Investigation of the Flowfield Downstream of a Discontinuous Backward-Facing Step on a Swept Flat Plate

William Yoshida

A thesis

submitted in partial fulfillment of the requirements for the degree of

Master of Science

University of Washington

2020

Committee:

Michael B. Bragg

M. Reza Soltani

Program Authorized to Offer Degree:

Aeronautics and Astronautics

University of Washington

Abstract

INVESTIGATION OF THE FLOWFIELD DOWNSTREAM OF A DISCONTINUOUS BACKWARD-FACING STEP ON A SWEPT FLAT PLATE

William Yoshida

Chair of the Supervisory Committee:
Michael B. Bragg

An experimental study of a swept flat plate has been performed in the University of Washington 3' by 3' Low-Speed Wind Tunnel to improve the understanding of iced swept-wing flowfields. The swept flat plate model included two interchangeable backward-facing steps that were mounted to the full span of the plate leading edge, as well as an adjustable trailing-edge flap. Each of the steps was designed to recreate one of two key flowfields characteristic of swept-wing artificial ice shapes while reducing the geometric complexity of the swept wing model. The first was a spanwise-running leading-edge vortex produced by certain low-fidelity artificial ice shapes. This type of flowfield is referred to as Type I, and was produced using the solid backward-facing step. Characteristic streamwise-running streaks of oil identify the second flowfield in surface flow visualization. This flow pattern was referred to as Type II, and was recreated with a modified backward-facing step that included spanwise-periodic gaps and solid features. Configurations of the flat plate were tested at four trailing-edge flap settings, and three Reynolds numbers based on step height of 2.50×10^4, 3.78×10^4, and 5.03×10^4, which correspond to Mach numbers of 0.088, 0.132, and 0.176. The experimental techniques used included fluorescent-oil surface flow visualization, surface pressure measurements, and five-hole pressure probe measurements.

From measurements made using a five-hole pressure probe, it was shown that the trailing-edge flap had significant effects on the local flow angularity about the leading-edge. These angularity changes varied across the span and had visible effects on the resulting oil flow visualization. Type II streamwise flow features were identified as having one of two sets of traits using two oil flow visualization techniques, For configurations with negative flap deflection, the flowfield behind the step was dominated by clear streamwise streaks, each appearing to emanate from a gap in the step. A detailed surface oil flow visualization technique presented evidence that this type of streamwise feature may be the result of pairs of counter-rotating streamwise vortices that form in the wake behind each solid feature in the step. This composition was distinct from the second type, which was seen at high flap angles in the oil flow as a superposition of a leading-edge separation vortex and streamwise streaks of vortical flow. These streaks were larger than the first case, and did not correspond to any single gap or solid feature. This behavior is similar to the flowfields associated with certain low-fidelity representations of scallop artificial ice shapes. The second type was hypothesized to be a result of a streamwise instability in the separated shear layer; however, additional work is required. A coating of 24 grit on the solid step produced small effects in the pressure distribution and tended to increase the mean shear layer reattachment length behind the step. Finally, the effect of Reynolds and Mach number was seen to be small, both in the pressure measurements and in the oil flow visualization. This result was in agreement with past research on iced-wing aerodynamics and swept backward-facing steps.

Acknowledgments

This work was funded by the University of Washington, but relied on research conducted as part of a collaborative research project with participation from NASA Glenn, FAA Technical Center, ONERA, University of Virginia, University of Washington, and the University of Illinois. The University of Washington and University of Illinois were funded by FAA grant 15-G-009 with support from Dr. Jim Riley and Tim Smith.

I can say with certainty that I would not have been able to complete this thesis without the kind and generous support of many people. I owe a great debt of gratitude to Professor Mike Bragg, first for giving me the opportunity to work with him and get my master's degree, then for his unflagging support and cool-headed advice, even in the face of unexpected circumstances.

Before a graduate degree was part of the plan, Dr. Brian Woodard gave me a chance and took me on as undergraduate hourly for the icing research program, which changed my life. Thank you for being a constant source of help and encouragement.

Without the generous help of Professor Owen Williams, the wind tunnel experiments discussed in the thesis would not have been possible. I am deeply grateful that he allowed me to use wind tunnel model components and other essential supplies, supplied CAD models that were instrumental in the preparations for the experiments, and helped to plan and install my own model.

Many thanks to Professor Reza Soltani, whose kindness, generosity, and willingness to go the extra mile to help were an inspiration.

Thank you to Kevin Ho and Eliot George for their help leading up to and throughout my experiments. Maddie Samuell was there for me, from first teaching me how to lay down aluminum tape to those many long night shifts during the summer. I am honored to have spent the last two years in Seattle with my beloved office-mates, Pablo Trefftz-Posada, Toni Deleo, and Abhi Aithal. Thank you for all the fun times, and also helping me with things I never could have managed alone.

Most of all, thank you to my family for the love and support that got me through the toughest times.

Contents

List of Figures vii

List of Tables xii

1 Introduction 1

2 Review of Literature 7
- 2.1 Iced Airfoil Aerodynamics . . . 7
  - 2.1.1 Performance Penalties . . . 8
  - 2.1.2 Flowfield Three-Dimensionality . . . 10
  - 2.1.3 Flowfield Unsteadiness . . . 12
- 2.2 Swept-Wing Icing . . . 14
  - 2.2.1 Ice Accretion Processes . . . 14
  - 2.2.2 Iced Swept-Wing Aerodynamics . . . 16
- 2.3 Icing Fidelity Studies and Fundamental Geometries . . . 24
  - 2.3.1 Iced Airfoil Fidelity . . . 25
  - 2.3.2 Iced Swept-Wing Fidelity . . . 32
  - 2.3.3 Swept Backward-Facing Steps . . . 40

3 Experimental Apparatus 45
- 3.1 Wind Tunnel Facility . . . 45
- 3.2 Swept Flat Plate Model . . . 45
- 3.3 Leading-Edge Step Shapes . . . 49
- 3.4 Data Acquisition . . . 53
- 3.5 Fluorescent-Oil Surface Flow Visualization . . . 55

4 Results and Discussion 58
- 4.1 Trailing-Edge Flap Deflection Effects . . . 58
  - 4.1.1 Flow Angularity Upstream of Leading Edge . . . 59
  - 4.1.2 Flow Separation . . . 61
- 4.2 Effect of Spanwise Discontinuities in Step . . . 72
  - 4.2.1 Standard Discontinuous Step . . . 73
  - 4.2.2 Discontinuous Step with Alternating Blocked Gaps . . . 82
  - 4.2.3 Solid Step with Discontinuous Center Section . . . 88
  - 4.2.4 Summary of Streamwise Streak Variation . . . 90
- 4.3 Effect of 24 Grit on Solid Step . . . 96
- 4.4 Reynolds Number and Mach Effects . . . 103

5 Summary, Conclusions, and Recommendations 108
- 5.1 Summary . . . 108
- 5.2 Conclusions . . . 109

5.3 Recommendations 111

6 References 114

List of Figures

2.1 Geometry of a shape, after Bragg et al. [1] 8
2.2 Sectional drag coefficient penalties for a NACA 0012 airfoil; a) With removal of upper or lower horn, b) across a range of icing conditions 9
2.3 Time-averaged pressure distribution for the clean NACA 0012 airfoil and the airfoil with 2-D and 3-D glaze ice simulations at $Re = 1.8 \times 10^6$ and $\alpha = 5^\circ$, after Gurbacki [2] 10
2.4 Performance variations for the clean NACA 0012 airfoil and the airfoil with 2-D and 3-D horn ice simulations at $Re = 1.8 \times 10^6$, adapted from Gurbacki [2] 11
2.5 Comparison of the surface flowfield behind a (a) horn-ice accretion casting and a (b) 2-D smooth horn-ice simulation at $Re = 1.8 \times 10^6$ and $M = 0.18$, after Busch et al. [3] 12
2.6 Sketch of possible hairpin vortex in flowfield causing observed spanwise cell structures on the surface of the NACA 0012 airfoil with the 3-D glaze ice casting, after Gurbacki [2] 12
2.7 Separation streamlines phase-averaged according to the instantaneous separation bubble cross-sectional area ($Re = 0.9 \times 10^6, M_\infty = 0.20$); (—) Nominal separation streamline, (- - -) Contracted/expanded separation streamlines. Adapted from Jacobs [4] 13
2.8 Summary of locations where unsteady modes were most dominant in the horn ice flowfield, after Ansell [5] 13
2.9 Ice accretion on a swept wing at glaze ice conditions, complete scallop case, critical distance = 0, after Vargas and Reshotko [6]. (a) Roughness elements (all over the ice accretion) develop into glaze ice feathers with a preferred direction of growth perpendicular to the external streamlines. (b) The feathers join along the preferred direction of growth to form ridges that will develop into incipient scallop tips. (c) Incipient scallop tips join at their tops to form complete scallop. 16
2.10 Sectional view of the simulated glaze ice accretion, after Khodadoust and Bragg [7] 17
2.11 Numerical results for the flow over a swept NACA 0012 with a leading-edge ice accretion at $Re = 1.5 \times 10^6$ and 8° angle of attack, after Kwon and Sankar [8]; left: surface oil flow simulation; right: particle trajectory simulation. 18
2.12 (a) NASA Langley 1/8 scale twin engine subsonic transport model, after Reehorst et al. [9]. (b) Ice shape #1 on the model horizontal tail with ice shape highlighted . 19
2.13 Effects of Ice #2 on longitudinal aerodynamic characteristics of the model in the $\delta_f = 40^\circ$ configuration, after Reehorst et al. [9] 20
2.14 3.5% Scale GTM installed in the NASA Langley 12-ft Low-Speed Wind Tunnel C-sector mounting and positioning system, after Broeren et al. [10] 21
2.15 Cross-section view of wing ice shape at three spanwise locations on the 3.5% scale GMT, after Broeren et al. [10]: (a - c); (d) Surface-oil flow visualization on the clean wing for $\alpha = 8^\circ$. Flow is from left to right. 22
2.16 Polyurethane castings of the six ice shapes obtained from icing tests at IRT, after Papadakis et al. [11] 23

2.17 Effect of IRT ice shapes on pressure distributions at 15% semispan, $Re = 1.8 \times 10^6$, after Papadakis et al. [11]; (a) $\alpha = 8°$; (b) $\alpha = 12°$; 23
2.18 Effect of IRT ice shapes ON C_L, C_D, and C_M at $Re = 1.8 \times 10^6$, after Papadakis et al. [11] 24
2.19 (left) Simulated horn ice shape locations and angles, (right) Position effects on C_l for ice shape with horn radius to width ratio $r/w = 0.5$ and height $h = 0.8$" at $Re = 1.8 \times 10^6$. Adapted from Kim and Bragg [12] 26
2.20 Contour of turbulence intensity, $\alpha = 3°$, $Re = 1.0 \times 10^6$, after Manshadi and Esfeh [13] (Reattachment location is marked with a dashed line). 28
2.21 Velocity vectors and streamlines from RANS computations; NACA 0011, $\alpha = 5°$, $h = 1.5$", $s/c = 0.02$, $\theta = -80°$, $Re = 1.86 \times 10^6$, after Papdakis et al. [14] 28
2.22 Photograph and tracing of a spanwise ridge ice accretion on a NACA 23012 airfoil. Adapted from Broeren et al. [15] 29
2.23 Typical representation of flowfield around a simulated spanwise-ridge ice shape, after Calay et al. [16] 30
2.24 Wake velocity profiles for different ice shapes, after Calay et al. [16]; (left) $x/c = 0.05$; (right) $x/c = 0.25$ 31
2.25 NACA 23012 model with quarter round ice simulation. (0.25" quarter round at x/c = 0.10 shown), after Lee and Bragg [17] 31
2.26 Summary of boundary-layer state on the NACA 23012 airfoil with 0.25-in. quarter-roung simulated ice shape at $x/c = 0.10$ obtained from flow visualization. Natural transition. $Re = 1.8 \times 10^6$, after Lee and Bragg [17] 32
2.27 Photographs of the upper surface of subscale CRM65 semispan wing models installed in their respective wind tunnels; left: 13.3% scale CRM65 semispan wing installed in ONERA F1 test section; right: 8.9% scale CRM65 semispan wing installed in WSU test section. 35
2.28 Photographs of the Maximum Scallop ice shape at the three spanwise locations, after Woodard et al. [18] 36
2.29 Renderings of artificial ice shapes. From top to bottom, the ice shapes are: Maximum Scallop High Fidelity, Maximum Scallop 3-D Smooth, Small Gap 3-D Discontinuous, Medium Gap 3-D Discontinuous. 37
2.30 Surface oil flow visualization for the High Fidelity and 3-D Smooth ice shapes at $\alpha = 6.4°$ illustrating the characteristics of Type I and Type II flowfields. Reattachment indicated by a solid red line. Suction side shown with flow from left to right, after Woodard et al. [19] 38
2.31 Pressure distributions for the High Fidelity and 3-D Smooth ice shapes at $\alpha = 6.4°$ illustrating the characteristics of Type I and Type II flowfields, after Woodard et al. [19] 38
2.32 Surface oil flow visualization for the High Fidelity, Small Gap, and Medium Gap 3-D Discontinuous ice shapes at $\alpha = 4.3°$. Suction side shown with flow from left to right, after Woodard et al. [19] 40
2.33 Close-up view of wing from y/b = 0.30 to 0.44 for the High Fidelity, Small Gap, and Medium Gap 3-D Discontinuous ice shapes at $\alpha = 4.3°$ with markers illustrating the period of the type II flowfield streamwise features. Suction side shown with flow from left to right, after Woodard et al. [19] 40

2.34 Diagram of the separated flow behind a backward-facing step, after Selby [20] . . . 41
2.35 Pictorial summary of surface flow features determined from oil flow downstream of a swept, backward-facing step, after Selby [20] 42
2.36 Backward-facing step geometries, after Selby [21] 43

3.1 Photograph of wind tunnel facility 46
3.2 Diagram of flat plate assembly 47
3.3 Close-up diagram of pressure tap array and nomenclature 47
3.4 CAD render of plate assembly showing flap angle sign convention used 48
3.5 Exploded view of model installation 49
3.6 Spanwise variation of the size of the discontinuity features after Woodard et al. [22]. The feature size is scaled to the WSU model and is measured along the leading edge of the wing. Measurements from the High Fidelity ice shape are also shown for reference. 51
3.7 Dimensioned drawing of discontinuous step features and gaps, looking downstream parallel to the test section walls 51
3.8 CAD rendered section cuts of the flat plate with leading-edge attachment, (left) discontinuous step, (right) solid step 52
3.9 CAD renders of the 3-D printed leading-edge step sections; (Top) solid, (bottom) discontinuous 52
3.10 Photograph of the alternating-gap discontinuous step and the pressure tap array . . 53
3.11 Photograph of five-hole probe mounted on the underside of the plate 55

4.1 Diagram of the flap plate assembly showing the flap angle sign convention 59
4.2 Local flow inclination angle 4h upstream of leading edge and level with plate underside; solid step at 60 m/s 60
4.3 Local flow inclination angle 4h upstream of leading edge and level with plate underside; discontinuous step at 60 m/s 60
4.4 Sample oil flow visualization image showing vortex reattachment length behind the solid step at 60 m/s 62
4.5 Variation in mean streamwise reattachment length at 60 m/s with flap angle, as measured from oil flow visualization images 63
4.6 Pressure distribution along the streamwise tap row for the solid step at each flap angle and 60 m/s 64
4.7 Diagram of steady flow past a two-dimensional wedge, after Tanner [23] 65
4.8 Comparison of swept flat plate and CRM65 oil flow visualization with vortex reattachment indicated by dashed line; (left) solid step, flap angle of -10°, $Re_h = 5.03 \times 10^4$, (right) Maximum Scallop 3-D Smooth, $\alpha = 4^\circ$, $Re = 1.6 \times 10^6$ 66
4.9 Comparison of swept flat plate and CRM65 oil flow visualization with vortex reattachment indicated by dashed line; (left) solid step, flap angle of -5°, $Re_h = 5.03 \times 10^4$, (right) Maximum Scallop 3-D Smooth, $\alpha = 5^\circ$, $Re = 1.6 \times 10^6$ 67
4.10 Comparison of swept flat plate and CRM65 oil flow visualization with vortex reattachment indicated by dashed line; (left) solid step, flap angle of $+4^\circ$, $Re_h = 5.03 \times 10^4$, (right) Maximum Scallop 3-D Smooth, $\alpha = 6^\circ$, $Re = 1.6 \times 10^6$ 67

4.11 Pressure distribution along the streamwise tap row for the discontinuous step at each flap angle and 60 m/s 68
4.12 Comparison of swept flat plate and CRM65 oil flow visualization; (left) discontinuous step, flap angle of $-10°$, $Re_h = 5.03 \times 10^4$, (right) Medium Gap 3-D Discontinuous, $\alpha = 4°$, $Re = 1.6 \times 10^6$ 70
4.13 Comparison of swept flat plate and CRM65 oil flow visualization; (left) discontinuous step, flap angle of $-5°$, $Re_h = 5.03 \times 10^4$, (right) Medium Gap 3-D Discontinuous, $\alpha = 6°$, $Re = 1.6 \times 10^6$ 71
4.14 Comparison of swept flat plate and CRM65 oil flow visualization; (left) discontinuous step, flap angle of $+4°$, $Re_h = 5.03 \times 10^4$, (right) Medium Gap 3-D Discontinuous, $\alpha = 8°$, $Re = 1.6 \times 10^6$ 71
4.15 Close-up view of swept flat plate oil flow visualization of discontinuous step, flap angle of $+4°$ 72
4.16 Comparison of the oil film and stippled droplet oil flow visualization techniques at the same region downstream of the discontinuous step at $-10°$ flap angle and 60 m/s; (left) oil film, (right) stippled oil droplets 74
4.17 Close-up view of the stippled droplet oil flow visualization image downstream of the discontinuous step at $-10°$ flap angle and 60 m/s 75
4.18 Pressure distribution downstream of the discontinuous step at $-10°$ flap angle and 60 m/s. Red arrows indicate the location of solid features of the step. 78
4.19 Fluorescent-oil surface flow visualization behind the discontinuous step at 60 m/s with yellow lines indicating a streamwise feature; (upper left) $-10°$ flap deflection, (upper right) $-5°$ flap deflection, (lower left) 0° flap deflection, (lower right) $+4°$ flap deflection 79
4.20 Fluorescent-oil surface flow visualization behind the discontinuous step at 60 m/s and $+4°$ flap deflection 80
4.21 Comparison of streamwise pressure distributions behind the discontinuous and solid steps at 60 m/s and $+4°$ flap deflection 81
4.22 Fluorescent-oil surface flow visualization behind the discontinuous step with alternating gaps blocked at 60 m/s with yellow lines indicating a streamwise feature; (upper left) $-10°$ flap deflection, (upper right) $-5°$ flap deflection, (lower left) 0° flap deflection, (lower right) $+4°$ flap deflection 84
4.23 Close-up view of the fluorescent-oil surface flow visualization behind the discontinuous step with alternating gaps blocked at $-10°$ flap deflection and 60 m/s . . . 85
4.24 Pressure distribution downstream of the discontinuous step with alternating gaps blocked at $-10°$ flap angle and 60 m/s 87
4.25 Pressure distribution downstream of the discontinuous step with alternating gaps blocked at $+4°$ flap angle and 60 m/s 87
4.26 Diagram illustrating a proposed flowfield about the discontinuous step to explain the observed surface flow visualization patterns 88
4.27 Fluorescent-oil surface flow visualization behind the solid step with the discontinuous center section installed at 60 m/s with yellow lines indicating a streamwise feature; (upper left) $-10°$ flap deflection, (upper right) $-5°$ flap deflection, (lower left) 0° flap deflection, (lower right) $+4°$ flap deflection 89

4.28 Close-up view of the fluorescent-oil surface flow visualization for the solid step with the discontinuous center section installed at a flap angle of -5° and 60 m/s . . 91
4.29 Close-up view of CRM65 model from y/b = 0.30 to 0.44 for the Small Gap 3D Discontinuous ice shape at $\alpha = 2.2, 4.3, 5.3$ and 6.4 deg. with markers illustrating the period of the type II flowfield streamwise features, after Woodard et al. [19] . . 92
4.30 Comparison of the streamwise pressure distributions for each of the variations on the discontinuous step at a flap angle of -10° and 60 m/s 94
4.31 Comparison of the pressure distributions for each of the variations on the discontinuous step at a flap angle of -10° and 60 m/s 94
4.32 Comparison of the pressure distributions for each of the variations on the discontinuous step at a flap angle of $+4^\circ$ 95
4.33 Comparison of the streamwise pressure distributions for each of the variations on the discontinuous step at a flap angle of $+4^\circ$ and 60 m/s 95
4.34 Fluorescent-oil surface flow visualization on the 8.9% scale CRM65 model with Maximum Scallop 3-D Smooth ice shape, $\alpha = 4^\circ$, $Re = 1.6 \times 10^6$; (left) no grit applied, (right) 60 grit applied 98
4.35 Close-up view of the fluorescent-oil surface flow visualization for the solid step without grit at a flap angle of -10° and 60 m/s 100
4.36 Close-up view of the fluorescent-oil surface flow visualization for the solid step with 24 grit at a flap angle of -10° and 60 m/s 100
4.37 Pressure distribution along the streamwise tap row for the solid step with and without 24 grit; flap angle of -10°, 60 m/s 101
4.38 Pressure distribution along the streamwise tap row for the solid step with and without 24 grit; flap angle of -5°, 60 m/s 101
4.39 Pressure distribution along the streamwise tap row for the solid step with and without 24 grit; flap angle of 0°, 60 m/s 102
4.40 Pressure distribution along the streamwise tap row for the solid step with and without 24 grit; flap angle of $+4^\circ$, 60 m/s 102
4.41 Variation in mean streamwise reattachment length with Reynolds number, as measured from oil flow visualization images 104
4.42 Oil flow visualization images of discontinuous step with -10° flap deflection at each airspeed tested; (top) 30 m/s, 3 minute run time (center) 45 m/s, 4 minute run time (bottom) 60 m/s, 5 minute run time 106
4.43 Variation in the pressure distribution along the streamwise tap row; solid step with flap angle of -10° 107
4.44 Variation in the pressure distribution along the streamwise tap row; discontinuous step with flap angle of -10° 107

List of Tables

4.1 Number of nodes for different mesh resolutions 103

Nomenclature

α	Angle of attack
α_{local}	Inclination angle of local flow
Λ	Wing sweep angle
λ	Wing taper ratio
μ	Dynamic viscosity
AR	Aspect ratio
b	Span
c	Chord length
C_D	Drag coefficient
C_L	Lift coefficient
C_M	Pitching moment coefficient
C_p	Pressure coefficient
CFD	Computational fluid dynamics
CRM	Common Research Model
$CRM65$	65% scale Common Research Model
DNS	Direct numerical simulation
FAA	Federal Aviation Administration
h	Step height
IRT	Icing Research Tunnel
LDV	Laser-doppler velocimetry
LWC	Liquid water content
M	Mach number
MAC	Mean aerodynamic chord
MVD	Mean volumetric diameter
$NACA$	National Advisory Committee for Aeronautics

$NASA$	National Aeronautics and Space Administration
$ONERA$	Office National d’Etudes et de Recherches Aérospatiales
PIV	Particle image velocimetry
q	Dynamic pressure
$RANS$	Reynolds-Averaged Navier-Stokes
Re	Reynolds number based on mean aerodynamic chord
Re_h	Reynolds number based on step height
SLD	Supercooled large droplet
$SWIP$	Swept-Wing Icing Project
U_∞	Freestream velocity
$UIUC$	University of Illinois at Urbana-Champaign
UW	University of Washington
WSU	Wichita State University

Chapter 1

Introduction

In a specific range of atmospheric conditions, ice can build up on critical components of an aircraft, such as the wings, horizontal and vertical tail elements, propellers, and more. Aircraft icing has severe implications on performance and stability, and as a result, it continues to cause incidents and accidents. Many trusted methods of ice protection exist, such as pneumatic boots, electro-thermal heating elements, and engine bleed air heating. Even with the use of such equipment, the understanding of iced-wing aerodynamics remains an important area of study for the safe operation of aircraft. There is an present need for improved icing analysis, which would facilitate aircraft design and certification, while reducing costs.

Much of the understanding of aircraft icing is based upon a large body of work regarding airfoil icing built from the last few decades. Correspondingly, the understanding of the flow phenomena is reasonably mature, and several comprehensive reviews have been completed regarding this topic. One such review is found in a comprehensive AGARD report [24]. The report covers several topics relevant to certification and qualification of aircraft, including types of ice accretion and their impacts on performance and handling. Across the range icing conditions, such as the temperature, speed, angle, and liquid water content, icing is generally seen to result in increased drag, higher stall speeds, and lower stall angles, as well as abnormal stability characteristics. This report is most valuable as a wide-ranging overview of topics such as meteorological conditions, experimental techniques, and ice prediction codes. However, it falls somewhat short in its discussion of the iced flowfield. Another extensive review paper by Lynch and Khodadoust [25] contributes a wealth of compiled data with emphasis on performance degradation, as quantified by lift, drag, stall angle, and other measures.

These two reviews categorize ice accretions primarily by icing conditions or appearance, such as ground frost, rime, and glaze, and devote their attention to the integrated aerodynamic effects. In their subsequent review paper, Bragg et al. [1] shifted the discussion by focusing on the flow physics of iced airfoils as a way to help explain the well-studied performance effects. Building upon many previous works, Bragg et al. [1] reduced ambiguity in airfoil icing by suggesting a classification system for ice accretions. The proposed classifications were grounded in similarities of critical aspects of the flowfield, in addition to the geometry. For instance, the classification of ice roughness is identified as the initial stage of ice accretion, which modifies the airfoil contour with small elements. Ice roughness has well-known adverse effects on maximum lift and drag; however, Bragg et al. [1] explains these effects with compiled results indicating the effects of roughness on the boundary layer and wing flowfield. This classification is made separate from that of horn ice, which may possess ice roughness on its surface, but is characterized by a large, unsteady separation bubble beginning at the leading-edge accretion. This bubble, in turn, modifies the airfoil pressure distribution and the reattachment point quickly moves downstream with angle of attack, contributing to the observed performance degradation that had been noted by many previous studies. In some ways this is comparable to the flow behind a 2-D backward-facing step, in which flow along a flat plate encounters a sharp expansion. At that point, the flow separates and forms a shear layer and recirculation region before reattaching. Using previous results and the straightforward nature of the backward-facing step are useful to analyze many separated flows in aircraft icing. Overall, the quality and thorough interpretation of iced airfoil research indicates a good understanding of the underlying physics, as well as the effects on aircraft. Fundamental separated flows will be explored further in Chapter 2, along with a continued review of airfoil icing aerodynamics.

Though the challenge of straight-wing icing remains, many modern aircraft employ three-dimensional wings with sweep, twist, and taper, ranging from small regional jets to large transport aircraft. These additions are made for structural or stability reasons, to delay compressibility effects, or efficiency. The consequence is that even the clean-wing aerodynamics of three-dimensional wings, much less the iced, may have increased complexity compared to the 2-D case.

For instance, wing sweep increases loading towards the tip as the induced flow angle changes spanwise. The spanwise lift distribution results in an outboard favorable pressure gradient and a component of the boundary-layer velocity that flows from root to tip [26]. This outward spanwise component thickens the boundary layer near the tip, making swept wings more prone to tip-stall. Both Furlong and McHugh [26] and Poll [27] describe the modalities of flow separation on swept wings. Depending upon sweep angle, leading-edge radius, and Reynolds number, separation may vary from a large spiral vortex in the case of leading-edge separation to trailing-edge separation, or even a combination of the two. Considering the case of iced swept-wing aerodynamics, the factors introduced with the three-dimensionality of the wing may influence the ice accretion and the resulting flowfield.

Researchers have conducted experimental investigations into the aerodynamics of iced, swept wings. Khodadoust and Bragg [28] tested a wing with a NACA 0012 section, a sweep of 30 degrees, and fitted with a simulation of a leading-edge ice accretion at $Re = 1.5 \times 10^6$. They found the most dominant feature of the flowfield to be a large separation bubble, which grew from root to tip and at higher angles of attack, accompanied by a significant increase in drag. Using a simple wing and simulated ice accretion allowed for a clearer picture of gross effects of the leading-edge ice, but only captured a small portion of the range of possible icing-related phenomena. Papadakis et al. [11] embarked on a more substantial aerodynamic testing campaign of swept-wing ice on a typical business jet wing with 28 degrees of sweep, a taper ratio of 0.4, and 4 degrees of washout. Dry-air wing tunnel testing was completed for a selection of leading-edge ice accretions generated in NASA Glenn Icing Research Tunnel [29] and by the accretion code LEWICE 2.0. The test results were limited to surface pressure and force balance measurements, but recorded increases in minimum drag relative to the clean wing as large as 3533% and decreases in maximum lift by as much as 93.6%. The presence of a prominent leading-edge separation bubble was also indicated in several cases by the surface pressure distribution, but a more detailed study into the 3-D flowfield was not made. Ultimately, research on swept-wing icing aerodynamics has not reached the same depth as that for iced airfoils, as will be discussed in a more detailed review of research on swept-wing icing in Chapter 2.

In response to the comparative lack of data for iced swept wings, NASA, the Federal Aviation Administration (FAA), and the Office National d'Etudes et Recherches Aérospatiales (ONERA) have undertaken a collaborative research project. The overall goal of this project is to contribute to flight safety through a new body of experimental and computational research on swept-wing ice accretion formation and the resulting aerodynamic effect. Broeren et al. [30] describes the motivation and objectives of the project in greater detail. The project uses a 65% scale version of the Common Research Model (CRM) wing [31, 32], referred to as the CRM65. The model was designed to be representative of a modern, wide-body commercial aircraft and possesses a complex geometry with sweep, taper, twist, and a Yehudi break. A database of ice accretions for the CRM65 at multiple conditions was compiled through testing in the NASA Glenn Icing Research Tunnel (IRT) [33], using models described by Fujiwara et al. [34], with each ice accretion digitally recorded using laser-scanning techniques [35, 36]. Dry-air aerodynamic wind tunnel testing of ice accretion simulations was performed at low Reynolds number using an 8.9% scale model of the CRM65, and at high Reynolds number using a 13.3% scale model. These models were fitted with full-span reproductions of ice shapes using the scans recorded in the IRT, and a process described by Camello et al. [37]. Such manufactured, full-span ice accretion simulations are referred to as ”artificial ice shapes.” The results of that series of tests are discussed in several papers [38, 39, 40, 41, 42, 43], which will be reviewed in more detail in Chapter 2.

A central objective of the research project, which for easier reference will be referred to as the Swept-Wing Icing Project, or SWIP, was determining the geometric fidelity of simulated leading-edge ice accretion that could approximate the true aerodynamic effects. Fidelity, in this and companion papers, refers to the level of realistic three-dimensional details that are included in the leading-edge ice accretion simulation used in dry-air aerodynamic testing. The operating principle is that if a low-fidelity ice accretion simulation can be shown to represent high-fidelity aerodynamics, this would simplify experimental and numerical simulation. The question of sufficient fidelity poses a particular challenge for swept-wing ice accretions, which in certain conditions form extremely complex and three-dimensional shapes, often referred to as ”scallops” or ”lobster tails” due to their unique shapes. Despite the growing body of work from this program, there is not a complete understanding of the complex flow physics that affect the aerodynamic effect of all leading-edge ice accretions. This statement rings particularly true in the case of scallop ice, their simplifications, and other highly three-dimensional ice accretions.

Woodard et al. [22, 19] describe the development and test results of a set of low-fidelity scallop ice shapes. One such low-fidelity simulation is created by making section cuts in the 3-D ice shape scan, then smoothing and lofting these cuts to span the full leading-edge. This artificial ice shape is called the 3-D smooth. Another low-fidelity ice shape is derived from the 3-D smooth and seeks to artificially recreate three-dimensional scallop-shapes by subtracting material from the solid ice geometry. During the aerodynamic testing of these shapes along with the high-fidelity, two key flowfields were observed: one dominated by leading-edge separation vortices, and one dominated by spanwise-varying features, observed in oil flow visualization as periodic streamwise streaks. For ease of reference and to reflect the incomplete understanding, the former is referred to as a Type I flowfield, and the latter as Type II. Broeren et al. [44] and Bragg et al. [45] also discuss Type I and Type II flowfields.

The work described in this thesis is complementary to the work being done within the current large-scale research project. As described, the overarching goal of the project is to build a database of realistic ice accretions and their aerodynamic effects. However, due to the sheer number of configurations to be tested among other constraints, detailed investigations of areas of complex and three-dimensional flow are not always possible. The experimental methods used in the series of wind tunnel tests on the CRM65 include balance data, surface oil flow visualization, mini-tufts, and wake data. This results in a database of swept-wing icing effects that is more extensive than any other in the open literature, but may only give a sketch of the flow phenomena at play. In the case of scalloped ice shapes and their effects, as introduced with the discussion of Type I and Type II flowfields, much has been learned, but many questions remain.

The overarching objective of the present study is to help improve the understanding of iced swept-wing flow physics. Specifically, this work aims to investigate the flow structures that are responsible for the streamwise-streak dominated Type II flowfield, and the effect that spanwise discontinuities in the step have upon the resulting separation vortex. To approach these objectives, an experimental set-up has been designed and built to add to the understanding of the complex flowfields that are characteristic of specific swept-wing ice accretion simulations. The set-up consists of a flat plate with a modified backward-facing step at the leading edge. The design was intended to generate a leading-edge separation vortex similar to that observed in Type I flowfields by using a fundamental geometry that reduces the number of variables. The separation vortex is then modified with the addition of discontinuities in the step, which were based on low-fidelity simulations of a scallop ice shape that resulted in a Type II flowfield. This flat plate model was tested in the University of Washington three foot by three foot low-speed wind tunnel. The experimental methods of this study consisted of fluorescent-oil surface flow visualization, static surface pressure measurements, five-hole pressure probe measurements, and making specific variations to the discontinuous geometry to probe their effects. All experiments were conducted at low Reynolds number based on step height using a highly simplified geometry, and are not intended to provide the most accurate representation of the swept-wing aerodynamics.

The organization of this thesis is as follows. Chapter 2 will present background information and a review of literature that will present context for the topic at hand. The review begins with iced-airfoil aerodynamics and then moves to the fundamentals of scallop ice formation and iced swept-wing aerodynamics. Having covered these background topics, the review continues with reviews most pertinent to this study, which include icing fidelity studies, aerodynamic experiments which also sought to approximate flow features with fundamental geometries and the swept backward-facing step. Chapter 3 describes the experimental methods used in this research. Chapter 4 presents and discusses the results of the application of those techniques in this work. Lastly, Chapter 5 offers a summary, conclusions, and recommendations.

Chapter 2

Review of Literature

This chapter will provide context and background information on a range of topics relevant to the understanding and interpretation of the current work. The review begins with iced airfoil aerodynamics, which will emphasize the effects and phenomena associated with flows characterized by a separation bubble. Then aspects of swept-wing icing are discussed in greater detail, as it is a central topic of this research. This latter part includes the geometric complexity in the ice accretion process on swept wings, as well as the resulting aerodynamic effect. Fidelity studies in iced-wing aerodynamics are also reviewed, as the current model geometry is based upon one such fidelity experiment. In the same vein, experiments on the swept backward-facing step are also reviewed for comparison with the model tested during this research.

2.1 Iced Airfoil Aerodynamics

Much of the understanding of wing icing effects originates from the study of straight wings with ice accretions. As a preface to iced swept-wing aerodynamics, which is the motivation for the experiments described in this paper, a selective review of airfoil icing will be given here. The following section focuses upon leading-edge ice accretions in which the flowfield is dominated by separated and reattaching flows. It is this subset of iced flowfields that is the most relevant to the research contained in this thesis. Bragg et al. [1] proposed four primary classifications of ice shapes on airfoils. They are as follows:

- Roughness
- Streamwise ice

- Spanwise-ridge ice
- Horn ice

Each classification is identified by key flowfield features and associated with specific aerodynamic effects. Of the four, horn ice is the most relevant to the research presented in this thesis, and it will be the focus of the remainder of this review section. Three important aspects of horn ice will be described: performance reductions, three-dimensionality, and unsteadiness.

Horn ice is typically a result of exposure to glaze ice conditions, which are described in Section 2.2.1, resulting in the distinctive profile for which the classification is named, Fig. 2.1. The accretion may also include some slight spanwise variation, surface roughness, and feather ice regions downstream of the horns. As diagrammed in Fig. 2.1, horn ice is characterized by the horn height, angle, and wrap distance from the leading edge. From a flowfield perspective, horn ice is dominated by the presence of separation bubbles that form behind each horn on the upper and lower surfaces. It is the separation bubble on the upper surface that has been seen to govern most of the aerodynamic effects. Relative to other classifications, the aerodynamic effect of horn ice is typically greater than streamwise ice and less than spanwise-ridge ice.

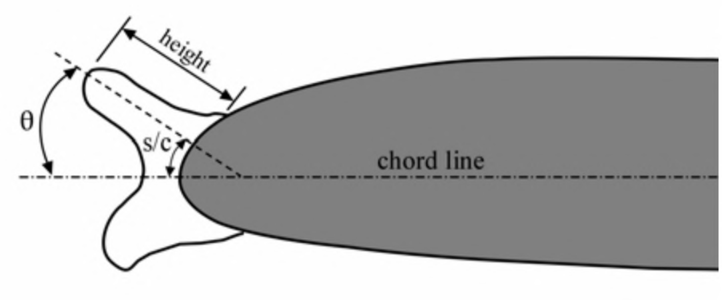

Figure 2.1: Geometry of a shape, after Bragg et al. [1]

2.1.1 Performance Penalties

The most thoroughly studied aspect of horn is the time-averaged effect on airfoil performance. Reviews such as those by AGARD [24], Lynch and Khodadoust [25], and Bragg et al. [1] are the synthesis of decades of study on airfoil icing, which at first focused heavily on integrated

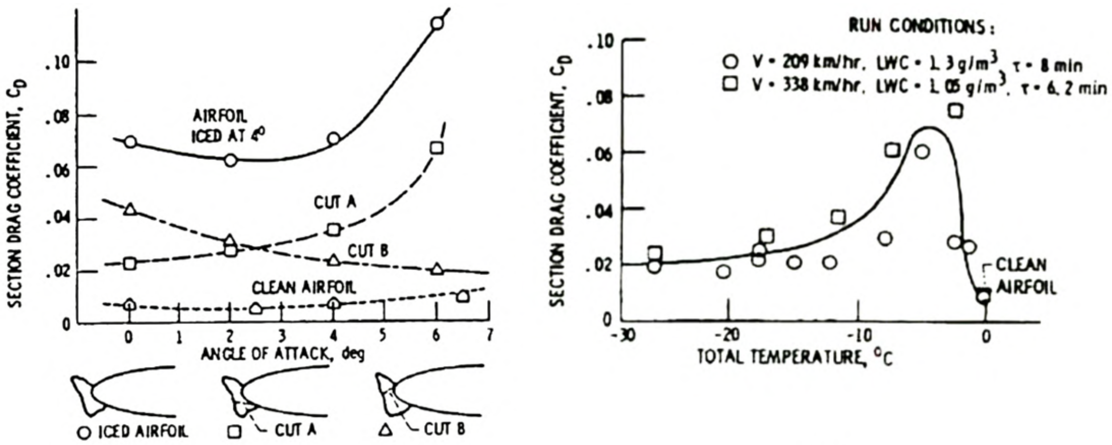

(a) **(b)**

Figure 2.2: Sectional drag coefficient penalties for a NACA 0012 airfoil; a) With removal of upper or lower horn, b) across a range of icing conditions

performance penalties on lift, drag, moment, and related measures. For instance, Olsen at al. [46] completed a study of drag increase on a NACA 0012 airfoil across a range of icing conditions, from which a selection of results are shown in Fig. 2.2. The peak in drag increase as icing tunnel temperature was decreased is associated with the set of icing conditions most likely to produce horn ice shapes, Fig. 2.2b. For a horn ice shape accreted at -4° F, the removal of the upper horn (Cut B) resulted in a significant reduction in drag relative to the full ice geometry, especially at higher angles of attach, Fig. 2.2a. The only diagnostic tool in the study was a wake rake, which did not enable a detailed study of the flowfield features. However, as later studies made clear, these performance differences were mainly due to the growth or absence of the upper surface separation bubble.

The bubble forms as the flow passes around the large leading-edge accretion and encounters the sharp expansion and adverse pressure gradient past the horn tip. Unable to turn rapidly enough, the flow separates, forming a shear layer between the fast-moving freestream above and slow recirculation region below. Entrainment of momentum through the turbulent mixing layer enables the shear layer to impinge on the airfoil surface and reattach downstream. Bragg et al. [1] compares the horn-ice flowfield to long laminar separation bubbles, within which the pressure distribution is nearly constant before recovering as the flow begins to reattach. This behavior is observed in

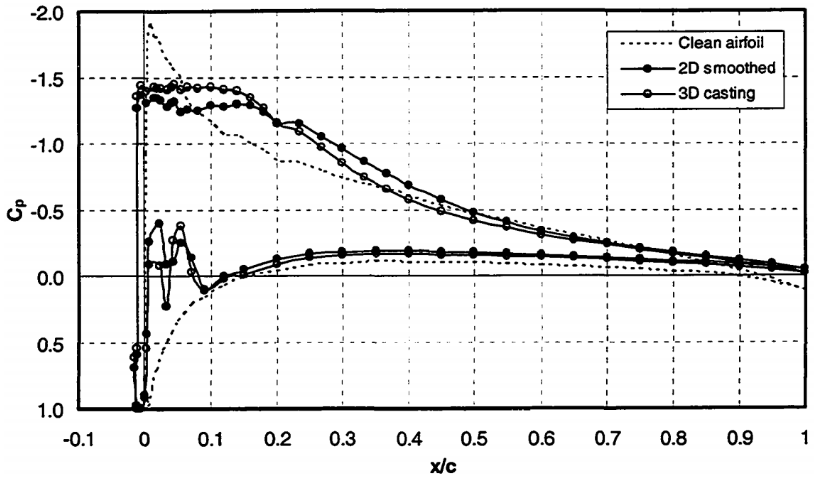

Figure 2.3: Time-averaged pressure distribution for the clean NACA 0012 airfoil and the airfoil with 2-D and 3-D glaze ice simulations at $Re = 1.8 \times 10^6$ and $\alpha = 5°$, after Gurbacki [2]

surface pressure measurements made by Gurbacki [2] on a NACA 0012 airfoil with two types of simulated horn ice accretion, Fig. 2.3. From these distributions, the separation beginning at the upper horn is seen to flatten the suction peak that is present on the clean airfoil and shift pressure recovery downstream. This modification to the pressure distribution causes significant changes in the pitching moment, Fig. 2.4b, even at lower angles of attack when lift penalties are not apparent, Fig. 2.3a. Also shown in Fig. 2.4a is the effect of the separation bubble on stall. As angle of attack increases, the separation bubble rapidly increases in length until it fails to reattach, resulting in a large decrease in stall angle. This flowfield and pressure distribution will remain important in the discussion of certain cases of iced swept-wing later in this thesis.

The discussion thus far has been primarily centered around time-averaged effects that are integrated and averaged across the entire span. As will be seen, the horn-ice flowfield possesses not only significant unsteadiness, but also degrees of three-dimensionality.

2.1.2 Flowfield Three-Dimensionality

One of the most intriguing aspects of the horn-ice flowfield is the effects of three-dimensional variations in the geometry and their resulting influence on the flowfield. This particular field of study has led to a body of research dedicated to the fidelity of leading-edge ice accretion simula-

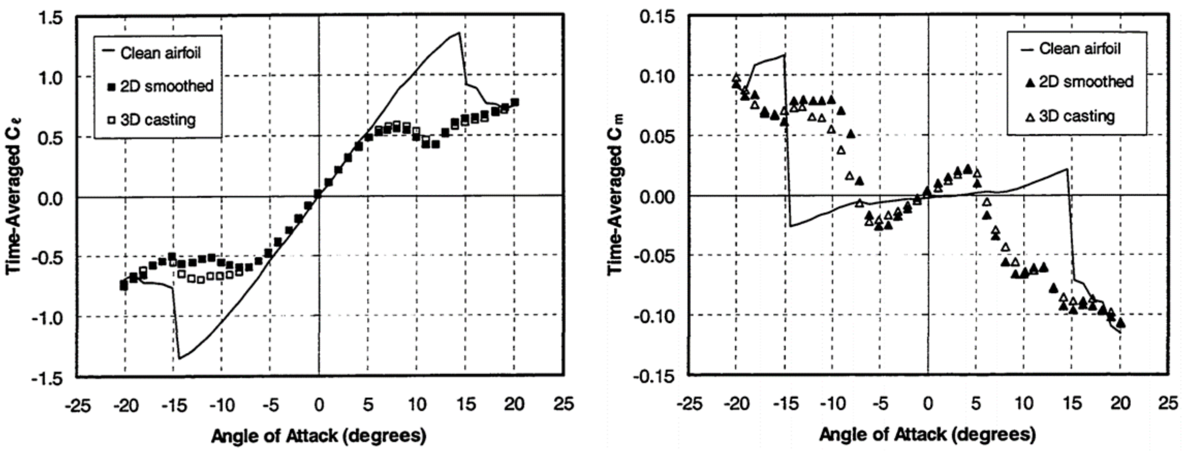

(a) **(b)**

Figure 2.4: Performance variations for the clean NACA 0012 airfoil and the airfoil with 2-D and 3-D horn ice simulations at $Re = 1.8 \times 10^6$, adapted from Gurbacki [2]

tion, some of which is discussed in greater detail in Section 2.3. This portion of the review will make use of the results of just a few in order to illustrate one aspect of the horn-ice flowfield.

Fig. 2.5 shows fluorescent-oil surface flow visualization completed by Busch et al. [3] for a high-fidelity horn ice shape based on a casting (left) and a low-fidelity shape made by extruding a smoothed section cut of the high fidelity (right). Flow is from left to right. In the surface-oil flow method of flow visualization, areas of higher shear experience more oil flow and streaking. In the case of the horn ice simulation, separation bubble reattachment is indicated by speckling of the oil at around 30% chord. Within the bubble, oil flowed left toward the ice shape, indicating reverse flow. In the flow behind the 3-D casting shape, the mean reattachment location is slightly upstream relative to the 2-D smooth shape. An interesting feature of the flowfield is the spanwise variations within the extent of the recirculation region. Gurbacki [2], who first observed the phenomena, referred to the features as ”cell-structures” and theorized that they might be a result of hairpin vortices, Fig. 2.6. Perhaps most interesting of all, is that no specific feature in the 3-D casting could be correlated with the regular appearance of the streamwise vorticity and cell-structures. A version of this experiment was first conducted by Gurbacki [2], then recreated by Jacobs [4] and Busch [3, 47], but the same cell-structure and vorticity was observed for high-fidelity horn ice simulation.

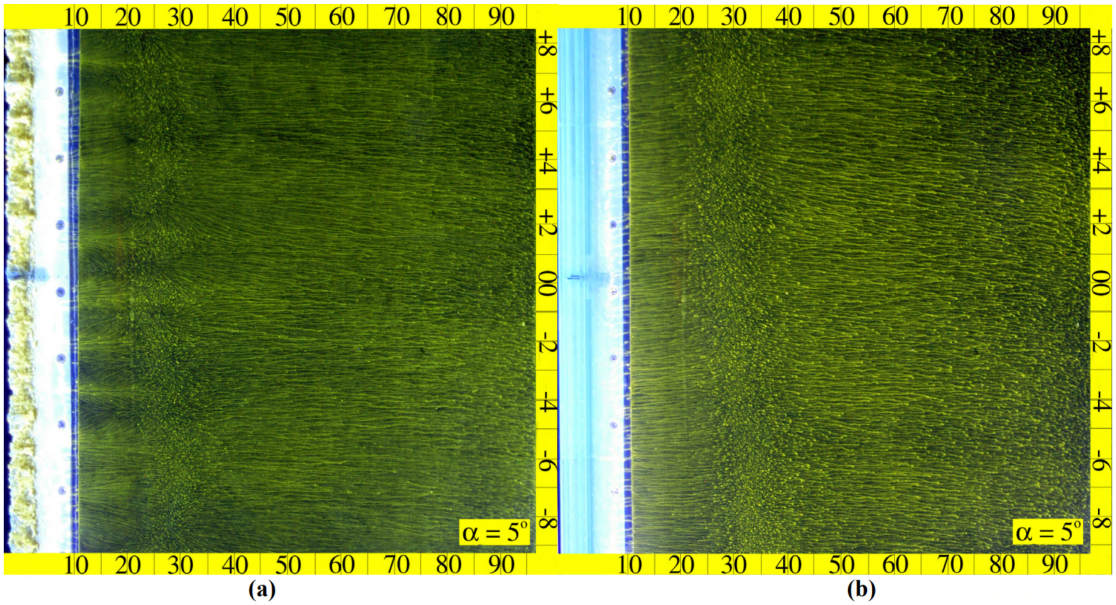

Figure 2.5: Comparison of the surface flowfield behind a (a) horn-ice accretion casting and a (b) 2-D smooth horn-ice simulation at $Re = 1.8 \times 10^6$ and $M = 0.18$, after Busch et al. [3]

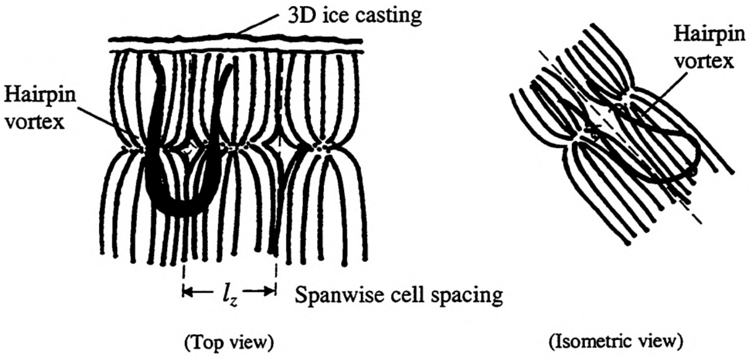

Figure 2.6: Sketch of possible hairpin vortex in flowfield causing observed spanwise cell structures on the surface of the NACA 0012 airfoil with the 3-D glaze ice casting, after Gurbacki [2]

2.1.3 Flowfield Unsteadiness

As an additional complicating factor, the separation bubble that is characteristic of horn ice is also highly unsteady. Gurbacki [2] identified two unsteady frequency modes using time-dependent hot wire anemometry measurements. The first unsteady mode, referred to as the regular mode, is a result of vortex pairing in the shear layer and vortex shedding. The second unsteady mode is the shear layer flapping mode, which related to the size of the separation bubble. Fig. 2.7

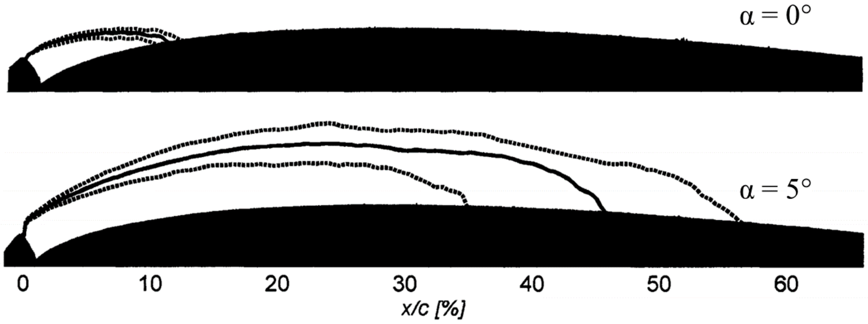

Figure 2.7: Separation streamlines phase-averaged according to the instantaneous separation bubble cross-sectional area ($Re = 0.9 \times 10^6, M_\infty = 0.20$); (—) Nominal separation streamline, (- - -) Contracted/expanded separation streamlines. Adapted from Jacobs [4]

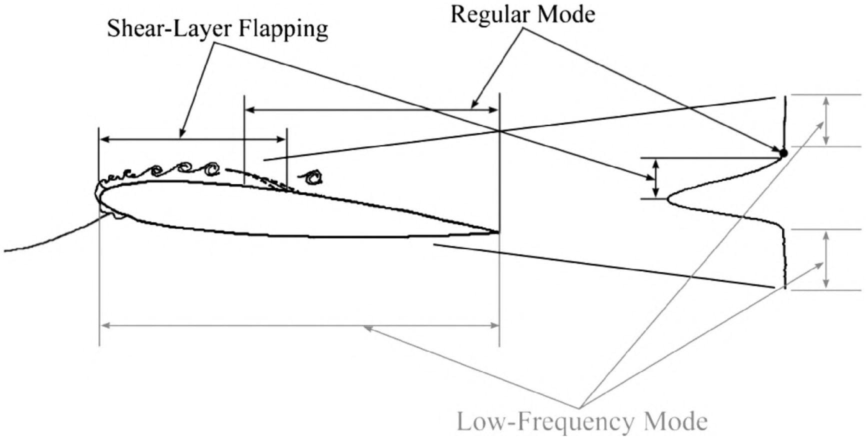

Figure 2.8: Summary of locations where unsteady modes were most dominant in the horn ice flowfield, after Ansell [5]

shows separation streamlines computed from particle image velocimetry (PIV) measurements by Jacobs [4] of the separation bubble behind a horn ice shape on a NACA 0012 with increasing angle attack. This figure shows the reattachment length advancing downstream and the range over which the shear layer fluctuates, which broadens at higher angles. A third, low-frequency mode was identified by Ansell and Bragg [5], which affected the entire airfoil circulation. Each identified mode and the region at which it is dominant is shown in Fig. 2.8.

In summary, the class of leading-edge ice accretions known as horn ice is characterized by a large separation bubble. This bubble alters the pressure distribution and affects the airfoil performance. The flow is highly unsteady and has a degree of three-dimensionality, notably in the form of semi-periodic streamwise vorticity within the separated region. When extended to 3-D, swept wings, airfoil horn ice makes for an interesting comparison.

2.2 Swept-Wing Icing

Swept-wing icing exhibits several differences and similarities with airfoil icing. In certain icing conditions, the accretion of ice on swept wings is comparable to the 2-D case. In other conditions, exposure results in highly three-dimensional shapes quite unlike any airfoil accretion. As swept wings also have distinct aerodynamics, this type of unique leading-edge ice leads to complex interactions and flowfields that are difficult to interpret. This section of the review will begin by exploring the processes by which scallop shapes, which are unique to swept-wings, develop. The review continues with an overview of aerodynamic tests on simulated swept-wing ice, leading up to the fidelity studies that are the basis for this thesis.

2.2.1 Ice Accretion Processes

The following section will introduce the fundamentals of swept-wing icing with emphasis on the highly three-dimensional ice accretions that are the motivation for the research in this thesis. While reviewing the initial stages of this type of ice is not wholly necessary to study the flow physics, it provides context and a deeper appreciation for the level of complexity. Before discussing the accretion processes, a brief overview of icing condition regimes. Quoting from AGARD Report 344 [24]:

> Conditions in which the freezing fraction is unity (cold air, low LWC) are known as rime icing conditions. The rime ice accretion process is relatively simple because the impacting droplets freeze and remain where they strike the surface. When the freezing fraction is less than unity, glaze icing conditions are said to prevail.
>
> Glaze icing is much more complex than rime icing because of the unfrozen water which is present in the impingement zone. As already mentioned, this water runs

back and tends to freeze somewhat downstream of where it impinged on the surface. Vargas [48] states that ice in the rime-ice regime does not fundamentally vary with sweep angle. However, shapes in the glaze-ice regime do exhibit a dependence upon sweep angle. As sweep increases, it is intuitive to recognize that unfrozen droplets may move along the surface of a swept-wing in ways that are entirely different from a 2-D wing.

Vargas [49] also reviews the findings of studies on swept-wing icing physics in glaze-ice conditions by the venerable Icing Branch at NASA Glenn Research Center. This review covers the current understanding of the formation of scallop ice on swept wings, which may be broken down into key findings, some of which are included below:

- Scallops are made of glaze ice feathers that grow from roughness elements located beyond a given distance from the attachment line. This distance is called the critical distance.
- The feathers that form the scallops show a preferred direction of growth perpendicular to the streamlines. Because of the preferred direction of growth, their thickness in the flow direction is much less than their width in the direction perpendicular to the flow.
- Ice accretions on swept wings at glaze and mixed ice conditions can be classified as complete scallops, incomplete scallops, and no-scallops depending on the critical distance.
- The critical distance has been shown to vary based on a number of factors, such as velocity and sweep angle [50], as well as the median volume diameter (MVD) [51], atmospheric temperature, and liquid water content [6].
- When the critical distance is zero, all of the ice shape is covered with glaze ice feathers, Fig. 2.9. During complete scallop growth, feathers join along the preferred direction of growth to form ridges. The ridges grow to form scallop tips. The scallop tips grow in size by joining with other scallop tips.

This section of the review was intended to provide background into scallop ice formation and highlight the complexity that such an accretion might impart upon the iced-wing flowfield. In the following sections, efforts to improve the understanding of the aerodynamic impact of swept-wing ice are described.

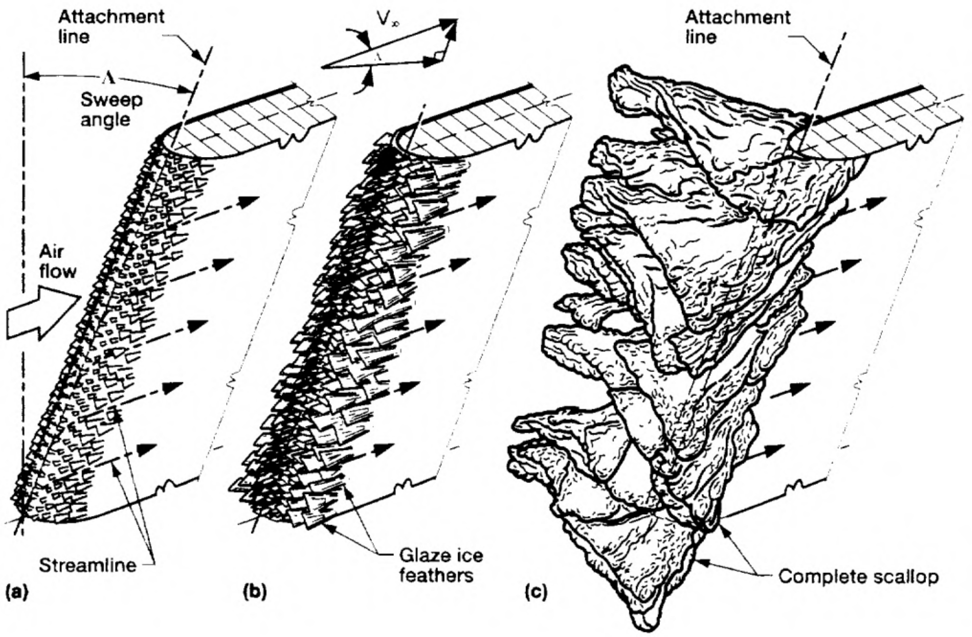

Figure 2.9: Ice accretion on a swept wing at glaze ice conditions, complete scallop case, critical distance = 0, after Vargas and Reshotko [6]. (a) Roughness elements (all over the ice accretion) develop into glaze ice feathers with a preferred direction of growth perpendicular to the external streamlines. (b) The feathers join along the preferred direction of growth to form ridges that will develop into incipient scallop tips. (c) Incipient scallop tips join at their tops to form complete scallop.

2.2.2 Iced Swept-Wing Aerodynamics

Thus far, this review has introduced the subset of airfoil ice accretions known as horn ice, whose aerodynamics are governed by a long, unsteady separation bubble. The physical properties by which highly three-dimensional scallop ice shapes form on swept wings has also been reviewed. This section will cover previous studies on the effects of swept-wing ice, moving from earlier experiments that made use of simple leading-edge horn ice simulations, to the latest results from the large, collaborative research program described in the introduction. In all, comprehensive investigations for five separate swept-wing models will be reviewed. As will be seen, separated and reattaching flows will remain an important factor, along with the additional effects brought about by scallop ice and its simulations.

The first set of iced swept-wing experiments to be discussed used a semispan NACA 0012

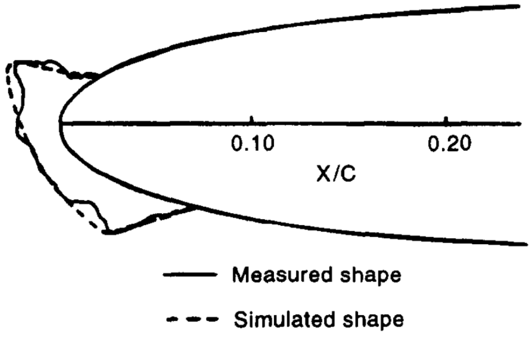

Figure 2.10: Sectional view of the simulated glaze ice accretion, after Khodadoust and Bragg [7]

model with $\Lambda_{LE} = 30°$, $AR = 2.3$, and no twist or taper, conducted by Bragg et al. [52] and Khodadoust and Bragg [7], with a companion numerical study by Kwon and Sankar [8]. The simulated ice shape applied to the leading-edge was produced by uniformly extending a horn ice shape accreted on a NACA 0012 airfoil at the NASA Glenn Icing Research Tunnel, Fig. 2.10. The experimental methods applied were surface and wake pressure measurements, surface oil flow, and helium bubble traces [7], as well as laser doppler velocimetry [52]. The surface oil and helium bubble flow visualization techniques showed the presence of a spiral vortex forming within a separation bubble aft of the horn ice shape. This flowfield was also seen in flattening of the the pressure distributions, which were reminiscent of the 2-D horn ice flowfield. The vortex-dominated flowfield was also observed in the numerical study, Fig. 2.11. Sectional lift was integrated from surface pressure taps rows, and sectional drag was computed from total pressure deficit in the wake. These computations showed a clear drag penalty, not unlike the effect of horn ice on a 2-D airfoil. A reduction in the loading of the outboard sections was also seen, indicating that the presence of the simulated ice shape exacerbated the tip stall behavior that swept wings often exhibit.

Reehorst et al. [9] tested a 1/8 scale twin-engine short-haul jet transport model in several configurations, pictured in Fig. 2.12a. This jet model included multi-element swept wings, and various flap and slat deflections were tested, as well as with and without landing gear. This campaign made use of two ice shapes first developed by Boeing for use in tests of a similar model that were simple extrusions of a constant cross-section for the entire span, similar to Khodadoust and Bragg [7]. One of these ice shapes is shown installed in Fig. 2.12b. Grit roughness was added to

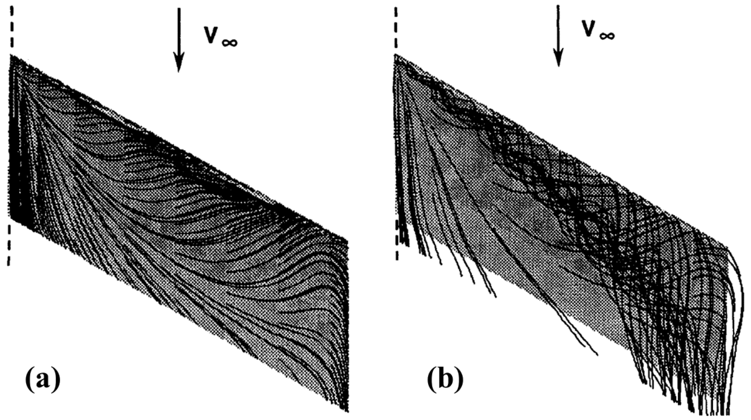

Figure 2.11: Numerical results for the flow over a swept NACA 0012 with a leading-edge ice accretion at $Re = 1.5 \times 10^6$ and 8° angle of attack, after Kwon and Sankar [8]; left: surface oil flow simulation; right: particle trajectory simulation.

both shapes, with grit sizes scaled by the full-scale momentum thickness. Experimental methods applied included force balance measurements and flow visualization with fluorescent mini-tufts and surface oil flow. Testing was conducted at a Reynolds number range of $Re = 8.2 \times 10^5$ to 1.8×10^6. The effect of each ice of the two ice shapes was seen to be roughly comparable, as they were both horn ice shapes with similar shapes. Some of the performance results are shown in Fig. 2.13. When comparing the clean to the overall iced performance, it may be seen that the simulated ice resulted in reduced stall angle and highly modified pitching moment. Before stall, drag penalties were not significant. Flow visualization revealed a complex and three-dimensional flowfield, despite the simplicity of the simulated ice geometry.

In a similar study, Broeren et al. [10] investigated the aerodynamic effects of simulated glaze ice on a 3.5% scale model of the NASA Langley Generic Transport Model (GMT), Fig. 2.14. The parameters of the main wing of the model were $\Lambda_{c/4} = 25°$, $AR = 8.0$, and $\lambda = 0.24$. Aerodynamic testing was conducted mostly at a Reynolds number based upon mean aerodynamic chord of approximately 0.24×10^6. Rather than using a simply extruded horn ice section as in previous studies, shapes were developed using the accretion code LEWICE 3D through a series of computational analyses. The resulting accretion was finally computed as a series of 2-D sections, some of which are shown in Fig. 2.15a-c, which were lofted to make a solid ice shape that varied across

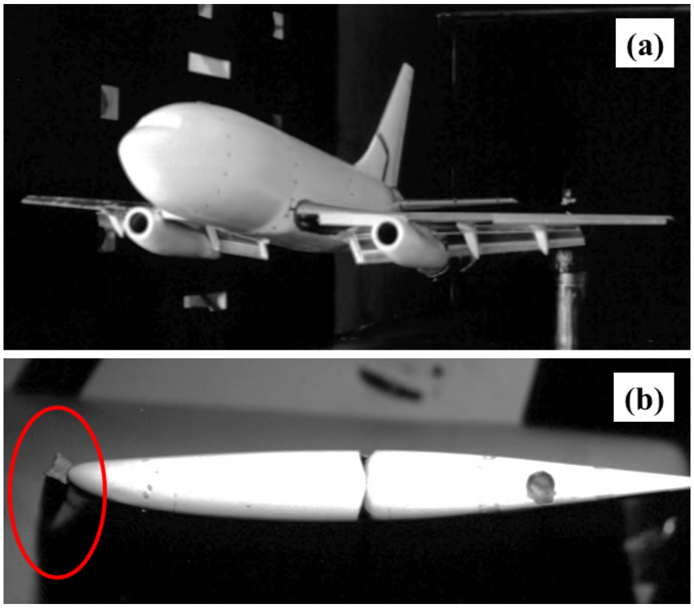

Figure 2.12: (a) NASA Langley 1/8 scale twin engine subsonic transport model, after Reehorst et al. [9]. (b) Ice shape #1 on the model horizontal tail with ice shape highlighted

the leading edges of the main wing and tail. Force balance measurements were made along with surface oil flow to gain a qualitative view of the iced flowfield. The results of this experiment showed a separation bubble that formed a spiral vortex behind the simulated ice shape and grew with angle of attack, Fig. 2.15d. Interestingly, while the addition of the ice shape increased drag, it had little effect upon lift and moment across the range of angles of attach. This study contributed valuable qualitative insights into the iced swept-wing flowfield, but did not use high fidelity glaze ice accretions, instead relying upon accretion codes.

The type of simulated swept-wing ice used in the three preceding sets of experiments was a reflection of the limited methodology of producing geometrically accurate ice simulations, which until recently consisted of section cut tracings and castings from molds. Depending on the wing in question, icing tunnel tests could not be conducted, or castings could not be scaled down from the icing tunnel to fit a model small enough to be usable for aerodynamic testing. Tracings pose an additional challenge for highly three-dimensional ice. The next set of experiments made use of realistic large-scale swept-wing ice accretions, most of which were highly three-dimensional.

For the fourth set of swept-wing ice experiments to be reviewed, Vargas et al. [29] generated

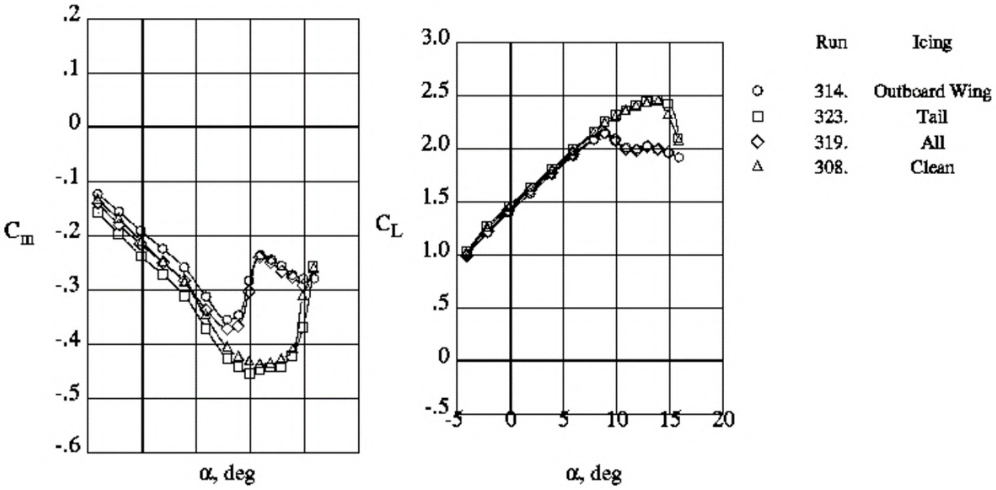

Figure 2.13: Effects of Ice #2 on longitudinal aerodynamic characteristics of the model in the $\delta_f = 40°$ configuration, after Reehorst et al. [9]

a series of ice accretions on a semispan wing with a GLC-305 section and parameters $\Lambda_{c/4} = 25°$, $AR = 6.8$, $\lambda = 0.24$, as well as a washout of 4°. This wing was intended to be representative of modern business jet and regional jet aircraft wing planforms. High-fidelity polyurethane castings were made for six ice accretion taken at the NASA Glenn Icing Research tunnel for dry-air aerodynamic testing, including a number of highly-three dimensional scallop shapes, Fig. 2.16. The six ice shapes consisted of five glaze shapes, which were either complete or incomplete scallops, and one streamwise/rime shape (IRT-SC5). One of these glaze shapes, IRT-CS22, was unrealistically large and had outlying performance penalties. The following discussion refers to the remaining four glaze shapes, as they have the greatest relevance to this thesis. The dry-air aerodynamic testing of these shapes is described by Papadakis et al. [11]. The aerodynamic testing model was fitted with three rows of pressure taps and was mounted on a force balance to investigate the performance effects of each ice geometry. Unfortunately, no flow visualization techniques were employed for these tests.

The pressure coefficient distributions in Fig. 2.17 show a significant alteration of clean-wing flowfield. The effect of leading-edge ice ranged from a reduction of the suction peak to the pressure-plateau characteristic of a separation bubble aft of the ice shape with the complete scallop shapes. The pressure distributions appear to show separation beginning at the tip advancing inboard in the form of a large separation bubble. By 8° angle of attack, the flow is separated for most shapes at least past 50% span. This matches the performance data shown in Fig. 2.18, which shows stall beginning for the complete scallop shapes in the neighborhood of 7° to 10° (see shapes IS10, CS10, IPSF22.) Ultimately, the three rows of pressure taps provided few conclusions regarding the finer details of the flowfield. Overall, the results of the test confirm the observations of other studies that found the iced flowfield for glaze ice shapes to feature leading-edge separation and a tip-stall phenomenon.

This review has covered a range of past investigations of the effect of swept-wing ice on performance and the flowfield. These studies were often limited in some way, whether in the simplicity of the simulated ice, the lack of complete flowfield diagnostics, or in the Reynolds number range. Section 2.3.2 describes the collaborative, multi-phase research effort sponsored by NASA, the FAA, and ONERA that has been undertaken to create a more comprehensive database of the aerodynamic effects of swept-wing ice. Specifically, this review will focus on the portions of the project aimed at finding the level of geometric fidelity needed to accurately predict the aerodynamics.

Figure 2.14: 3.5% Scale GTM installed in the NASA Langley 12-ft Low-Speed Wind Tunnel C-sector mounting and positioning system, after Broeren et al. [10]

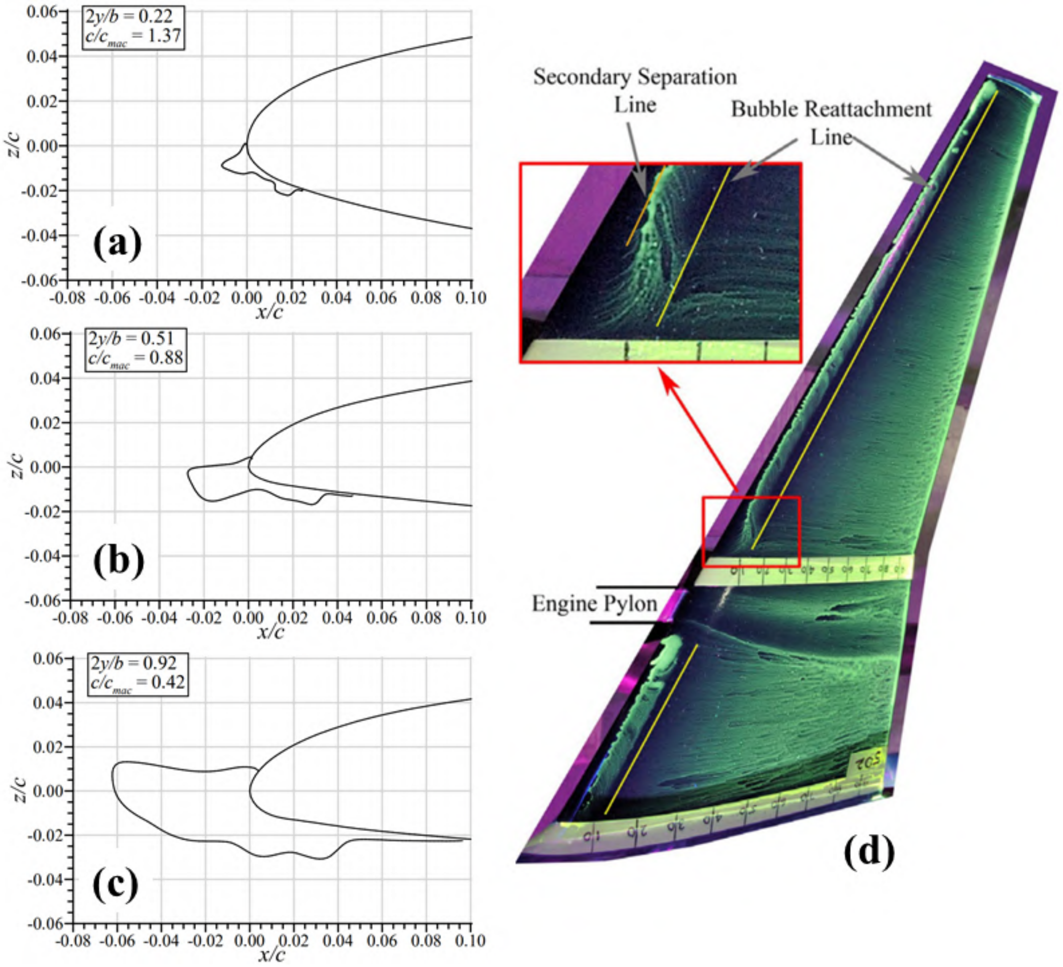

Figure 2.15: Cross-section view of wing ice shape at three spanwise locations on the 3.5% scale GMT, after Broeren et al. [10]: (a - c); (d) Surface-oil flow visualization on the clean wing for $\alpha = 8^\circ$. Flow is from left to right.

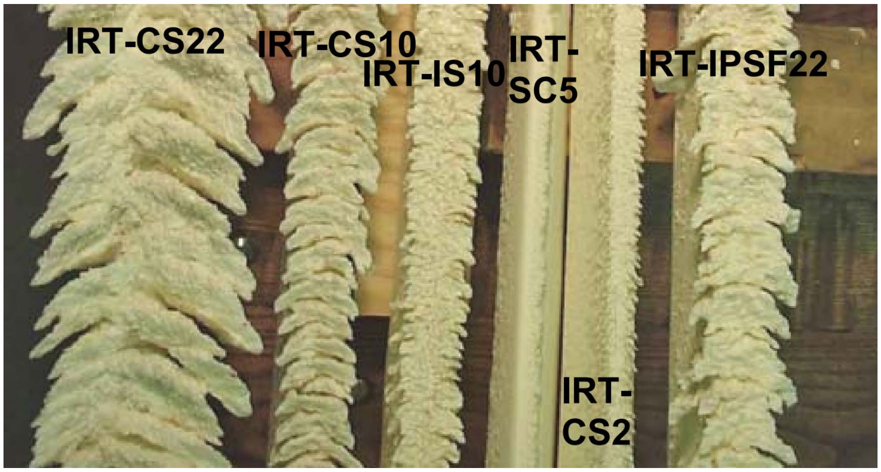

Figure 2.16: Polyurethane castings of the six ice shapes obtained from icing tests at IRT, after Papadakis et al. [11]

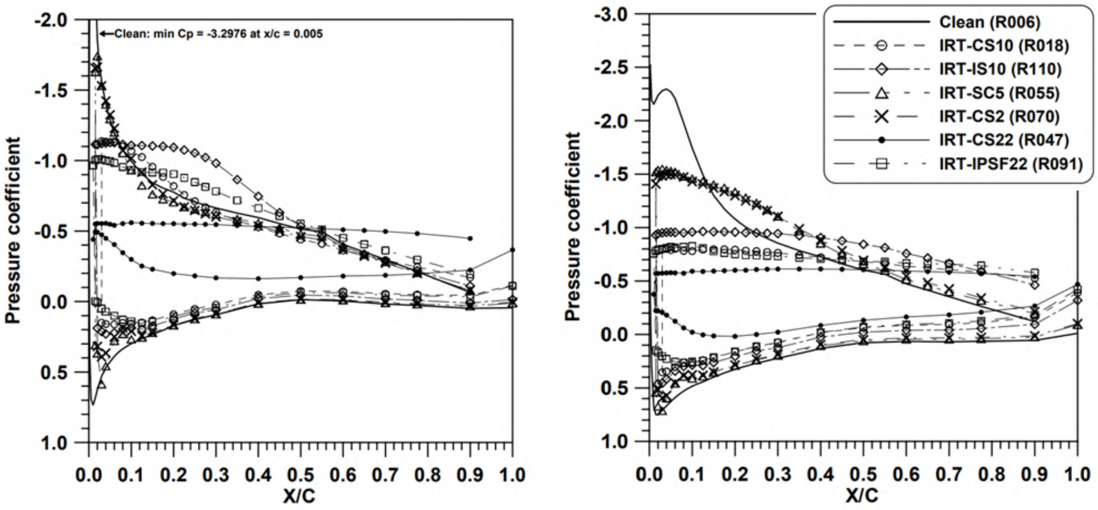

(a) **(b)**

Figure 2.17: Effect of IRT ice shapes on pressure distributions at 15% semispan, $Re = 1.8 \times 10^6$, after Papadakis et al. [11]; (a) $\alpha = 8^\circ$; (b) $\alpha = 12^\circ$;

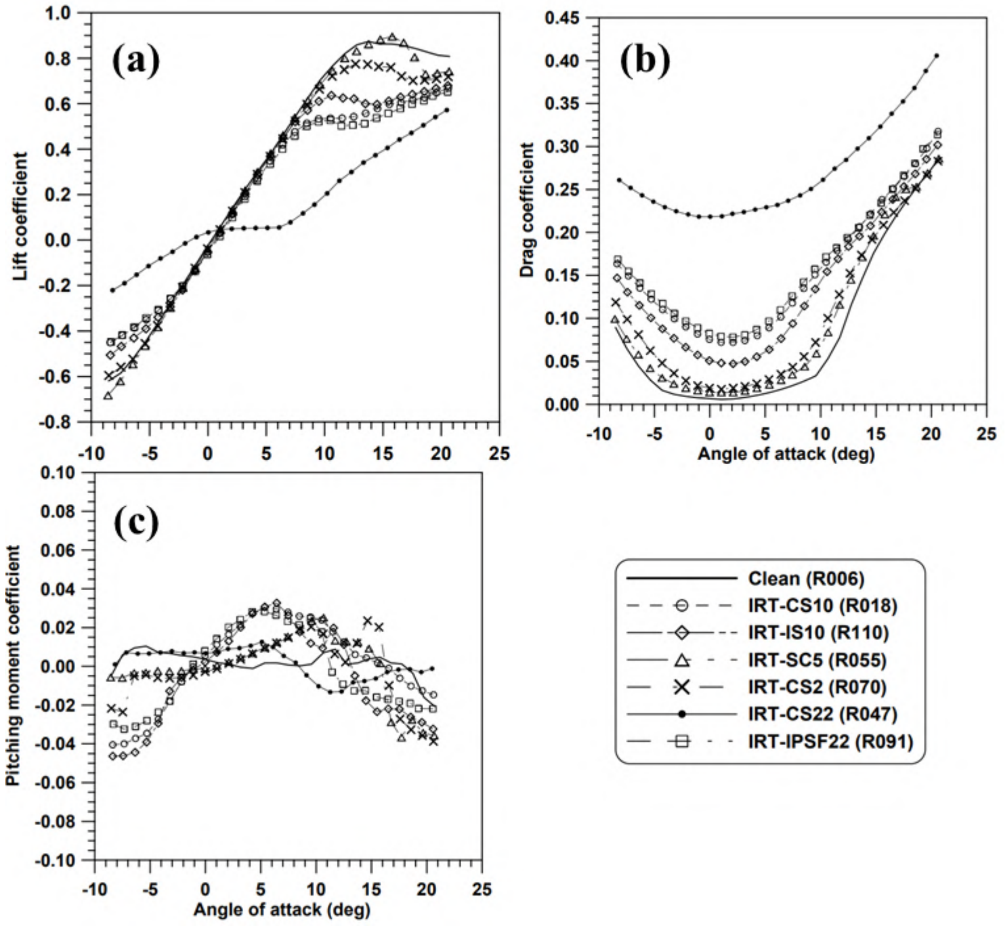

Figure 2.18: Effect of IRT ice shapes ON C_L, C_D, and C_M at $Re = 1.8 \times 10^6$, after Papadakis et al. [11]

2.3 Icing Fidelity Studies and Fundamental Geometries

Finding the necessary level of ice shape fidelity is important for the simplification of experimental and numerical research. As a note, fidelity refers to the level of realistic three-dimensional details from the original ice accretion that are included in the leading-edge simulated ice shape. Extensive work was done to determine the necessary fidelity level for airfoil ice accretions. Eventually, it was determined that using simple geometry with known effects on the flow was sufficient to recreate the aerodynamic effect and general flowfield. This, in turn, enabled the parametric study of airfoil ice shapes, such as horn ice and spanwise-ridge ice. These simple geometries could be moved and modified to gain insight into the impact of different factors on the airfoil performance.

The study of swept-wing ice fidelity is not as mature, nor as straightforward as it is for airfoils, especially in the case of ice accretions with high levels of three-dimensionality. Recent studies on the aerodynamics of this type of swept-wing ice provide new insight, but questions remain about certain aspects of the flowfield, some specifically regarding the Type I and Type II flowfields, first mentioned in the introduction.

The current study takes an approach similar to the study of iced-airfoil aerodynamics to address this uncertainty. That is, the present work uses a simple 2-D geometry with a desired effect on the flowfield, and modifies it to study the effect on lifting surface performance. Specifically, a variation on a swept backward-facing step is used to reproduce the separation bubble and spiral vortex observed in some low-fidelity ice shapes. Then, the step is modified with discontinuities to study the flowfield. This section of the review will give an overview of 2-D icing studies that made use of simple geometries as low-fidelity ice shapes. Then, the motivation and basis for the current work will be given with a review of recent swept-wing fidelity studies. Finally, as a comparison to the swept-wing flowfields discussed prior, studies on the swept backward-facing step will be reviewed.

2.3.1 Iced Airfoil Fidelity

The aerodynamics of airfoil ice are conducive to representation by simple geometries. For horn ice and spanwise-ridge ice, it has been shown that spanwise variations from the realistic ice geometry are not wholly necessary to recreate the proper aerodynamic effect. As a note, the drag is particular is more accurate when some of the 3-D features are included. Despite the vorticity and cell-structures present behind a high-fidelity horn ice shape, Gurbacki [2] showed that a two-dimensional smooth shape captured the aerodynamics and flow physics appropriately. Broeren et al. [53] had similar conclusions for spanwise-ridge ice, as well as horn ice. Operating on the observation that the flowfields of these ice shapes were primarily two-dimensional, several parametric studies were made to estimate the effect of variations on each type of ice. This type of study was enabled by thorough knowledge of the iced-airfoil flowfield, through which a proper simple geom-

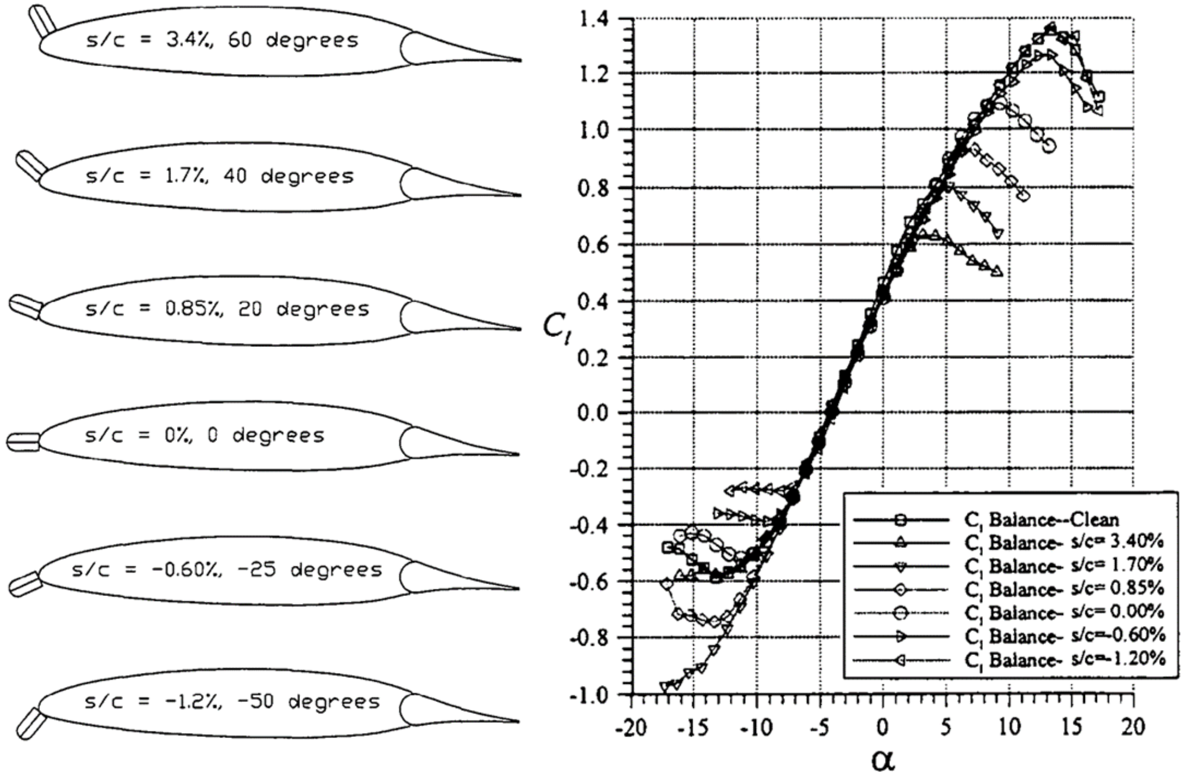

Figure 2.19: (left) Simulated horn ice shape locations and angles, (right) Position effects on C_l for ice shape with horn radius to width ratio $r/w = 0.5$ and height $h = 0.8$" at $Re = 1.8 \times 10^6$. Adapted from Kim and Bragg [12]

etry was selected. First, experiments showing the application of simple geometries to approximate horn ice will be reviewed. Then, a description of spanwise-ridge ice will be given, along with a review of several studies similar to those conducted for horn ice.

Simple Horn Ice Simulations

The aerodynamics of horn ice, as previously described in Section 2.1, are predominantly influenced by the separation bubble that begins at the horn tip. To recreate this important flow feature, researchers have utilized simple protuberances affixed near the leading edge as an approximation of a horn. In this manner, Kim and Bragg [12] applied horn ice simulations to an NLF(1)-0414 airfoil, which was designed to have a relatively long stretch of laminar flow along its upper surface. For this parametric study, the effects of horns of varied size, shape, and position were compared using force balance, surface pressure taps, and wake pressure measurements. The simulated horns had three tip radii, ranging from a sharp point to 50% of the base width The shapes were also constructed in three different sizes, with a height range of $k/c = 2.00\%$ to 6.67%. These dimensions were based upon averaged measurements of real ice accretions from what was then the NASA Lewis Icing Research Tunnel. Finally, horns were positioned at six wrap distances relative to the leading edge, pictured in Fig. 2.19. Using these simplistic simulations of horn ice to recreate the separation bubble yielded several notable results. Specifically, there is a significant relationship between the horn height and the reduction in lift, Fig. 2.19, which was coupled with a dependency on the surface position of the horn. It was also observed that variations in the horn tip radius and Reynolds number had a small effect compared to the other geometric variables.

Using the finding of Kim and Bragg [12] that the tip radius of the simple horn did not affect the aerodynamics significantly, Manshadi and Esfeh [13] used only the 50% base-width radius horn on a NACA 0012 airfoil. Two heights of this shape were used: $k/c = 2.00\%$ and 4.33%. This study used surface pressure and hot-wire measurements to investigate the unsteadiness of the flowfield. These unsteady measurements included a spectral analysis of velocity fluctuation, including the shear layer flapping and regular frequency modes introduced in Section 2.1.3. The Strouhal numbers associated with these modes compared well to previous studies, including those by Gurbacki [2] and Bragg et al. [54], both of whom used higher-fidelity horn ice shapes. Hot-wire measurements of turbulence intensity are shown in Fig. 2.20, showing the turbulent shear layer growing from the horn shape, experiencing the greatest fluctuations above the reattachment zone. In this and other respects, the flow behind a horn is similar to the flow behind a backward-facing step.

Another parametric study of simulated horn ice was conducted by Papadakis et al. [14] using thin metal spoiler plates as horn simulations on two NACA 0011 airfoils. The height, angle, and surface position of the spoilers were varied, along with the Reynolds number. Resulting force balance and surface pressure data echoed the findings of Kim and Bragg [12], in that increasing horn height generally increased the lift and drag penalties, with a dependence upon the surface position. Stall angle was observed to decrease significantly, and Reynolds number effects were relatively small. Accompanying numerical analyses using the Reynolds-Averaged Navier-Stokes equations showed the large separation bubble and a series of vortices, both upstream and downstream, Fig. 2.21.

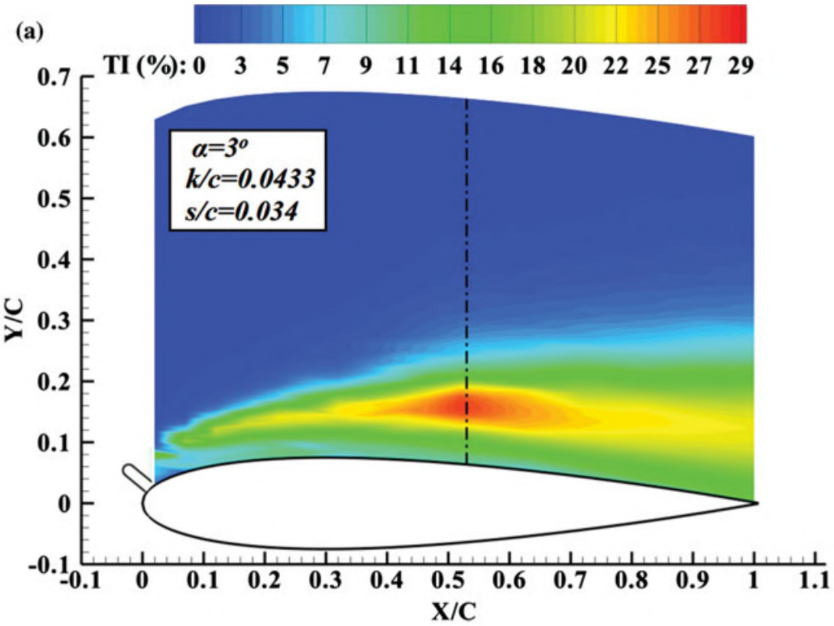

Figure 2.20: Contour of turbulence intensity, $\alpha = 3°$, $Re = 1.0 \times 10^6$, after Manshadi and Esfeh [13] (Reattachment location is marked with a dashed line).

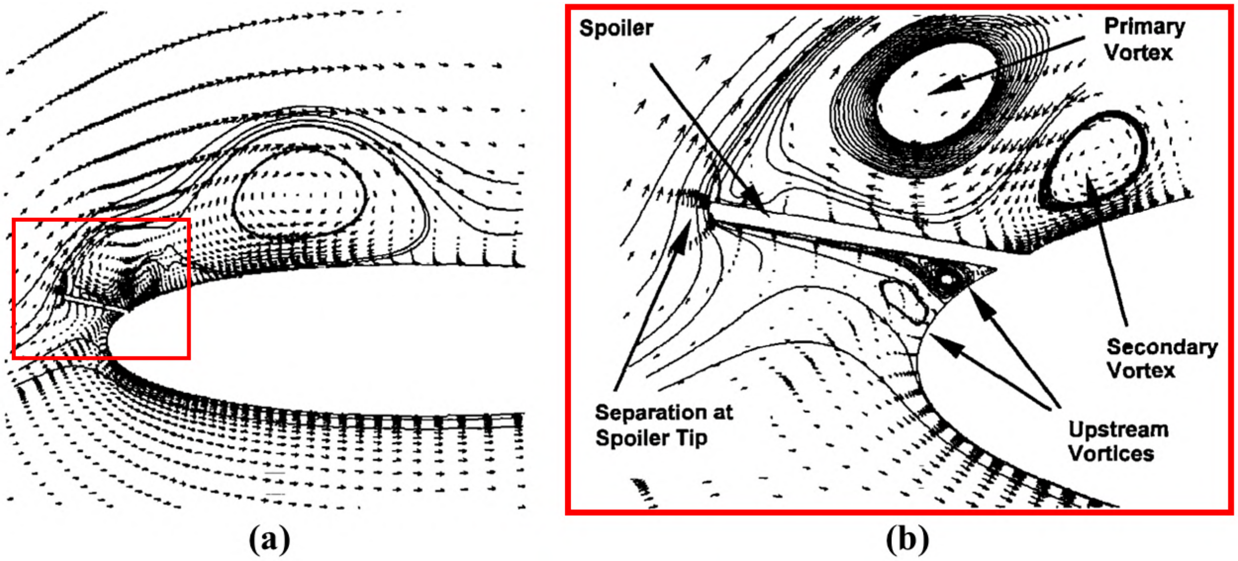

Figure 2.21: Velocity vectors and streamlines from RANS computations; NACA 0011, $\alpha = 5°$, $h = 1.5$", $s/c = 0.02$, $\theta = -80°$, $Re = 1.86 \times 10^6$, after Papdakis et al. [14]

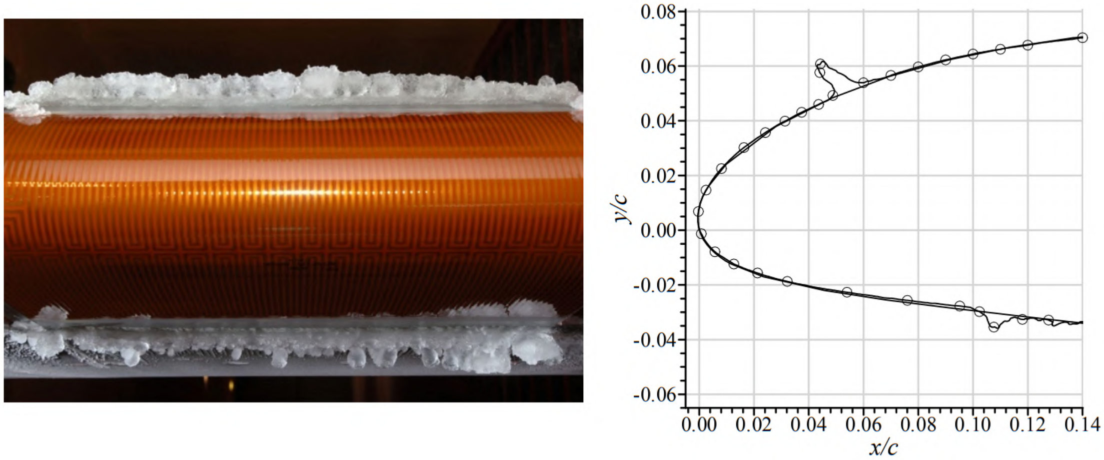

Figure 2.22: Photograph and tracing of a spanwise ridge ice accretion on a NACA 23012 airfoil. Adapted from Broeren et al. [15]

Simple Spanwise-Ridge Ice Simulations

Spanwise-ridge ice is one of the main aerodynamic classifications of airfoil ice introduced by Bragg et al. [1]. This type of ice accretion forms as water droplets flow downstream along the wing surface and freeze, forming a ridge shape. An example of this type of ice is shown in Fig. 2.22. Spanwise-ridge ice typically forms just aft of a de-icing boot or leading-edge de-icing heater that fails to evaporate all of the impinged water. Physically, spanwise-ridge ice is characterized by height, location, geometry or shape, and spanwise uniformity. These factors have important implications for the aerodynamics, which are largely determined by a separation bubble, as with horn ice, but with the added complication of a developing boundary layer. A diagram of this flowfield forming around a simple ramp approximating a spanwise-ridge shape is shown in Fig. 2.23.

Calay et al. [16] investigated the aerodynamic effects spanwise-ridge ice with three ramp shapes, pictured in the legends of Fig. 2.24, on a NACA 0012 airfoil. Each ramp had a height of $h/c = 0.35\%$ and a width of $w/c = 1.4\%$, and was positioned at one of three chordwise positions, $x/c = 5\%$, 15%, or 25%. The effects of these shapes were measured at $Re = 1.25 \times 10^6$ using a force balance, surface pressure taps, and a wake pressure rake. The rake was mounted 0.065 chord lengths downstream of the airfoil. The addition of the ramps resulted in a disruption of

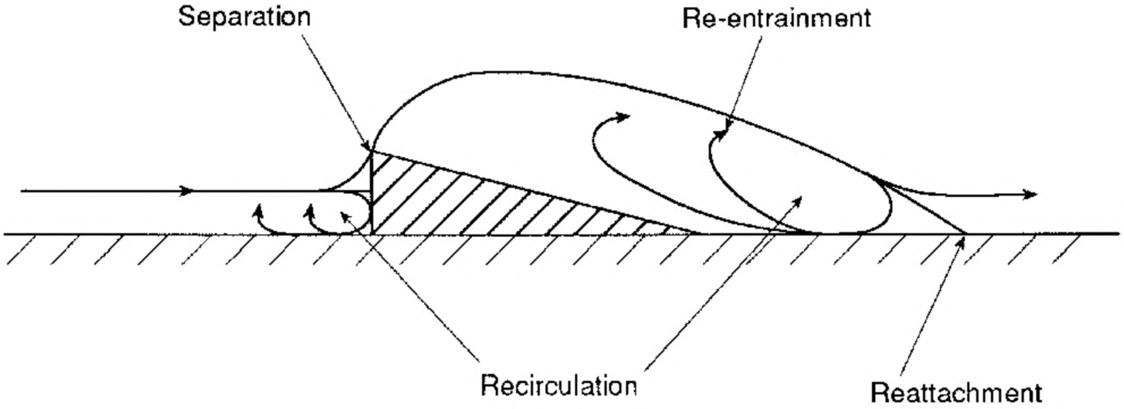

Figure 2.23: Typical representation of flowfield around a simulated spanwise-ridge ice shape, after Calay et al. [16]

the clean pressure distribution, creating a high-pressure trough forward of the shape and a suction peak aft. Performance penalties, which included higher drag and lower lift-curve slopes and stall angle, decreased as shapes were placed further aft. This is illustrated in the wake profiles for the simulated ice at two chordal positions, Fig. 2.24. In these plots, the velocity deficit is seen to vary consistently between ramp shapes, but also between the chordal position, with $x/c = 0.05$ exhibiting the greatest deficits. Even for geometry with a small height relative to the chord, these results show that spanwise-ridge shapes can have strong effects on the performance and flowfield.

In a series of experiments, Lee and Bragg [55, 17] applied several simple spanwise-ridge simulations to both a NACA 23012 and a NLF-0414 airfoil. The shapes included backward- and forward-facing quarter-rounds, a half-round, and forward-facing ramp. Grit and boundary layer trips were also employed to simulate ice roughness. The baseline forward-facing quarter-round shape is shown on the NACA 23012 airfoil in Fig. 2.25. It was this particular geometry that served as the inspiration for the swept backward-facing step studied in this thesis. The effects of each spanwise-ridge simulation were quantified with a force balance, surface pressures, and wake pressures. Surface oil flow was used for a qualitative picture of the flowfield development. In addition to severe penalties on lift and drag, similar to Calay et al. [16], Lee and Bragg [55] saw significant differences between the two airfoils tested. The NACA 23012 had a forward-loaded pressure distribution and a strong adverse pressure gradient in the recovery region. The addition of the simple ice shapes within this region resulted in a much larger separation bubble, which grew rapidly with angle of attack, Fig. 2.26. The NLF-0414 airfoil, designed for laminar flow, had a much milder adverse pressure gradient. As a result, the airfoils had widely varying relationships between performance penalty and chordwise ridge position.

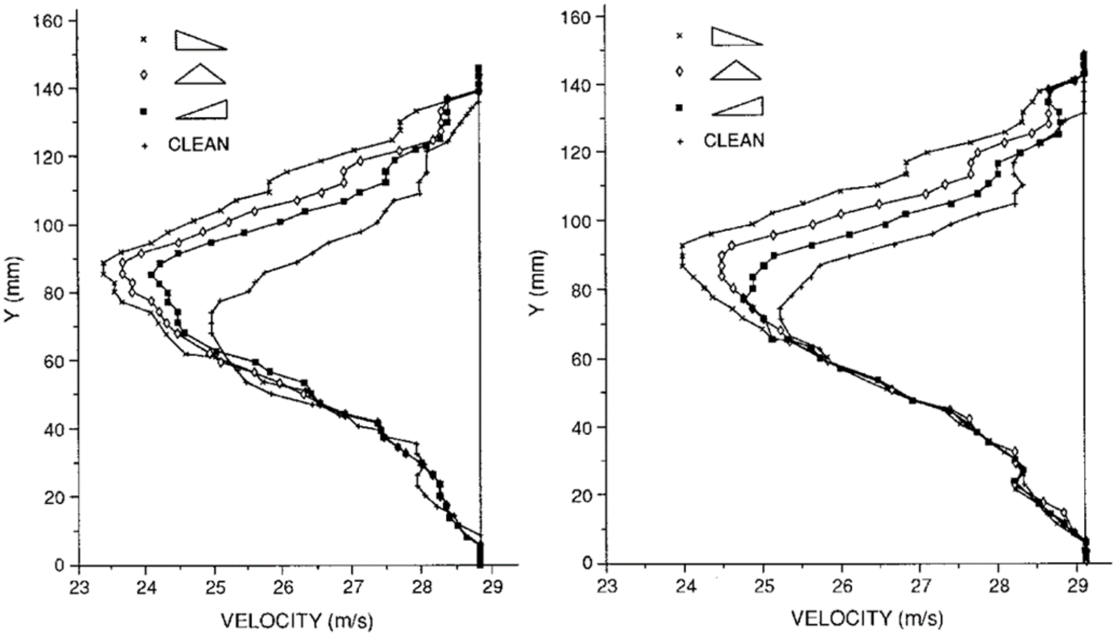

Figure 2.24: Wake velocity profiles for different ice shapes, after Calay et al. [16]; (left) $x/c = 0.05$; (right) $x/c = 0.25$

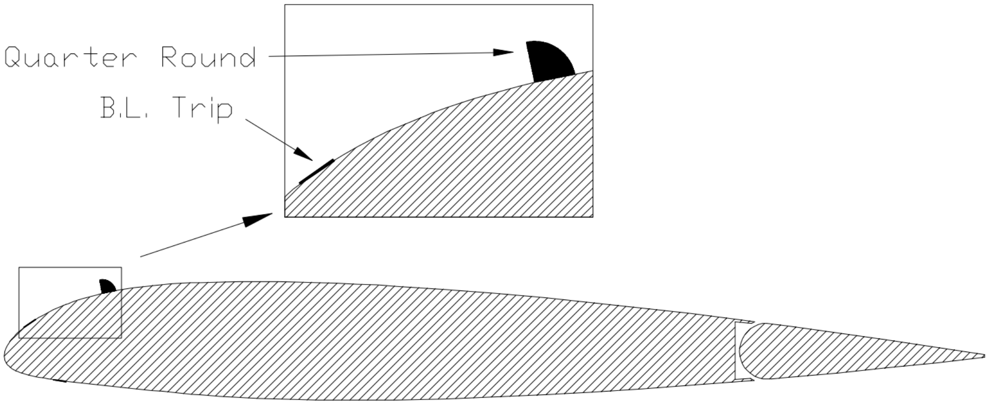

Figure 2.25: NACA 23012 model with quarter round ice simulation. (0.25” quarter round at x/c = 0.10 shown), after Lee and Bragg [17]

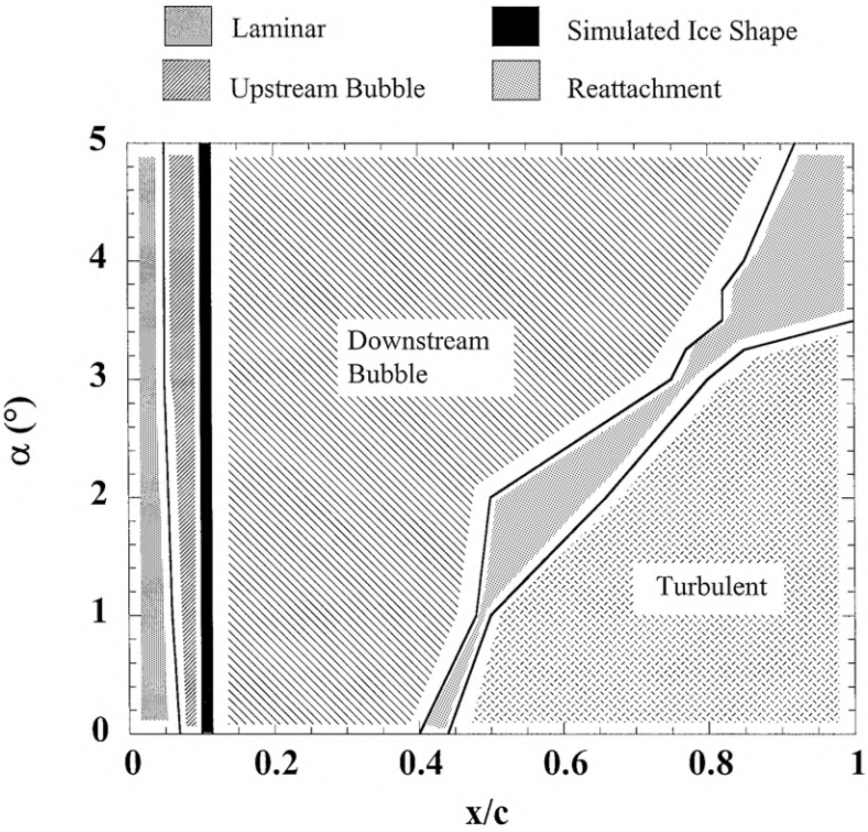

Figure 2.26: Summary of boundary-layer state on the NACA 23012 airfoil with 0.25-in. quarter-roung simulated ice shape at $x/c = 0.10$ obtained from flow visualization. Natural transition. $Re = 1.8 \times 10^6$, after Lee and Bragg [17]

2.3.2 Iced Swept-Wing Fidelity

The previous section of this review focused on the use of simple geometries to recreate key flow features and thus study their effects on lifting surfaces. This type of study was applied to good effect and led to many interesting findings and ultimately, an improved understanding of the effect that certain types of ice accretion have on airfoils. As the review of scallop ice in Section 2.2.1 showed, ice accretions with substantial spanwise variation can occur on swept wings, which in turn complicates the aerodynamics. Bragg et al. [45] classified swept-wing ice shapes by similar aerodynamic effect as part of the effort toward determining the appropriate level of geometric fidelity for accurate aerodynamics. That review incorporated new research and built upon an earlier aerodynamic classification of swept-wing ice shapes by Broeren et al. [56]. The latest classifications described in that paper are as follows:

- Leading-edge roughness
- Streamwise ice
- Spanwise ridge
- 3-D leading-edge horn
- Highly 3-D leading-edge horn

The primary focus of this paper relates to the 3-D leading-edge horn and highly 3-D leading-edge horn shapes; therefore, special consideration will be given these two classes to provide the necessary context to the results of this paper. 3-D leading-edge horns shapes and highly 3-D leading-edge horn shapes, which are both derived from the classification of airfoil horn ice, are differentiated by the level of spanwise variation in the horn ice accretion, as well as the presence or absence of a separation bubble. These classifications are based upon limited experimental results, much of which have been collected during the SWIP research program.

First described in the introduction, SWIP is a collaborative, multi-phase research effort sponsored by NASA, the FAA, and ONERA, with assistance from the University of Illinois at Urbana-Champaign, University of Virginia, and the University of Washington. The overarching objective of SWIP is to address a need for knowledge on swept-wing icing that is important to the design, certification, and safe operation of small and large transport aircraft. This objective is accomplished primarily with two major efforts. The first is to develop an experimental ice accretion database for large, swept wings for the evaluation of numerical icing simulation tools [57, 58]. The second is to experimentally assess the aerodynamic effects of swept-wing ice, including Reynolds and Mach number effects and varied geometric fidelity. A more detailed description of the project and its motivations is given by Broeren et al. [56]. The model used for all tests was the semispan wing from a 65% scale version of the Common Research Model, referred to as CRM65. The CRM65 wing has a modern transonic supercritical design with favorable aerodynamic properties, even without the standard engine nacelle and pylon, which is the configuration used for this project. Other properties of the wing are: $\Lambda_{LE} = 37.15^\circ$, $\lambda = 0.28$, and $AR = 9.0$.

For the first thrust, testing was performed in the NASA Glenn Icing Research Tunnel to acquire the database of ice accretions. Due to the size of the full-scale reference wing, tests were performed on specially designed hybrid wing models meant to capture the full-scale CRM65 leading edge at three stations along the span [34]. The conditions for the icing tests were based on holding conditions for a CRM65 aircraft in the Code of Federal Regulations, Part 25, Appendix C, Continuous Maximum. From these ice accretions, full-span artificial ice shapes were designed and manufactured for 8.9%-scale and 13.3%-scale models of the CRM65 semispan wing. This process, described by Camello [37], uses laser scanning to acquire 3-D digital images of the ice accretion, which are subsequently interpolated and extrapolated from the three spanwise ice accretion sections. The ice shapes developed from the laser scans contain all of the three-dimensional properties of the original ice shape. In terms of fidelity, these ice shapes are called "high fidelity," meaning that they are the most detailed ice shapes available, accounting for the limitations of the methods employed. Ice shapes were constructed using stereolithography (SLA) 3-D printing, and could be attached to the wing models via a removable leading edge.

The models and the various leading-edge ice simulations were tested in dry-air wind tunnels, with the 8.9%-scale wing for low-Reynolds number testing, and the 13.3%-scale model for high-Reynolds number testing. The models are shown installed in Fig. 2.27. Low-Reynolds number testing was performed at the Walter H. Beech wind tunnel at Wichita State University, and high-Reynolds number testing was performed at the ONERA F1 facility. This review is primarily concerned with the low-Reynolds number test results. Data were collected with force balance measurements, surface pressure taps, and fluorescent mini-tuft flow visualization. During low-Reynolds number testing, wake pressure surveying and fluorescent surface oil flow was also done.

Broeren et al. [38] describes the aerodynamics of the CRM65 wing model. Before stall, flow over the clean wing was attached with turbulent transition occurring outward from the root. Flow separation during stall initiated from the tip first, as is often characteristic of swept wings.

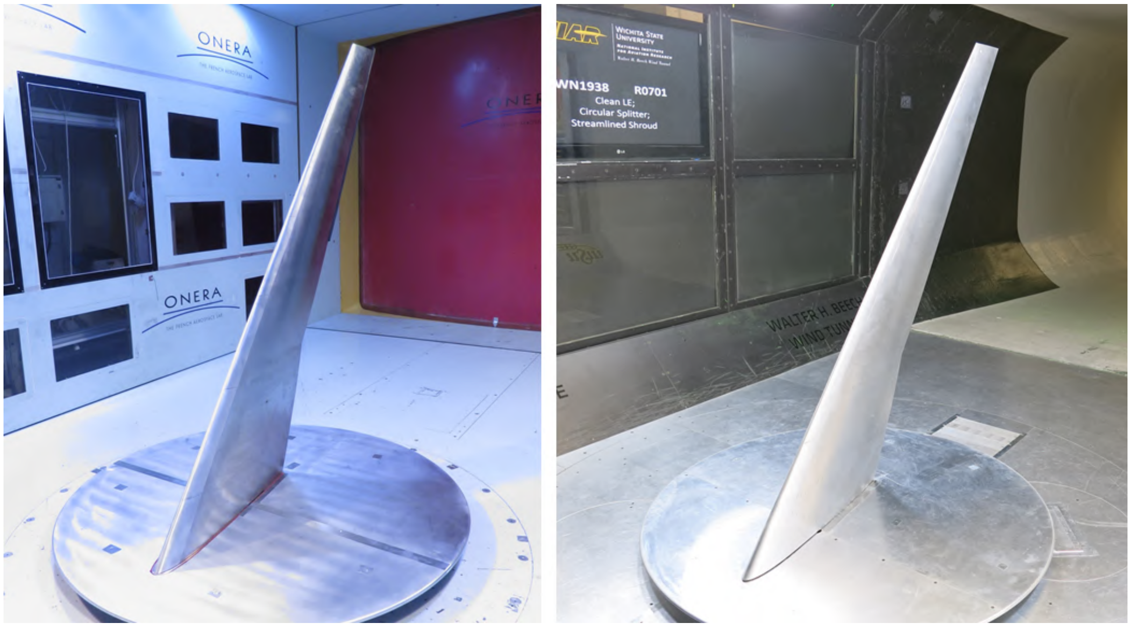

Figure 2.27: Photographs of the upper surface of subscale CRM65 semispan wing models installed in their respective wind tunnels; left: 13.3% scale CRM65 semispan wing installed in ONERA F1 test section; right: 8.9% scale CRM65 semispan wing installed in WSU test section.

However, this portion of the review will discuss a series of fidelity studies completed as part of the SWIP program for a scallop ice shapes that falls under the classification of highly 3-D leading-edge horn. It is this classification of swept-wing ice accretion that is the most complex and requires further study, as the current work endeavors to do. The scallop shape in question is referred to as the ”Maximum Scallop,” which had distinct complete scallops at all three spanwise stations. The Maximum Scallop was a result of a temperature sweep while other icing conditions were held constant. Photographs of the Maximum Scallop are shown in Fig. 2.28.

For this particular ice shape, in addition to the high-fidelity artificial ice shape, various low-fidelity variations were built as well. This was done as part of the investigation of the necessary level of fidelity required for accurate aerodynamic simulation of swept-wing ice. One such low-fidelity shape is referred to as the 3-D smooth, which was developed by taking section cuts of the ice shape along the span, which were smoothed and then lofted to make a new full-span ice shape [37]. While this shape is three-dimensional in that it varies in cross-section along the span, it eliminates the scallops that make the original shape highly three-dimensional. A variation on

Figure 2.28: Photographs of the Maximum Scallop ice shape at the three spanwise locations, after Woodard et al. [18]

the 3-D Smooth was also tested that included roughness from grit applied to the ice shape surface. This was intended to recreate some of the realistic roughness present in the high-fidelity shape. In between the 3-D smooth and the High Fidelity, several artificial ice shapes were developed to investigate the sensitivity of the flow to spanwise discontinuities similar to scallop ice and the gaps between them. Referred to as ”3-D Discontinuous,” these shapes are developed simply by removing material from the 3-D Smooth, resulting in a spanwise array of gaps and features. Several of these shapes are shown in Fig. 2.29. More details on the development and design are given by Woodard et al. [22, 19]. In total, six 3-D Discontinuous shapes were manufactured and tested, each varying in gap and feature widths or the cutting plane that shaped the discontinuities.

Woodard et al. [19] provided the latest review of testing results for the Maximum Scallop and its low-fidelity counterparts. One conclusion from these results was that the 3-D Smooth was not an accurate approximation of the high-fidelity aerodynamics or flowfield. Specifically, the aerodynamic penalties of the 3-D Smooth were less than that of the High Fidelity ice shape. Additionally, the 3-D Smooth flowfield was dominated by a series of spanwise vortices while the high fidelity Max Scallop contained periodic streamwise features, seen as streamwise streaks in the surface oil flow, Fig. 2.30. Differences are further illustrated in the surface pressure distribution,

Fig. 2.31. The 3-D Smooth exhibits pressure plateaus, confirming the presence of the spanwise vortices, whereas the high fidelity maintains a suction peak. The comparison between the 3-D Smooth and High Fidelity was also explored by Camello [59], Sandhu [60], and Woodard et al. [18].

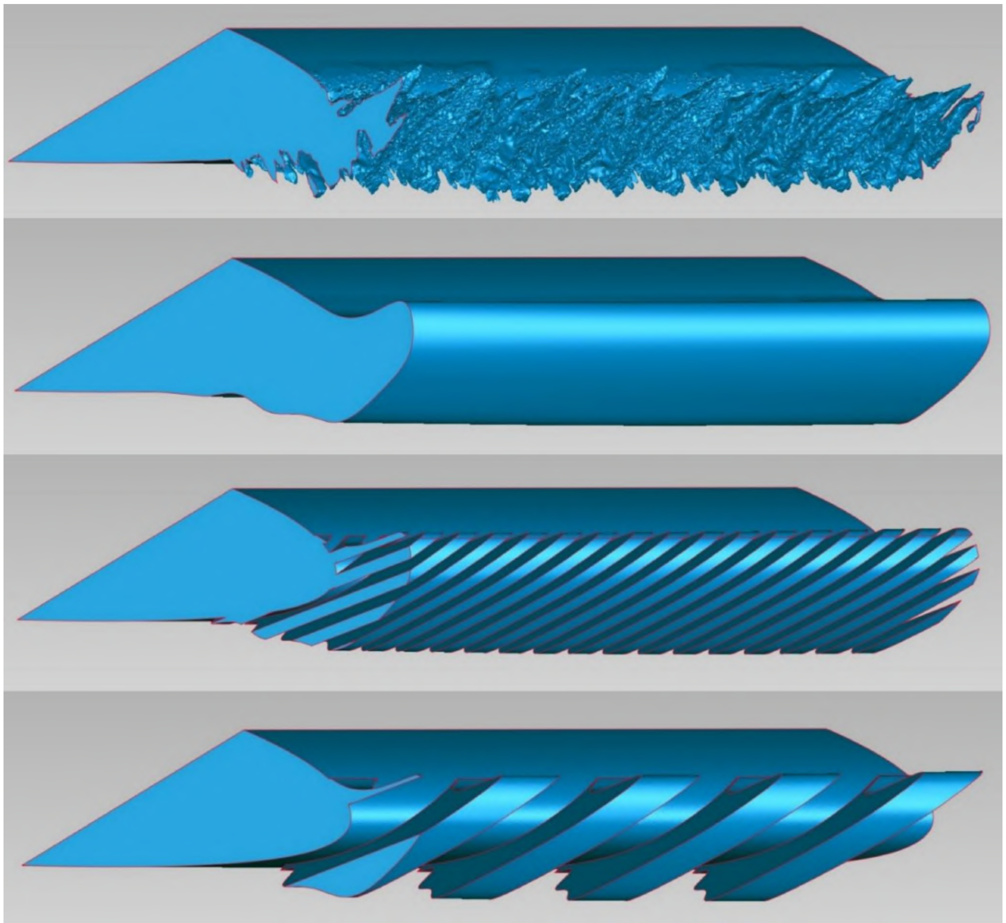

Figure 2.29: Renderings of artificial ice shapes. From top to bottom, the ice shapes are: Maximum Scallop High Fidelity, Maximum Scallop 3-D Smooth, Small Gap 3-D Discontinuous, Medium Gap 3-D Discontinuous.

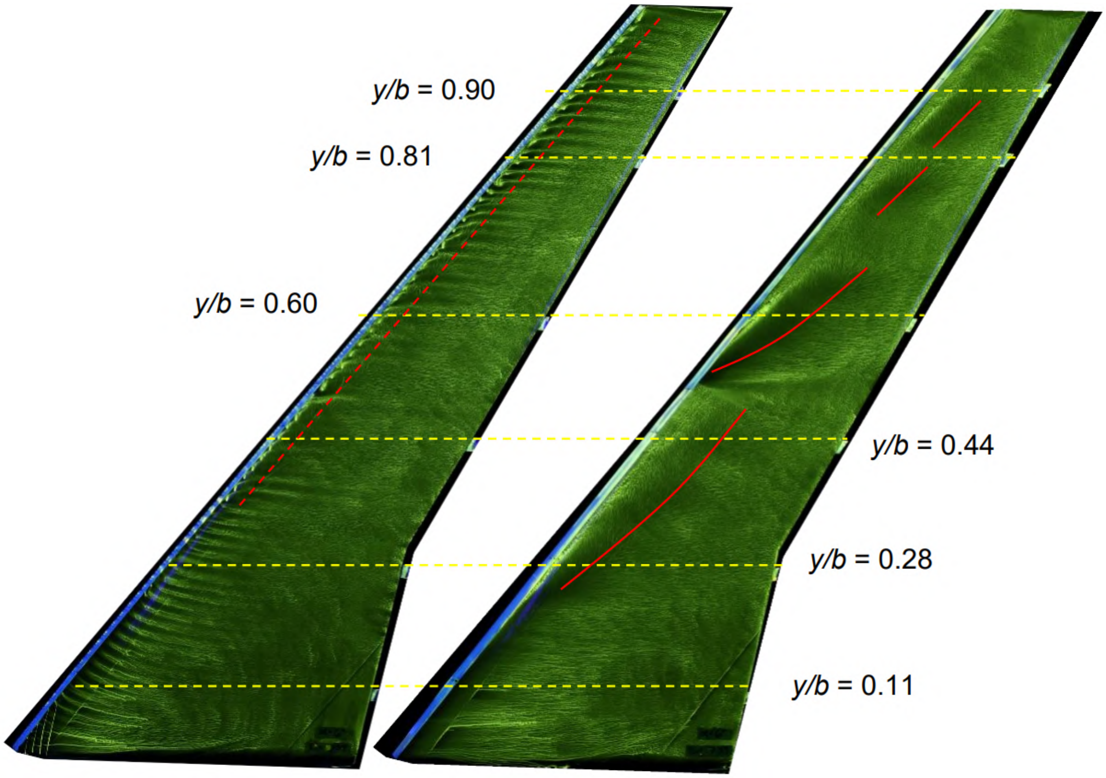

Figure 2.30: Surface oil flow visualization for the High Fidelity and 3-D Smooth ice shapes at $\alpha = 6.4°$ illustrating the characteristics of Type I and Type II flowfields. Reattachment indicated by a solid red line. Suction side shown with flow from left to right, after Woodard et al. [19]

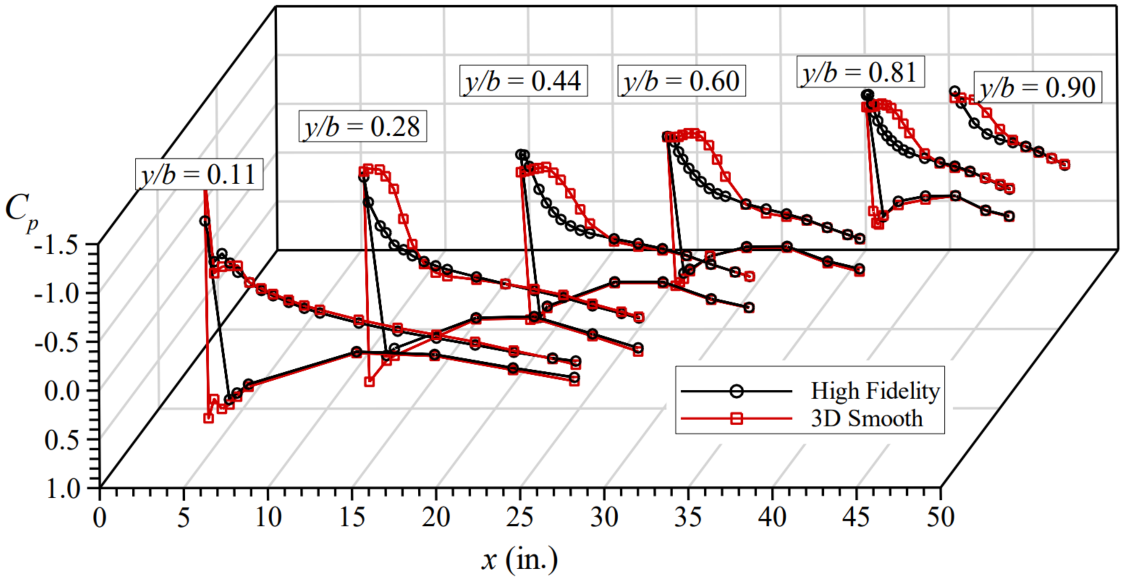

Figure 2.31: Pressure distributions for the High Fidelity and 3-D Smooth ice shapes at $\alpha = 6.4°$ illustrating the characteristics of Type I and Type II flowfields, after Woodard et al. [19]

Wind tunnel testing of the 3-D Discontinuous variants of the Maximum Scallop provided new insights as to the sensitivity of the flow to spanwise variations. The 3-D Discontinuous shapes resulted in integrated performance that was closer to the High Fidelity than the 3-D Smooth, but still not an accurate recreation of the aerodynamics. Upon further analysis of surface oil flow visualization, the 3-D Discontinuous shapes possessed streamwise streaks akin to the High-Fidelity, but with variations in the geometric spacing. For example, a region of streamwise streaks is compared at the same angle of attack for the High Fidelity, the Small Gap, and Medium Gap 3-D Discontinuous shapes, Fig. 2.32. A close-up view reveals differences in the periodic streamwise feature spacing. For the Maximum Scallop, the spacing of the streaks could not be directly associated with any one of the many significant spanwise variations in the ice shape geometry. In contrast, 3-D Discontinuous shapes with larger gaps had streamwise feature spacing that matched that of the gaps. However, this was not the case for the Small Gap 3-D Discontinuous shape, which had the smallest gap spacing of the low-fidelity variants. In this case, the spacing of the streamwise features varied across the span and with angle of attack. Woodard et al. [19] theorize that this may be a result of an instability in the shear layer that forms as the flow separates at the ice shape.

Overall, Woodard et al. [19] also report two general trends in the flowfield of the Max Scallop shape and its variants. One general flowfield is dominated by spanwise leading-edge vortices generated by flow separation originated from the leading-edge ice accretion. This type of flowfield is referred to as Type I. Another, designated as Type II, lacks the spanwise vortices, and shows evidence of streamwise vorticity in the form of streamwise streaks seen in surface oil flow. The appearance of Type I and Type II flowfields is also noted by Broeren et al. [44] in their study of an incomplete scallop ice shape and its low-fidelity variants. The Type I/Type II nomenclature is for simplicity and due to the lack of complete understanding of the phenomena at work. The problem of Type I and Type II flowfields, along with the study of the necessary fidelity to simulate scallop ice, are the driving forces behind this thesis. The model tested in the current study is a combination of the Medium Gap 3-D Discontinuous and a swept, backward-facing step. The final section in this review of literature goes over the swept, backward-facing step as a comparison to the current geometry and the Type I flowfield.

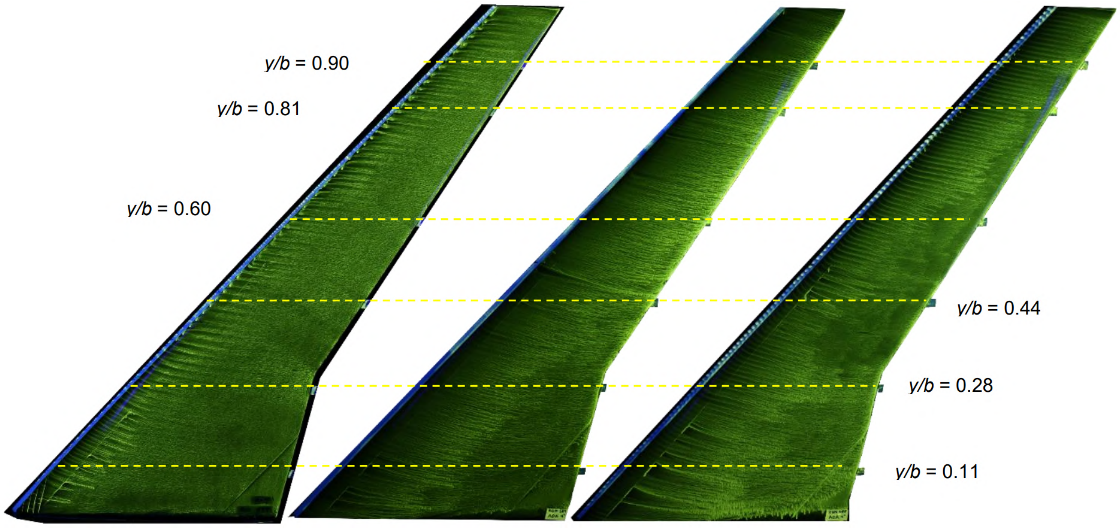

Figure 2.32: Surface oil flow visualization for the High Fidelity, Small Gap, and Medium Gap 3-D Discontinuous ice shapes at $\alpha = 4.3°$. Suction side shown with flow from left to right, after Woodard et al. [19]

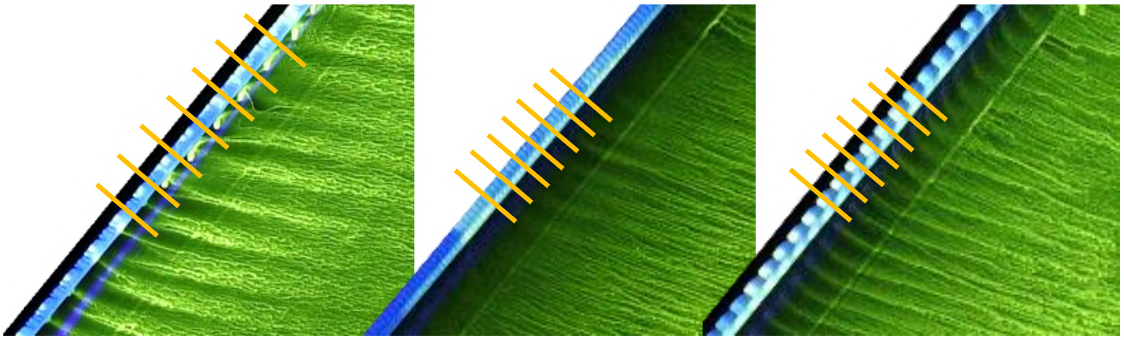

Figure 2.33: Close-up view of wing from y/b = 0.30 to 0.44 for the High Fidelity, Small Gap, and Medium Gap 3-D Discontinuous ice shapes at $\alpha = 4.3°$ with markers illustrating the period of the type II flowfield streamwise features. Suction side shown with flow from left to right, after Woodard et al. [19]

2.3.3 Swept Backward-Facing Steps

The primary design driver for the geometry tested in the current study was to approximate key flow features while reducing complexity in other areas. The 3-D Smooth is characterized by leading-edge spanwise vortices, which in some ways are comparable to the flow behind a swept backward-facing step. Both the step and the ice shape are overwhelming perturbations of the

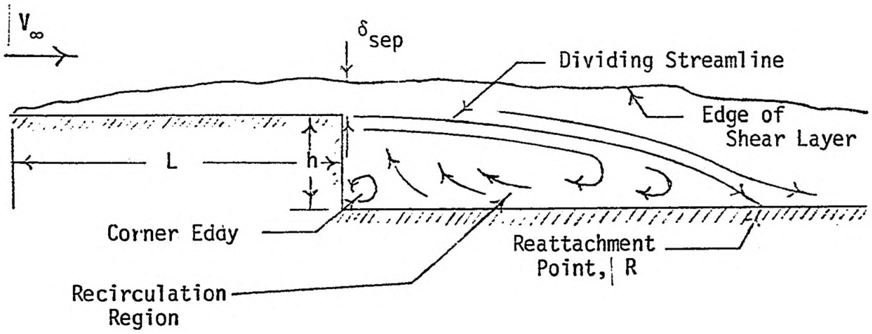

Figure 2.34: Diagram of the separated flow behind a backward-facing step, after Selby [20]

flow that lead to a separation bubble and spiral vortex. However, the number of studies of the swept, backward-facing step is limited. What may be gained from the swept, backward-facing step studies in the open literature is a fundamental comparison to ice shapes that result in a Type I flowfield, giving insight into the baseline flow physics. This may then be contrasted with results from the swept, flat plate with a discontinuous leading-edge attachment that is studied in the current research.

The backward-facing step is one of the simplest separated and reattaching flows, both in geometry and flowfield. As opposed to a surface-mounted obstacle like a spoiler, which may form a separation bubble both windward and leeward, the backward-facing step forms only one. In the most common variation of the swept, backward-facing step, a developed boundary layer flows along a flat plate before encountering the sharp expansion of the step. At the step, the flow is unable to respond to the corner and separates. A portion of the fluid forms a slow recirculation region downstream of the step face. The rest of the flow continues to form a separated shear layer. As the flow eventually turns, the shear layer impinges on the plate in the reattachment zone and bifurcates. As with the separation bubble from a horn ice accretion on an airfoil, the shear layer and reattachment location are highly unsteady. Downstream, the flow begins to recovery to a standard turbulent boundary layer. This flowfield is diagrammed in Fig. 2.34. A sketch of the resulting surface flow, as with oil flow visualization, is given in Fig. 2.35.

The most comprehensive study on the swept, backward-facing step was conducted by Selby [20, 21]. In this study, the sweep angle is varied from 0° to 60°, using step heights of 0.5” and

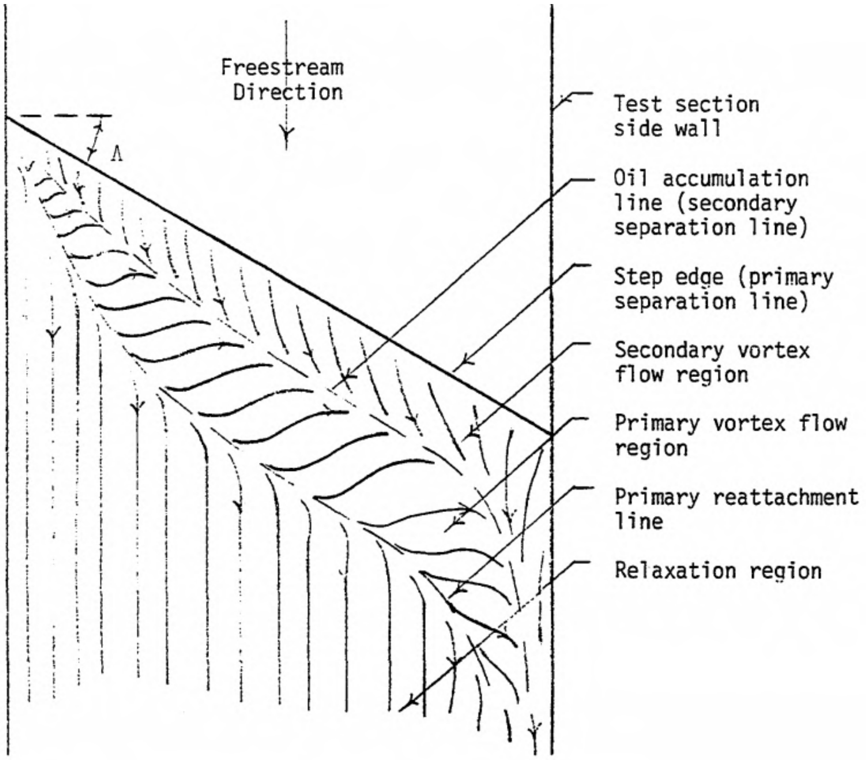

Figure 2.35: Pictorial summary of surface flow features determined from oil flow downstream of a swept, backward-facing step, after Selby [20]

0.94”. For these tests, the Reynolds numbers based on step height and freestream velocity ranged from $Re_h = 4.45 \times 10^3$ to 3.48×10^4. In addition to varying sweep angle and step height, geometric modifications were made to the edge of the step, including shallow streamwise troughs that form counter-rotating vortices, diagrammed in Fig. 2.36. These vortex troughs, which were intended to control the separated region of the flow, provide an interesting comparison to the addition of spanwise variation in low-fidelity leading-edge ice simulations. There is also some similarity to the addition discontinuities to the leading-edge step in the current research. Selby [20] found that the vortex troughs succeeded in producing longitudinal vortices that had clear effects visible in surface oil flow visualization. The periodically spaced vortices resulted in an alternating light-dark pattern, where dark regions had the oil scrubbed away. In this case, the lateral spacing of the darkened regions was approximately the same as the spacing between the vortex troughs. This was also the case for 3-D Discontinuous shapes with sufficiently large gap widths and their resulting Type II streaks. Another effect of the vortex troughs was a reduction in the mean reattachment

A) Basic base (Configuration BB) B) Conical lip (Configuration CL)

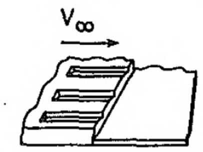

C) Vortex troughs (Configuration VT)

Figure 2.36: Backward-facing step geometries, after Selby [21]

length of the separation bubble. Finally, compared to the standard step, the step with vortex troughs also experienced greater suction seen in the pressure distribution.

Computational studies of the swept, backward-facing step have been performed by a handful of researchers, however, none with the thorough focus on flow physics contained in Selby's research. The unswept case of the backward-facing step has been used many times to evaluate numerical methods. In the same manner, Weber [61] and Weber and Danberg [62] use their measurements of the swept, backward-facing step to evaluate the Baldwin-Lomax turbulent viscosity model and Coles' wall-wake model. Hartman [63] numerically recreated Selby's [20] experimental studies, which mainly focuses on validation, rather than new insights on the flow. Kaltenbach and Janke [64] completed direct numerical simulation (DNS) of the flow behind a backward-facing step across a range of sweep angles at $Re_h = 3000$, and large-eddy simulation (LES) of the same geometry at $Re_h = 5000$ by Kaltenbach [65]. These Reynolds numbers are quite low, but still provide some insights that would otherwise have been inaccessible. For instance, the DNS results showed a dependency of the orientation of shear layer rollers on sweep, with deviations from the freestream-normal direction of up to 25°. The LES results showed that the reattachment length was nearly independent of sweep for angles below 30°. At higher angles, the reattachment length was seen to decrease gradually. Throughout the entire sweep angle range, the flow becomes more strongly skewed with increasing sweep angle.

This review has provided an overview of topics relevant to the current research, including iced airfoil and swept-wing aerodynamics, as well as studies of ice simulation fidelity that have guided this thesis. The works reviewed represent an extensive body of knowledge, but the understanding of certain topics in aircraft icing is still incomplete. In the following section, the experimental methods employed in the current work will be described, followed by a discussion of the results.

Chapter 3

Experimental Apparatus

3.1 Wind Tunnel Facility

The testing for this study was conducted in the 3'x3' Low-Speed Wind Tunnel located at the University of Washington. The tunnel is open-return type with a 3 ft. by 3 ft. square test section that is 8 ft. in length. The test section walls, floor, and ceiling are 1 1/4" thick plexiglass for optical access. The tunnel uses an axial-type fan with a variable pitch hub, powered by a 200 H.P., constant speed, AC induction motor, which allows operation at speeds ranging from 10 ft/s to 200 ft/s. These speeds correspond to a range of Reynolds number based on step height of 2.55×10^3 to 5.11×10^4, and a range of Reynolds number per foot of 6.12×10^4 to 1.23×10^6. The inlet has a 9:1 area contraction ratio, and includes a filter media, a perforated plate, an aluminum honeycomb, and a high-porosity screen for flow conditioning [66]. Williams [67] surveyed the turbulence intensity in 2019 and found it to be 0.2% or less across the range of tunnel speeds.

3.2 Swept Flat Plate Model

A flat plate model was chosen for this experiment to avoid many aspects of the complex CRM65 geometry, while still generating key flow features and general flow physics. These aspects include the airfoil geometry and associated pressure gradients, the twist, and the taper. In this case the flow feature to be captured is the spiral vortex that occurs when the flow separates from the leading-edge ice accretion.

This type of flow is similar to that behind a backward-facing step, which served as the inspiration for the leading-edge step geometry used in this study. As seen from the descriptions in

Figure 3.1: Photograph of wind tunnel facility

Chapter 2, there are similarities between the flow behind the swept, backward-facing step and the leading-edge vortices in a Type I flow seen in the oil flow and pressure distributions.

The flat plate model tested in this study was an assembly consisting of two main parts, one upstream and one downstream, Fig. 3.2. The upstream section was the swept plate to which the leading-edge steps were mounted. The plate was constructed from aluminum and was 35.5 inches wide, leaving lateral space for foam sealing affixed with adhesive to establish a tight seal when the test section doors were closed. The leading edge of the plate has a sweep angle of 37.15 degrees, the same angle as the leading edge of the CRM65. Arranged about the centerline were 48 pressure taps. The tap holes were CNC-machined with a 1/32" diameter on the upper face and countersunk with a 1/16" diameter on the lower face. Steel tubing was inserted into the 1/16" countersunk holes to connect pressure tubing that was routed to the pressure measurement system. The arrangement of the taps was designed to span the repetition of two gap-feature pairs in the discontinuous step parallel to the leading edge. The design of the discontinuous step is discussed further in Section 3.3. A wooden splitter fence was mounted at $y/b = 16\%$ to reset the incoming boundary layer on the test section wall, as well as to reduce wall-root interactions. The wall interactions were observed with surface flow visualization to disrupt the flow enough to prevent a uniform flowfield from developing across much of the span. The addition of the fence successfully reduced these effects. The downstream section of the plate assembly was borrowed from the experimental set-up of Williams et al. [67]. The plate was machined from aluminum and included similar foam sealing on the lateral edges. Dimensions are shown in Fig. 3.2. Finally, a 12” adjustable flap consisting of a flat plate was located at the trailing-edge of the plate assembly. The flap angle was adjusted with a turnbuckle, and pre-cut template with specific angles were used for repeatability. A CAD-rendered side view with the flap angle sign convention used is shown in Fig. 3.4.

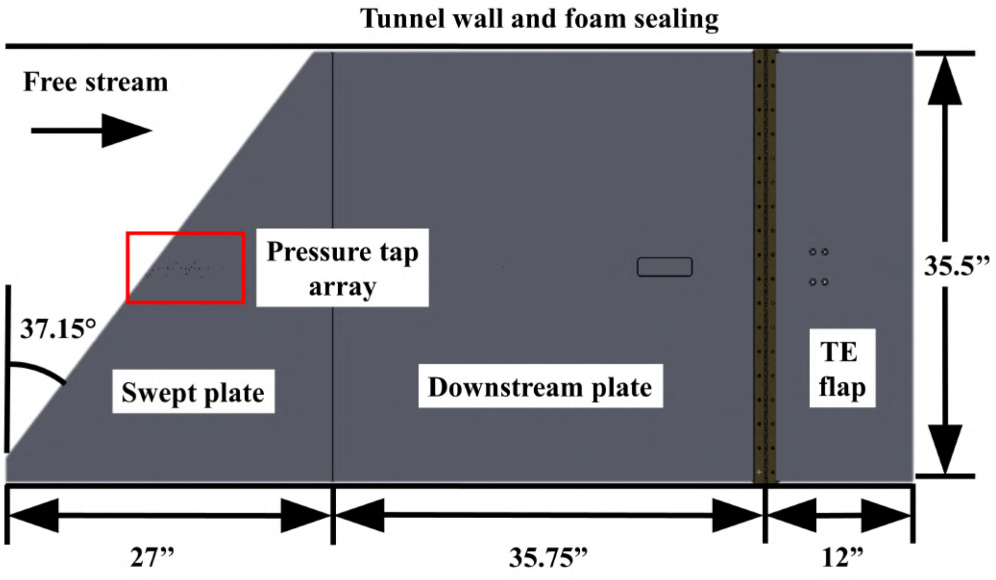

Figure 3.2: Diagram of flat plate assembly

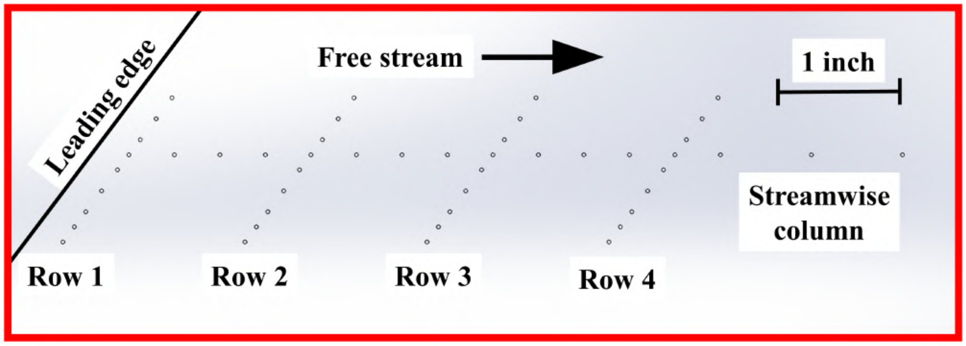

Figure 3.3: Close-up diagram of pressure tap array and nomenclature

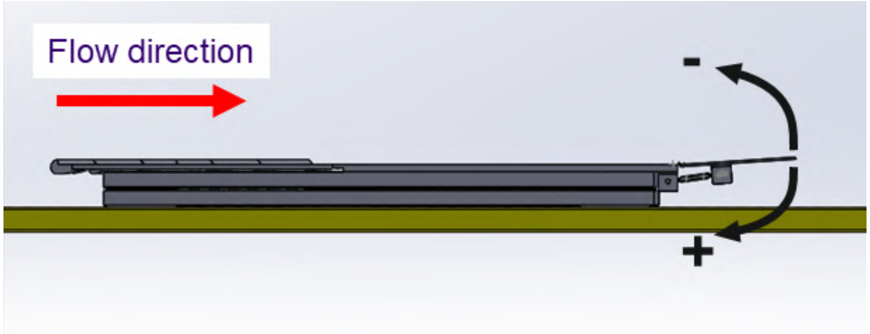

Figure 3.4: CAD render of plate assembly showing flap angle sign convention used

The flat plate assembly was mounted in the test section on a series of streamwise-oriented struts. An exploded view of the support structure is shown in Fig. 3.5 with the test section walls made invisible for clarity. The plate assembly was bolted to two pairs of stacked secondary struts. These were added to lift the plate assembly clear of the wakes of any upstream excrescences, and had reduced length so as not to protrude upstream of the leading edge. The secondary struts were stacked atop the main struts, which spanned the length of the test section and rested upon a pair of transverse rectangular bars. The spanwise bars were fitted with spring-loaded pins that fit precisely into holes in the test section inlet and outlet walls. These pins bore the full weight of the mounting infrastructure and allowed for quick installation of the struts and vertical adjustments. In the present study, the transverse bars were installed such that the upper surface of the plate was 18.75” from the test section floor, or 0.75” above the test section centerline. The upstream spanwise bar was fitted with a 3D-printed fairing in the shape of a NACA 0025 airfoil with an 8” chord length to reduce downstream wake effects that might affect the flowfield of the plate.

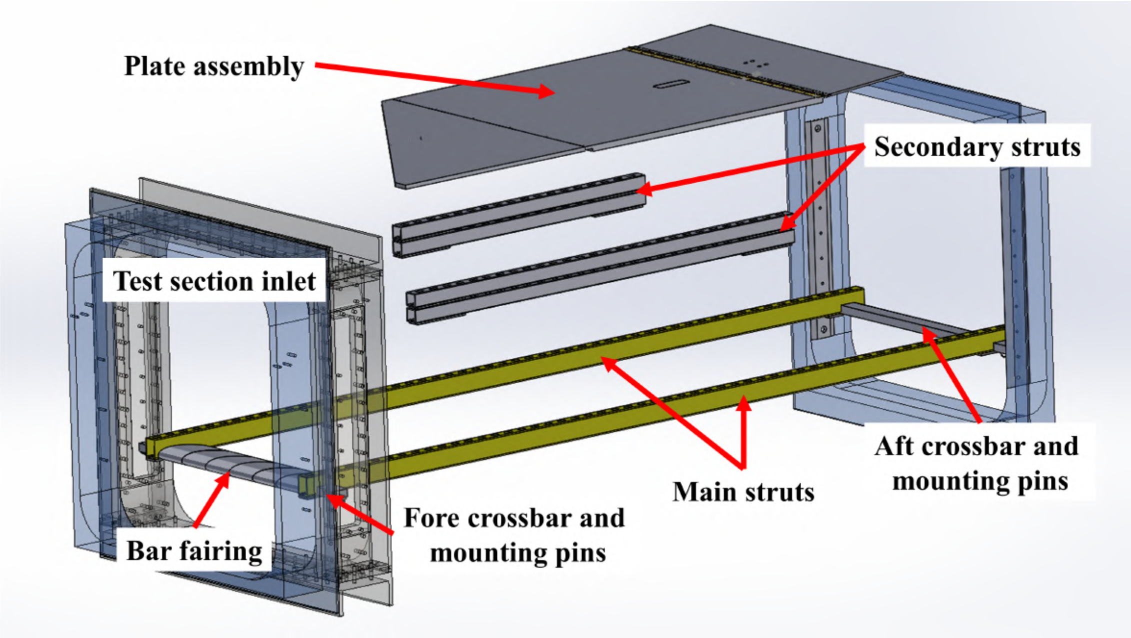

Figure 3.5: Exploded view of model installation

3.3 Leading-Edge Step Shapes

The goal behind the design of the full-span leading-edge attachments of the swept flat plate was not to test realistic ice shapes. Rather, the goal was to recreate the approximate flowfield observed in the large-scale wind tunnel testing of the CRM65 and study the effect of adding spanwise discontinuities similar to low-fidelity scallops. These flowfields are discussed in greater depth in the background given in Section 2.2. Two distinct full-span, leading-edge backward-facing step geometries were manufactured: a solid step without any gaps or features, and a discontinuous step which included low-fidelity scallop features sized after those described by Woodard et al. [22]

The intention behind the design of the solid step was to form a leading-edge vortex with a backward-facing swept step. While backward-facing steps typically have an upstream plate and boundary layer, a quarter-round leading edge shape was chosen instead. This choice avoided any substantial boundary-layer growth, similar to the leading edge of an iced airfoil. The design of the discontinuous step was derived from the Medium Gap 3-D Discontinuous artificial ice shape designed by Woodard et al. [22] As mentioned in Chapter 2, this simulated ice accretion was developed by subtracting material from the 3-D Smooth ice shape, which was created by lofting smoothed sections of the ice shapes scanned in the IRT. The gaps are streamwise-oriented at an angle of 34 degrees clockwise from the horizontal in a reference frame parallel to the leading edge. This angle was chosen to be closest to the orientation of the scallops in the high-fidelity ice shape, which was observed to not change significantly across the span of the wing. The motivation for the gap angle and reference frames is given by Woodard et al. [22]. Feature and gap widths were taken from Fig. 3.6, which plots measurements of the high-fidelity ice shape, as well as the alternative gap widths. The medium gap and feature widths, plotted in green, were used in the design of the discontinuous step in this experiment. This was done to slightly improve the comparison between the available data from those previous tests. The as-built discontinuous step is diagrammed with dimensions in Fig. 3.7.

In a reference frame parallel to the streamwise direction, the section of the step was a quarter-cylinder with a radius of 0.75”, centered at the middle of the plate’s leading-edge face. This radius and centerpoint resulted in a step height of 0.5” and an aspect ratio relative to the test section width of 72. The lower face of the quarter-round step was filleted to meet the lower step edge and give a more streamlined profile. The full-span step was 3-D printed in six sections with a Stratasys F170 printer using Stratasys ABS-M30 acrylonitrile butadiene styrene (ABS) filament. This filament was chosen for its mechanical strength and ease of post-processing. Each section was smoothed with increasingly fine grits of sandpaper to reduce striations on the leading-edge surface. The sections were bolted to the underside of the swept flat plate, with each bolt having a small rounded fairing. A CAD-rendered image shows both the steps as fixed to the plate in Fig. 3.8 and two sections of the leading-edge step are shown in Fig. 3.3.

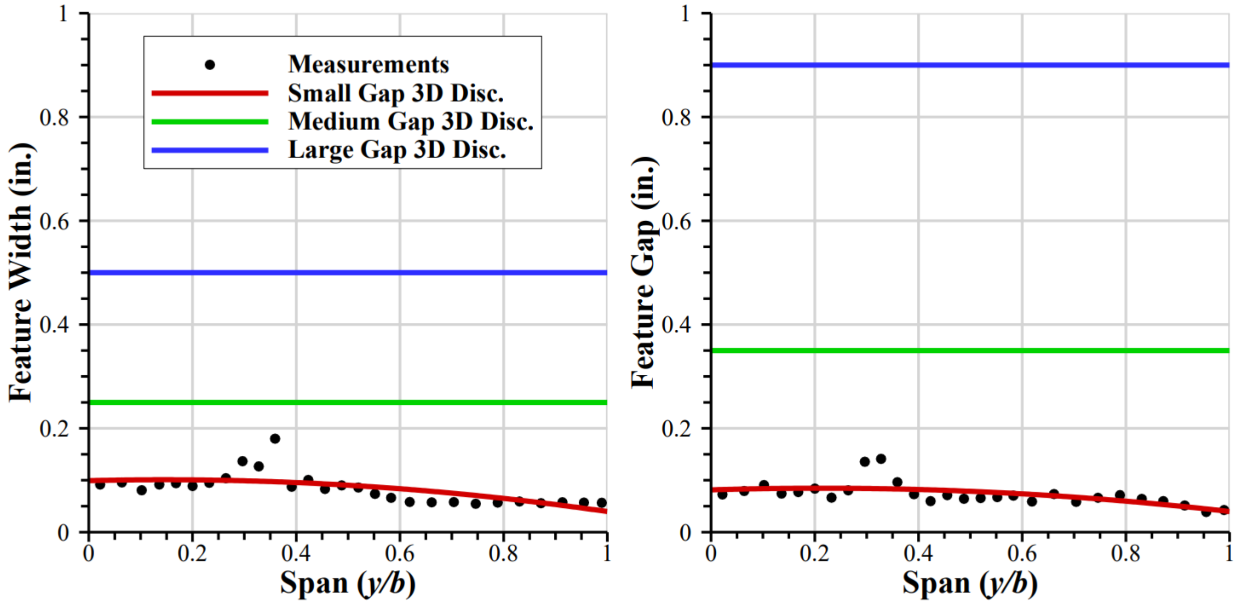

Figure 3.6: Spanwise variation of the size of the discontinuity features after Woodard et al. [22]. The feature size is scaled to the WSU model and is measured along the leading edge of the wing. Measurements from the High Fidelity ice shape are also shown for reference.

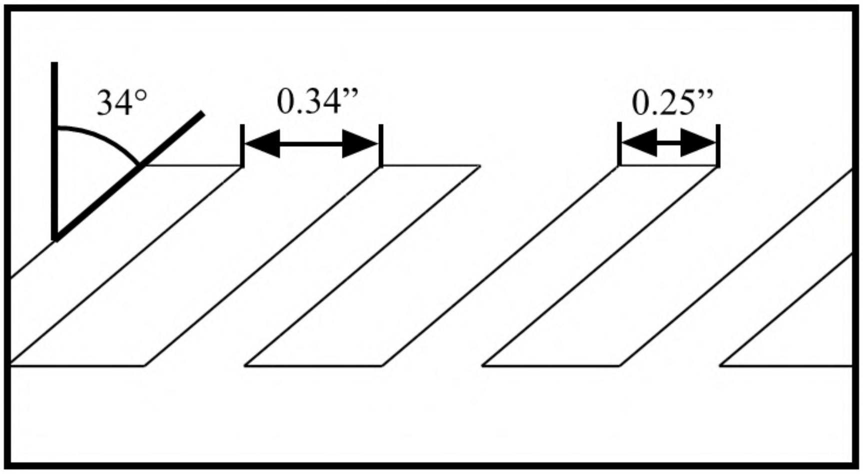

Figure 3.7: Dimensioned drawing of discontinuous step features and gaps, looking downstream parallel to the test section walls

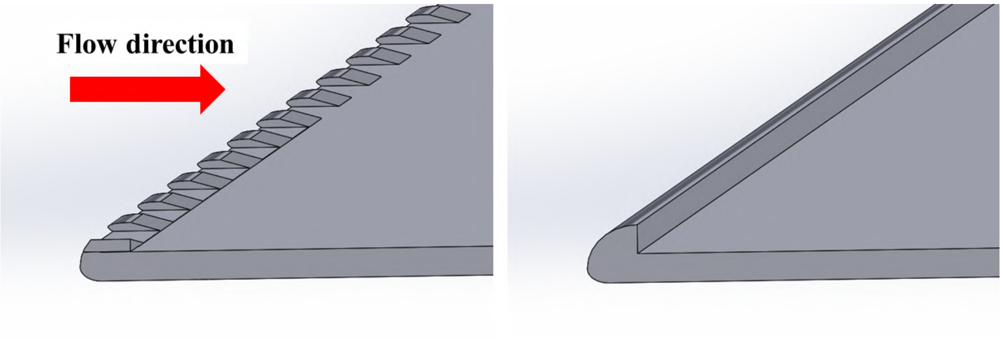

Figure 3.8: CAD rendered section cuts of the flat plate with leading-edge attachment, (left) discontinuous step, (right) solid step

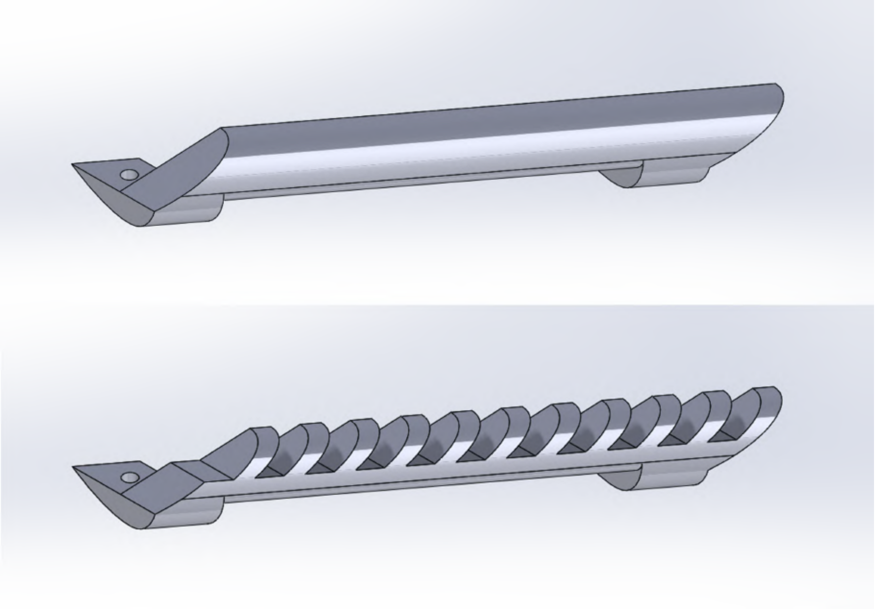

Figure 3.9: CAD renders of the 3-D printed leading-edge step sections; (Top) solid, (bottom) discontinuous

In all, five total step configurations were tested. The first and second were the solid and discontinuous steps, which were the primary configurations. Rather than manufacture additional 3-D printed leading-edge steps, the other three configurations were temporary modifications of the first two. Similar to previous studies of ice shape fidelity, a coating of grit serves as a slight increase in fidelity, as it mimics realistic ice roughness. In the present study, a protective layer of tape was applied to the surface of each section of the solid leading-edge step, followed by a thin coating of glue, and then 24 grit. As the glue hardened, the grit particles were securely fixed to the leading

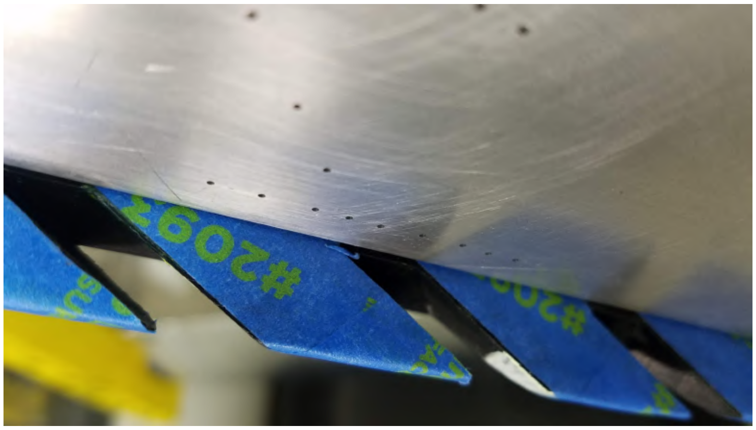

Figure 3.10: Photograph of the alternating-gap discontinuous step and the pressure tap array

edge, but could be easily removed by pulling the tape off of the step. As a note, 24 grit has a mean size of 0.0270”. Typically, grit is scaled to the ice shape based on the ratio of roughness height to chord, k/c, however, in this case, the largest grit available was used in an attempt to produce the most visible results.

The final two step configurations were modifications using the discontinuous step. In one, the center section from the discontinuous step was installed alongside the remaining four solid step section. This configuration has no basis for comparison in the existing literature, but proved to be interesting. In the last configuration, tape was used to completely block every second gap, Fig. 3.10. This was completed as a replacement for manufacturing a leading-edge step with a different gap width, similar to Woodard et al. [22], who designed several variations on the gap size of the 3-D Discontinuous artificial ice shapes.

3.4 Data Acquisition

Data acquisition was controlled on a desktop computer in the wind tunnel facility. LabView 2019 was used as the software interface, which displayed tunnel speed, temperature, and which pressure tap was being measured. Plate surface pressures were measured using a Honeywell 143PC01D differential pressure sensor with a range of ± 1 psid and an accuracy of 0.3% full scale. This sensor was powered by an Elenco Precision Quad Linear regulated supply. The sensor was referenced against the tunnel inlet static pressure, and a Scanivalve solenoid valve was used to cycle through the 48 pressure taps. The LabView code was used to send voltages to advance and home the solenoid valve. A 10-second dwell time with samples taken at 1000 Hz was recorded and averaged for each pressure tap measurement. Tunnel temperature was measured with a K-type thermocouple. Analog signals were digitized with a National Instruments model NI-9205 analog input module and a model NI-9213 thermocouple module, which included 16-bit analog-digital converters.

Initially, velocity above the plate was measured using a pitot-static probe and an Omega PX653-10D5V differential pressure transducer, which has a range of 0 to 10 inH_20 and an accuracy of 0.05%. Due to constraints in test section access, the pitot-static probe needed to be placed downstream of the step. It was noticed during preparations that at higher tunnel speeds, issues arose with the pitot-static measurement, potentially due to vortex shedding from the separated flow behind the step. In response, the dynamic pressure at the test section entrance was calibrated to the velocity above the plate with the solid step installed. This was completed using measurements from the pitot-static probe, kerosene manometer, and the readout from the LabView interface. The calibrated velocities obtained from the test section entrance dynamic pressure were used for all runs discussed in this paper. As a note, large differences in dynamic pressure were not expected between the tunnel inlet and above the plate assembly. The primary driver in these tests was not the exact tunnel velocity, and instead was the variation in the flowfield structures with changing geometry.

The effect of flap deflection on flow angularity ahead of the leading edge of the plate was quantified using an Aeroprobe standard, straight five-hole probe. The probe was affixed to the lower surface of the plate at four spanwise stations, and was positioned such that the probe tip was four step heights, or 2” ahead of the leading edge in the streamwise direction. This upstream position was chosen to acquire measurements that were suitably away from the local flowfield about the leading edge, while maintaining enough probe length in contact with the plate to be securely mounted. Pressure tubing was plumbed from the five taps to the first five ports in the

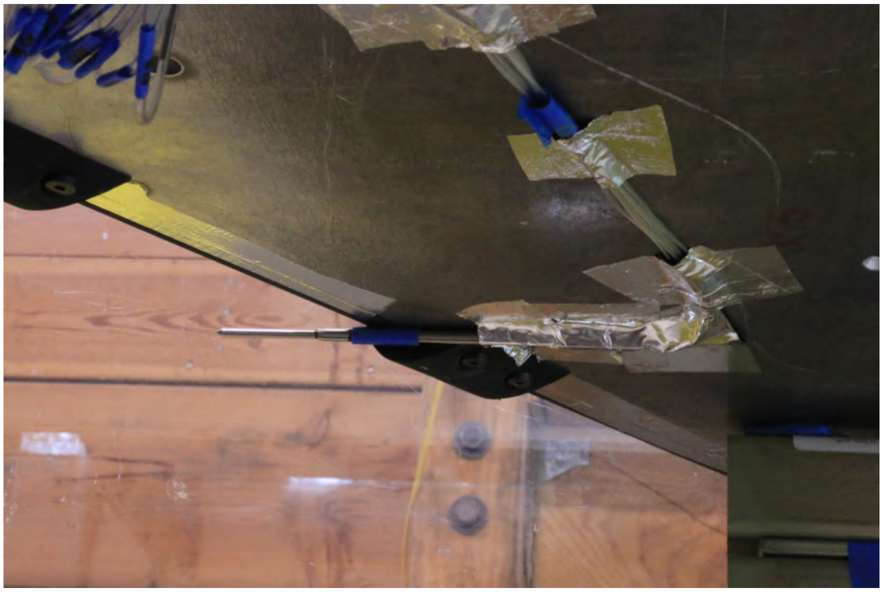

Figure 3.11: Photograph of five-hole probe mounted on the underside of the plate

Scanivalve, and data were collected using the LabView interface as with the surface pressure tap array. The pressure probe data were reduced using Matlab codes previously developed for the wake survey of the CRM65 model, which is described by Lum [40] and Diebold [68].

3.5 Fluorescent-Oil Surface Flow Visualization

In order to acquire a qualitative picture of the flowfield through the mean flow, fluorescent surface oil flow visualization was used. The methods employed were similar to those used in the wind tunnel testing of the CRM65 model, as described by Woodard et al. [39] and by Diebold [68]. The operating principle of the technique is that areas with high shear will have the oil removed, and oil will flow in the direction of the mean surface shear stress.

The first step was to apply matte black, self-adhesive vinyl sheets made by Con-Tact brand. The purpose of this was to safeguard the pressure taps against oil blockage and provide a non-reflective background that contrasts with the color of the fluorescent oil. Next, a small amount of 10W-30 motor oil is spread over the surface of the sheet, making sure to wipe away excess oil. This step is intended to fill any small imperfections in the vinyl sheet and provide a thin layer of oil over which the fluorescent oil may easily flow.

The fluorescent oil mixture consists of a small proportion of fluorescent leak-detection dye combined with heavy-viscosity mineral oil. The dye used was Tracerline TP-3400 Dye-Lite, which fluoresces yellow-green with exposure to UV light. The fluorescent oil was applied in two ways throughout this test. The first way used a small paint roller with the fluorescent oil applied. A uniform layer of the oil mixture was rolled onto the plate, and the tunnel was run for 3 to 5 minutes, depending on the Reynolds number. The oil was re-rolled until a uniform coating was again reached to reset the after a run. The second method employed a disposable acid brush. The end of the brush was dipped in the tray of oil mixture and lightly tapped on the prepared surface of the vinyl covering, which left small, discrete droplets. These droplets left traces as they were pushed by shear forces, which helped show the presence of flow structures invisible with the oil film method. Before running again, this second method required that all of the oil be wiped away, and the vinyl sheet be cleaned with window cleaner before applying another layer of motor oil and dye mixture.

In either method of application, after the desired wind-on time, the tunnel was turned off and allowed to spin down. Once the test section had settled, the door was opened, and a UV lamp was positioned in the test section, making an effort to minimize glare and reflection while brightly illuminating the entire area of interest. Photos were taken through a polished section of the test section ceiling using a Nikon D3200 DSLR camera, equipped with a Nikon AF-S DX Zoom-Nikkor 18-55mm f/3.5-5.6G lens. The camera was positioned carefully to capture the full extent of the swept flat plate, while avoiding any kind of angling which might distort the resulting photographs. This was accomplished using a Manfrotto camera tripod which allowed the camera to point straight downward while removing the tripod legs from the frame.

Using images of the fluorescent-oil surface flow visualization, the streamwise reattachment length behind each solid step configuration could be quantified. The measurement process was completed using the grabit Matlab image processing tool, which is openly available on the MathWorks File Exchange. First, an oil flow image was uploaded and input into the grabit function. Next, the axes were set using distances that were known between landmarks observable in each photo. Then, two points along the leading edge were selected. A linear function representing the location of the leading edge was determined using these points. Finally, the coordinates of points along the mean reattachment line visible in the surface oil flow were recorded across the span. The streamwise reattachment length was computed as the difference between the leading edge linear function and the reattachment line coordinates. These differences were then averaged across the span for the solid step, both with and without 24 grit applied. A sample oil flow image of the flow behind the solid step is given in Fig. 4.4 to help illustrate the streamwise reattachment length and the distinguishing characteristics of the leading-edge vortex.

Chapter 4

Results and Discussion

This chapter presents the results of applying the experimental techniques and steps described in Chapter 3. The chapter is divided into sections by the effects of changing key variables in the experimental setup. The presentation and discussion of results begins with the effects of trailing-edge flap deflection, which are shown using five-hole pressure probe measurements along the span, surface pressure measurements, and the assessment of fluorescent-oil surface flow visualization. Beginning with a presentation of the general effect of the trailing-edge flap provides the proper background to discuss the effects of the addition of spanwise discontinuities to the backward-facing, leading-edge step. Improving the understanding of the discontinuous step geometry is a primary motivation for this thesis. As such, a detailed analysis of the resulting flowfield will be made. Next, the flowfields of the solid step configurations are compared with and without a coating 24 grit. The final section covers the trends observed when varying Reynolds number and Mach number.

4.1 Trailing-Edge Flap Deflection Effects

Several of the key findings of this thesis depend upon the variation of the trailing-edge flap angle. For example, certain types of flowfields behind the step are only observed within certain ranges of flap angle. Thus, it is necessary first to describe the effect that the flap had on the flat plate flowfield. As will be seen, the flap angle imposes significant changes upon the flow about the leading-edge, backward-facing step. Initially described in Section 3.2, the flap consists of a flat plate deflected up or down by adjusting a turnbuckle between the flap and aft flat plate. In this experiment, the flap angle was set to four angles: -10°, -5°, 0°, and $+4^\circ$. The

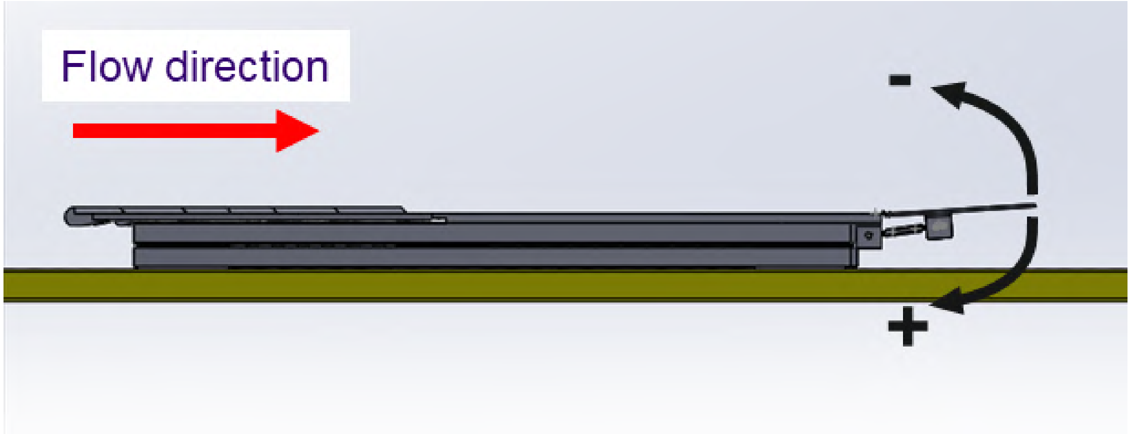

Figure 4.1: Diagram of the flap plate assembly showing the flap angle sign convention

only downward deflection angle, +4°, was limited by the maximum downward angle allowed by the turnbuckle. The baseline configuration was a flap deflection of -10° and a wind speed of 60 m/s. This configuration will be a point of reference at several points throughout this chapter. The following subsections show the effect of flap angle, first using five-hole probe measurements ahead of the leading edge, and then with observations of the flowfield made with fluorescent-oil flow visualization and surface pressures. For reference, the sign convention of the flap angle is diagrammed onto a CAD rendering of the plate assembly in Fig. 4.1.

4.1.1 Flow Angularity Upstream of Leading Edge

Surface oil flow visualization was used to qualitatively see the effects of the trailing-edge flap angle. A five-hole pressure probe was then used to compute the local flow angularity about the leading edge. The trailing edge flap altered the circulation about the flat plate assembly, which, in turn, altered the stagnation point and local flow angles. Unfortunately, no pressure taps were installed along the leading-edge surface to quantify the location of the stagnation point. As a result, the primary quantitative measures of the effect of flap setting in the present study were the five-hole probe data. Measurements were taken for both the discontinuous and solid backward-facing step configurations at four spanwise stations and at each flap angle. The results are plotted in Figs. 4.2, and 4.3.

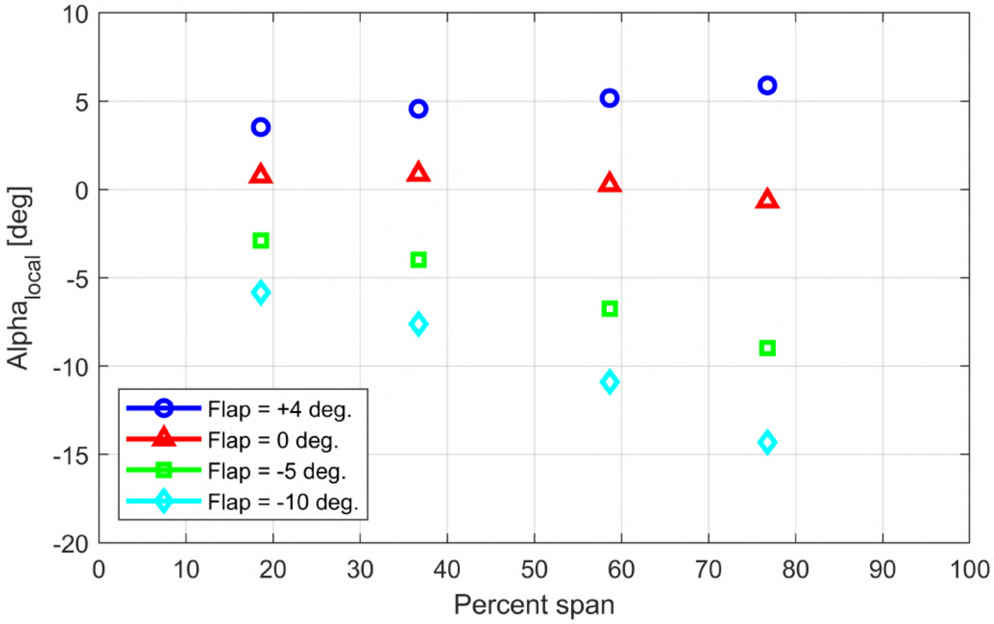

Figure 4.2: Local flow inclination angle 4h upstream of leading edge and level with plate underside; solid step at 60 m/s

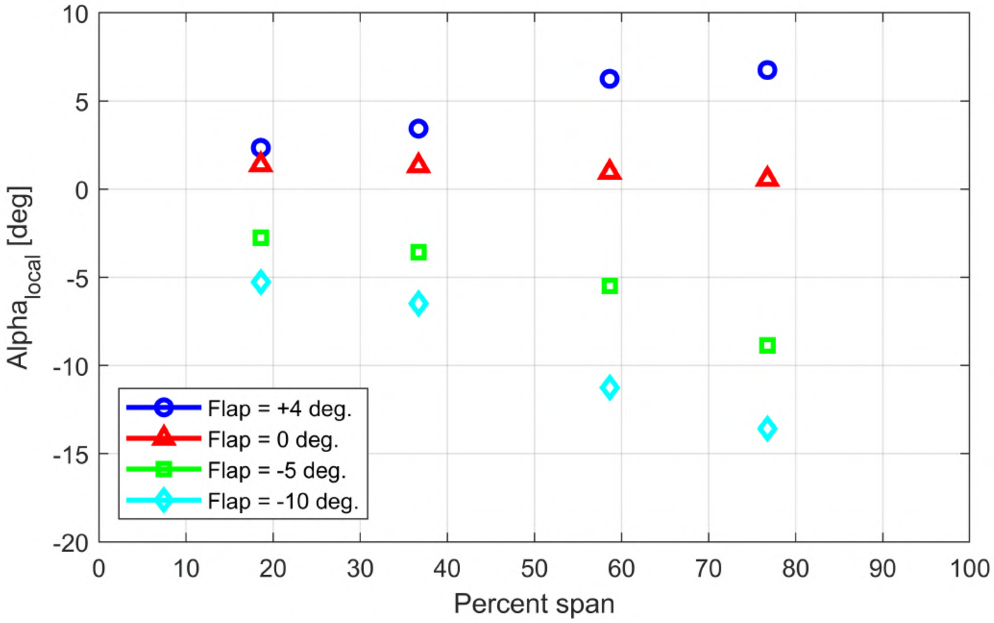

Figure 4.3: Local flow inclination angle 4h upstream of leading edge and level with plate underside; discontinuous step at 60 m/s

As expected, as the flap is angled downward, the inclination of the local flow ahead of the leading edge of the plate trends upward. The change suggests that the stagnation point of the flow has shifted lower on the leading-edge surface, which is expected for a lifting body with higher circulation. A critical insight from these data is the spanwise variation of the flow angle, α_{local}. At negative flap deflections, this angle becomes significantly more negative along the span in the outboard direction. At a positive flap setting, the trend reverses and α_{local} instead becomes slightly more positive or upwardly inclined in the outboard stations. These trends do not appear to differ significantly between the two step geometries tested. The results that follow in this section show the ways in which the spanwise variation of flow angularity affects the flowfield behind the step configurations.

It is important to state that the flow angles computed across the span using the five-hole probe should not be interpreted as the effective angle of attack, as with an airfoil. Rather, the α_{local} of the flow at each spanwise location should serve as a more general indicator of trends of flow angle as a function of the spanwise position and flap deflection. After reviewing the results, it was determined that placing the probe tip four step heights ahead of the leading edge was insufficient to avoid the influence of the local flow about the step. As a result, the computed flow reaches angles that are quite large, Fig. 4.2-4.3.

4.1.2 Flow Separation

The preceding section analyzed the quantitative effect that flap deflection had upon the local flow angularity upstream of the leading edge of the plate. As will be seen, the changes in incoming flow angle and stagnation point location are strongly connected to the overall flow behind the step. Specifically, the presence and development of a leading-edge flow separation region in various configurations. First, the results for the solid step will be reviewed. The solid step, due to its sharp corner, features flow separation regardless of the flap setting. Despite this, noticeable changes occur throughout the deflection range, as observed in the pressure distributions and streamwise reattachment lengths. The discontinuous step will be analyzed second. This step geometry experiences the most dramatic changes due to the shifting stagnation point and the onset of leading-edge separation. The flowfields of this step vary from a uniform and relatively attached

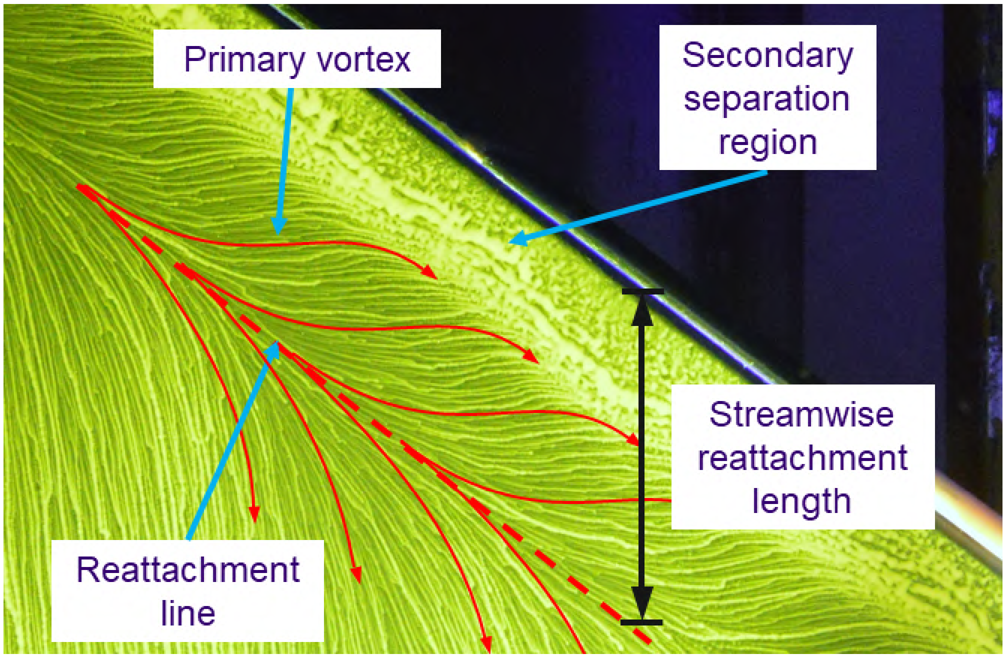

Figure 4.4: Sample oil flow visualization image showing vortex reattachment length behind the solid step at 60 m/s

Type II-dominated flowfield, to showing signs of significant regions of flow separation.

Solid Leading-Edge Step

The solid leading-edge step shape was characterized by the separation of flow at the sharp corner. By design, the solid step consistently had a clear leading-edge spiral vortex, the reattachment length of which could be determined for comparison between geometries and configurations. Fig. 4.4 outlines the anatomy of the separated region and how they appeared in the surface oil flow visualization. The intent of the solid step was to recreate a Type I flowfield. The streamwise reattachment length was measured digitally using surface oil flow images and the grabit Matlab image processing tool, as described in Chapter 3.

The resulting measurements of mean reattachment length at each flap angle are plotted in Fig. 4.5. This plot shows a generally positive relationship between flap angle and mean reattachment length at an airspeed of 60 m/s. As the flap angle increases, the stagnation point shifts lower on the surface of the leading edge. The flow must then rapidly accelerate around the leading edge,

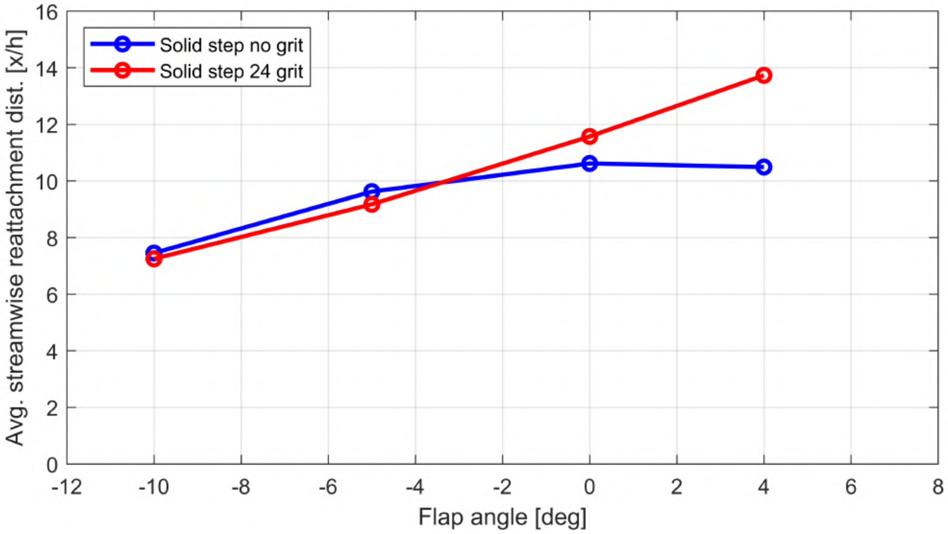

Figure 4.5: Variation in mean streamwise reattachment length at 60 m/s with flap angle, as measured from oil flow visualization images

and encounters strong suction followed by an adverse pressure gradient. At this point, the flow is more likely to separate even before encountering the sharp step corner. Unfortunately, no pressure taps were located along the leading edge to gain quantitative evidence of the changes in the leading-edge pressure distribution. In the case that the flow separates before reaching the corner of the backward-facing step, the separated flow is likely to have an upward velocity component. Upward velocity would slow the reattachment of the flow by requiring a longer distance to respond to the sharp expansion. This is in contrast to the standard backward-facing step geometry, which would simply have an incoming boundary layer with streamlines parallel to the upstream flat plate.

In Selby's [20] comprehensive study of swept, backward-facing steps, a step with $\Lambda = 30^\circ$ and $h = 0.50$" produced reattachment lengths at the centerline of roughly $6h$. As first described in Section 2.3.3, these swept steps included an upstream extent of flat plate, over which the boundary layer could develop. This type of swept, backward-facing step is referred to as a "standard" swept step, as it is representative of the type of geometry used in nearly all backward-facing step studies. The standard step is in contrast with the leading-edge backward-facing steps that are subject of the present study, which have a rounded leading edge, rather than an upstream flat plate. These data were acquired at $Re_h = 5.36 \times 10^3$; however, Section 4.4 will present evidence that separated flows

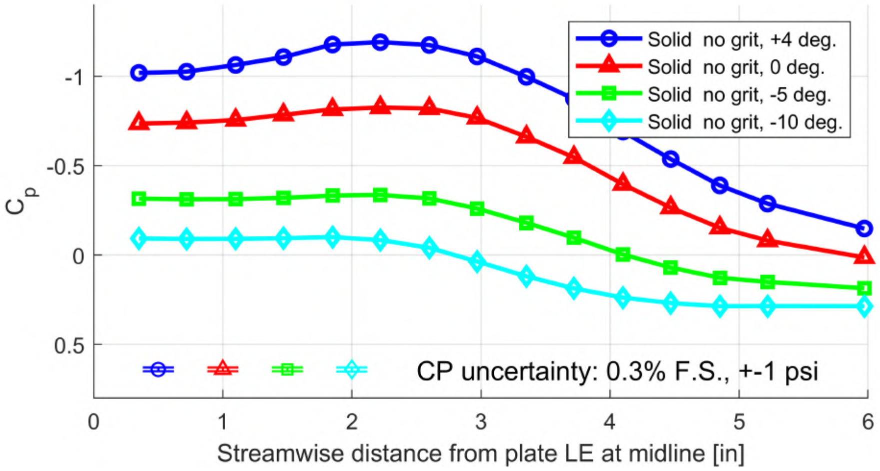

Figure 4.6: Pressure distribution along the streamwise tap row for the solid step at each flap angle and 60 m/s

like the backward-facing step may be independent of Reynolds number in the turbulent regime. Comparing this reattachment length to that of the solid leading-edge step, which was 7h or greater, the standard swept backward-facing step indeed has shorter reattachment lengths. Despite the fact that both solid step configurations are plotted in Fig. 4.6, a full discussion of the effect of adding 24 grit to the surface of the solid step will be delayed until Section 4.3.

The streamwise distribution of surface pressures may also give insight into the separated region of the flow behind the solid backward-facing step. The distributions are plotted at each flap angle and an airspeed of 60 m/s in Fig. 4.6. The location of the core of the spanwise-running leading-edge vortex is may be suggested by the low-pressure peak seen between 2 and 3 inches. Similar flowfields and pressure distributions were observed by Tanner [23] during experimentation on a two-dimensional wedge shape, Fig. 4.7. The spanwise-running spiral vortex is seen as S-shaped traces in the surface oil flow visualization. Pressure recovery and reattachment occur as the pressure converges toward the freestream value. Unfortunately, the streamwise extent of the pressure tap distribution was not sufficient to capture the complete recovery. Nonetheless, the pressure recoveries plotted in Fig. 4.6 confirm the increase in reattachment length, which was digitally measured using the flow visualization images. As the flap angle increases, the pressure recovery is seen to be at varying stages of progress at the final pressure tap depending on the

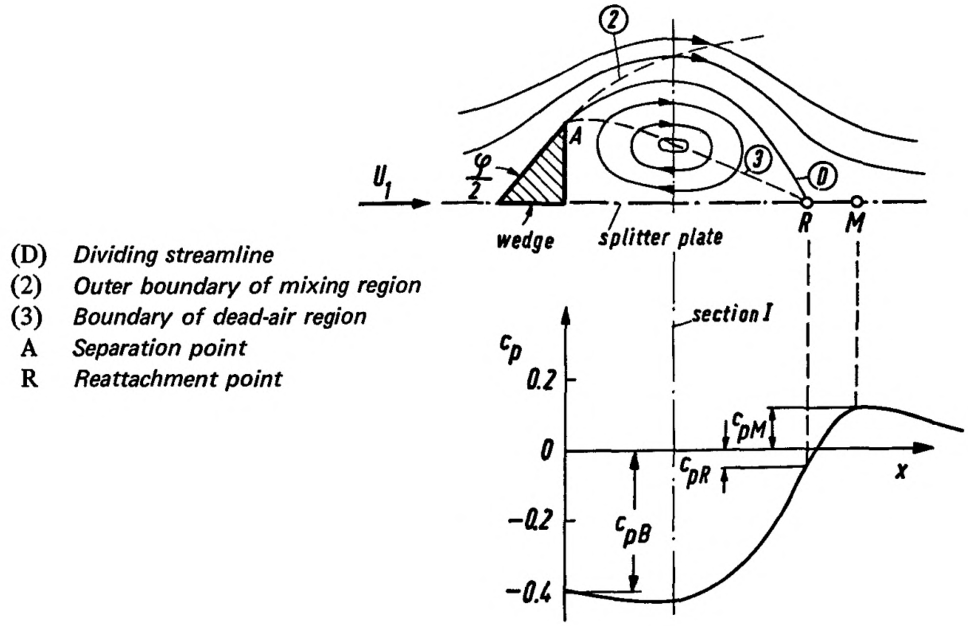

Figure 4.7: Diagram of steady flow past a two-dimensional wedge, after Tanner [23]

flap angle. Higher flap angles appear to lead to recovery occurring further downstream from the step face. As a note, when comparing the streamwise pressures to the mean reattachment length measured from oil flow photos, it is important to remember that the reattachment length trends are averaged across the entire span. In contrast, there is only a pressure tap row at a single spanwise station.

Figs. 4.8 to 4.10 show oil flow visualization images for the solid backward-facing step alongside selected configurations of the CRM65. For reference, both the Reynolds number based on step height and Reynolds number based on MAC of the CRM65 are shown, though it is difficult to compare the two. Overall, the red line overlaid on the photographs show that the separation region behind the solid step covers a longer streamwise distance as the flap deflection is increased. Next to the images of the step flowfields are fluorescent-oil surface flow visualization photographs of the Maximum Scallop 3-D Smooth ice shape as tested on the 8.9% scale CRM65 wing model at increasing angles of attack. First, it must be noted that the comparison between the solid step and the Maximum Scallop 3-D Smooth shape is merely to illustrate the Type I flowfields that evolve downstream of each geometry. It must not be discounted that the cross-section of the Maximum

Scallop 3-D Smooth varies along the span, while that of the solid leading-edge step does not. Additionally, the comparison of the backward-facing, leading-edge step flow and the Maximum Scallop 3-D Smooth ice shape is not intended to suggest any equivalency of angle of attack of the CRM65 and flap angle of the flat plate assembly. This comparison is merely intended to show parallels between two Type I flowfields and their evolution as local flow angularity changes.

Figs. 4.8 to 4.10 show that for both the flat plate with leading-edge step and the CRM65 with the Maximum Scallop 3-D Smooth ice shape, the flow separates and forms a spanwise-running spiral vortex. As the incoming flow angle is increased, the separation regions grow, leading to reattachment occurring further downstream. The growth also varies along the span of each model. For instance, at flat plate flap angle of -10° and CRM65 $\alpha = 4^\circ$, the mean vortex reattachment line is roughly constant across the span, Fig. 4.8. Increasing to a flat plate flap angle of $+4^\circ$ and CRM65 $\alpha = 6^\circ$, reattachment length in both models now increases across the span, with the primary vortex being shed completely in both cases, Fig. 4.10. The general flowfield patterns and evolution confirm that the desired Type I flowfield is formed by behind the backward-facing, leading-edge step. In the next section, the effect of flap deflection on the overall flowfields of the

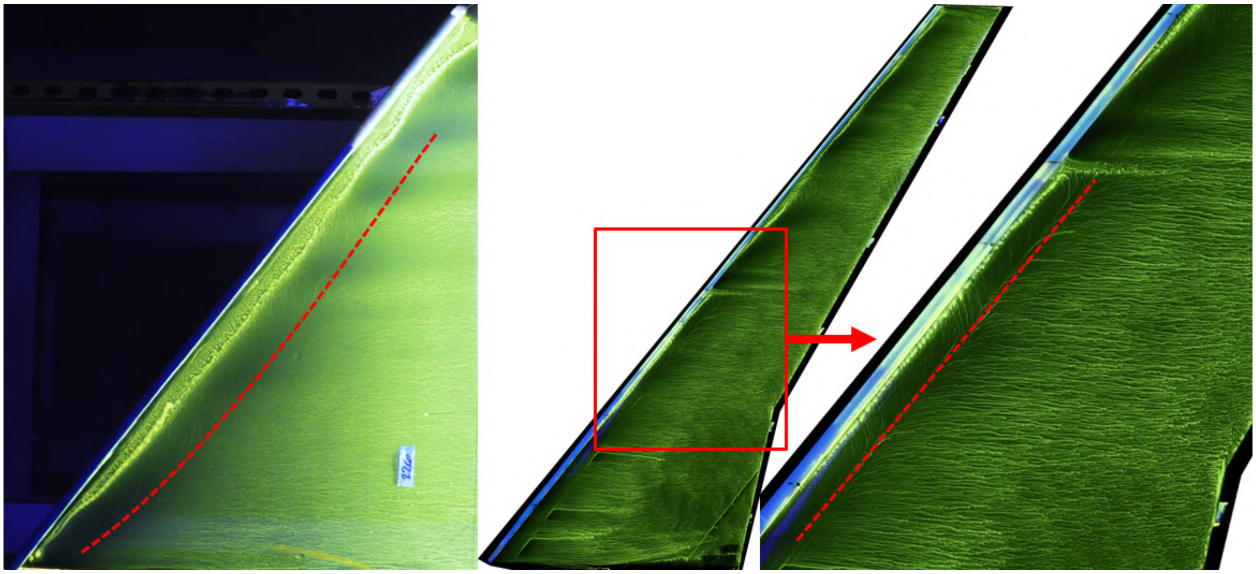

Figure 4.8: Comparison of swept flat plate and CRM65 oil flow visualization with vortex reattachment indicated by dashed line; (left) solid step, flap angle of -10°, $Re_h = 5.03 \times 10^4$, (right) Maximum Scallop 3-D Smooth, $\alpha = 4^\circ$, $Re = 1.6 \times 10^6$

discontinuous step configurations will be analyzed.

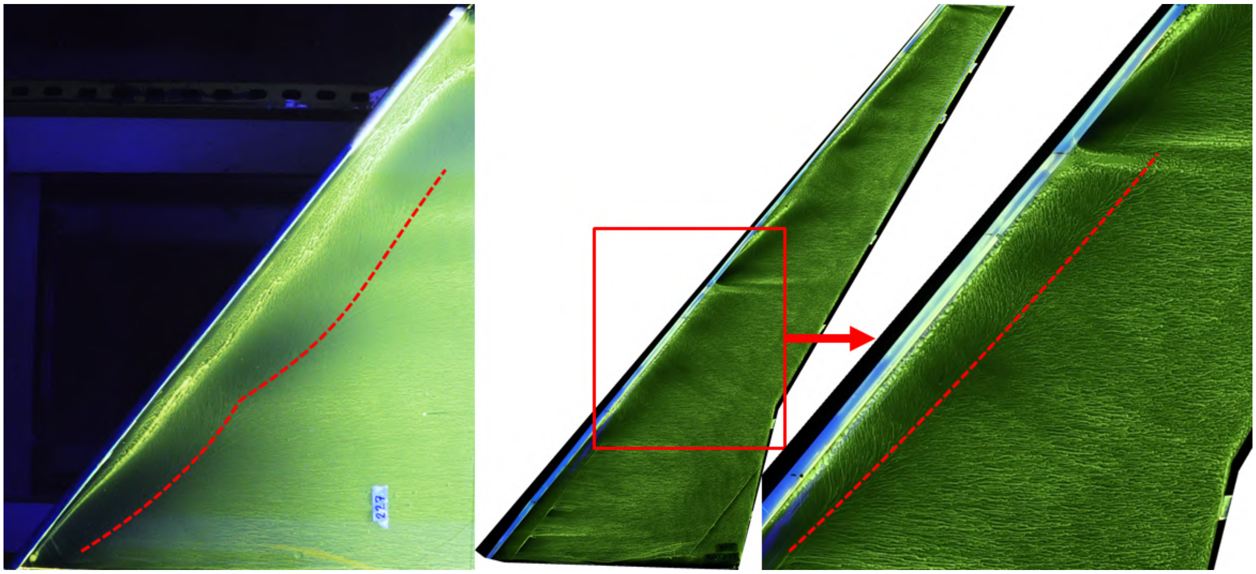

Figure 4.9: Comparison of swept flat plate and CRM65 oil flow visualization with vortex reattachment indicated by dashed line; (left) solid step, flap angle of $-5°$, $Re_h = 5.03 \times 10^4$, (right) Maximum Scallop 3-D Smooth, $\alpha = 5°$, $Re = 1.6 \times 10^6$

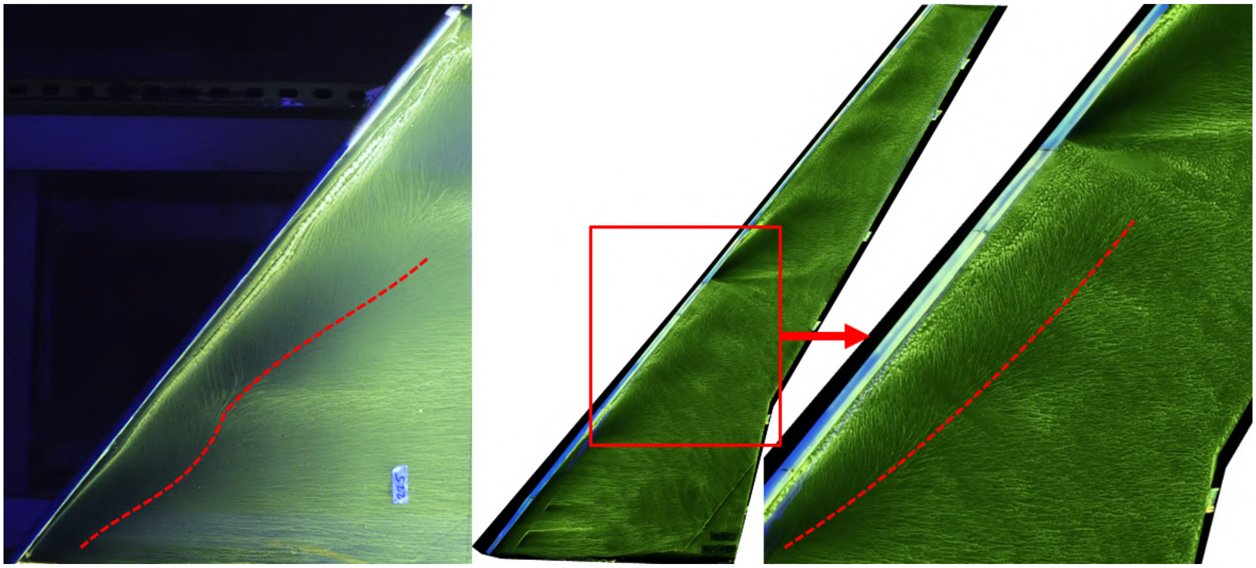

Figure 4.10: Comparison of swept flat plate and CRM65 oil flow visualization with vortex reattachment indicated by dashed line; (left) solid step, flap angle of $+4°$, $Re_h = 5.03 \times 10^4$, (right) Maximum Scallop 3-D Smooth, $\alpha = 6°$, $Re = 1.6 \times 10^6$

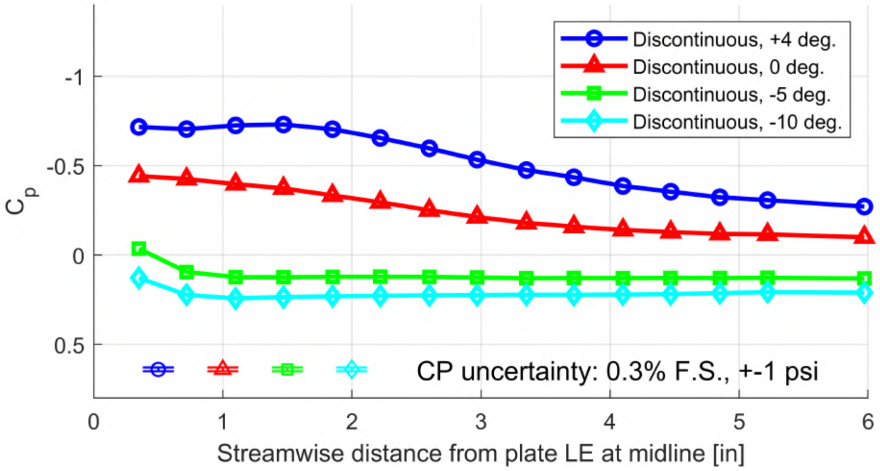

Figure 4.11: Pressure distribution along the streamwise tap row for the discontinuous step at each flap angle and 60 m/s

Discontinuous Leading-Edge Step

Unlike the solid step configurations, the discontinuous steps did not have a clear separation and reattachment visible in the surface oil flow visualization images. The most striking features of the flowfields are the Type II streamwise streaks, which are most apparent at the baseline flap deflection. In this configuration, evidence of the characteristic leading-edge vortex of the solid step has been eliminated. However, dramatic changes in the flowfields associated with this geometry and its variants were observed across the range of flap angles. As the stagnation point shifted lower due to downward flap deflection, signs that the flow separated before passing through the spanwise discontinuities were observed. One such indications was the presence of oil collecting in between gaps. The streamwise pressure distributions plotted in Fig. 4.11 also suggest flow separation at flap angles of 0° and +4°. The distributions of these configurations resemble those of the solid step, plotted in Fig. 4.6, which has confirmed separated flow.

Like the comparison made for the solid step, Figs. 4.12 to 4.14 show the flowfield evolution of the discontinuous step configurations as flap angle increases. Each image of the flat plate surface flow visualization is now compared with oil flow images from the Medium Gap 3-D Discontinuous shape at different angles of attack. It was the Medium Gap 3-D Discontinuous ice shape that the discontinuous step geometry was derived from, using the same gap and feature widths, along with the same cutting plane angles. With a flat plate flap angle of -10° and CRM65 $\alpha = 4^\circ$, streamwise streaks dominate the flowfields of both configurations, Fig. 4.12. Increasing to a flap angle of -5° and CRM65 $\alpha = 6^\circ$, the oil flow visualization reveals a complex distribution of streamwise features of varying width and spacing, quite unlike the uniform distribution seen previously. Judging by the streamwise pressure distribution at the plate centerline, it cannot be said with certainty that the flow is completely separated. However, the higher flow angle has drastically affected how the flow passes through the discontinuities. Section 4.1, which reviewed five-hole probe measurements at each flap deflection, showed that at certain flap angles, flow angle had significant spanwise variation, Fig. 4.3. Specifically, at negative flap angles, the flow angle decreased in the outboard direction. The spanwise distribution of flow inclination helps to explain some of the spanwise variation on the flat plate. It may be that the local flow in the outboard region approaches at a low enough angle to avoid separation and facilitate flow through each gap. As a result, this makes the visualization in that specific region resemble that of the -10° flap angle configuration. In contrast, the local flow inclination within the inboard region has seemingly passed a critical angle at which the discontinuities are no longer having the same individual effects seen in the oil flow.

Finally, at a flat plate flap angle of $+4^\circ$ and CRM65 $\alpha = 8^\circ$, there are signs that a separation region has formed upstream of the discontinuities, Fig. 4.14. A close-up view of the oil flow visualization at this configuration is also shown in Fig. 4.15. This image shows the bifurcation of oil flow lines along the reattachment point, similar to the flowfield associated with the solid backward-facing step. An important distinction in the case of the discontinuous step at a flap angle of $+4^\circ$ is that the spiral flow lines within the separated region are now deformed by light and dark streamwise-running region. This observation will be discussed further during the in-depth analysis of the effect of spanwise discontinuities in the backward-facing step in Section 4.2. The separation region is also seen in the pressure distribution for this configuration, Fig. 4.11, which shows a low-pressure plateau highly similar to the separation region measured behind configurations of the solid step. In addition, oil flow visualization shows a drastic reduction of the uniform Type II streamwise features observed at negative flap angles. It must be acknowledged that some streamwise streaks are visible in the oil flow on the flat plate, but the full discussion of this is deferred to Section 4.2.

In summary, the flow angularity changes which vary across the span of the plate, suggest that flap deflection shifts the stagnation point and significantly alters the flow about the leading edge. For the solid step, this results in the growth of the Type I leading-edge vortex. This trend is similar in some ways to a Type I flowfield like that of the Maximum Scallop 3-D Smooth. At a negative flap setting, the gaps in the discontinuous step are seen to greatly disrupt the spanwise vortex, as seen in the oil flow visualization and pressure distributions. In this case, rather than a spanwise-running spiral vortex, the flow is dominated by Type II streamwise streaks across the entire span. However, as the flap angle is increased, the flowfields behind the step configurations show signs of separation and large, irregular streamwise-running streaks. In the following section, the results for the three discontinuous step variations are analyzed to probe the flow structures that make up the Type II flowfield.

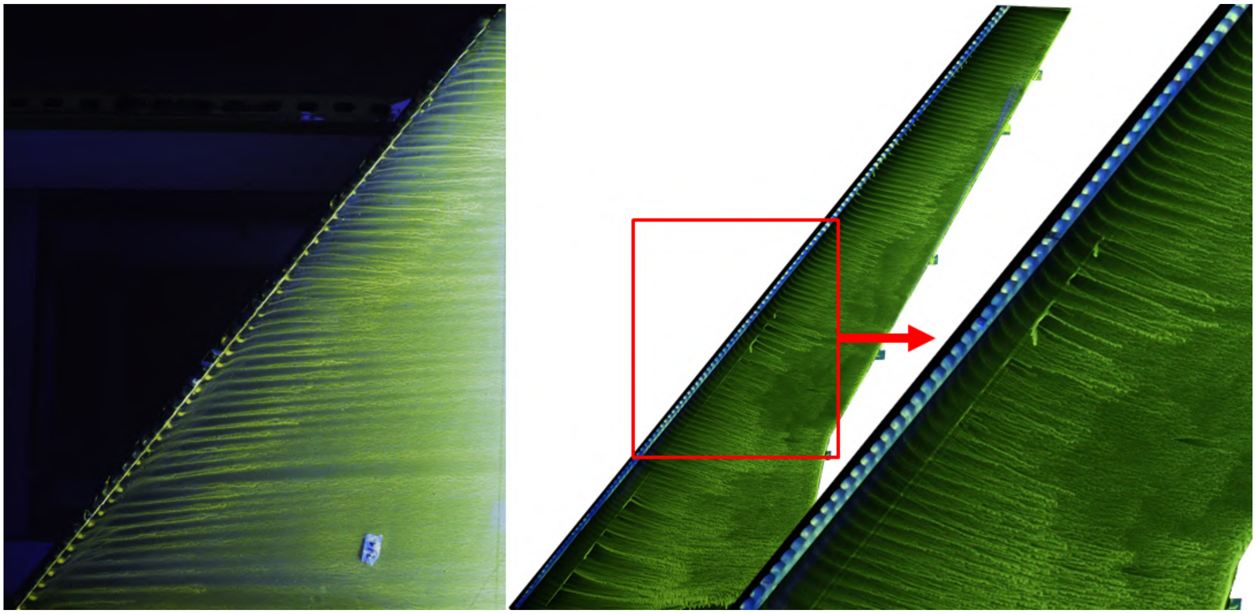

Figure 4.12: Comparison of swept flat plate and CRM65 oil flow visualization; (left) discontinuous step, flap angle of $-10°$, $Re_h = 5.03 \times 10^4$, (right) Medium Gap 3-D Discontinuous, $\alpha = 4°$, $Re = 1.6 \times 10^6$

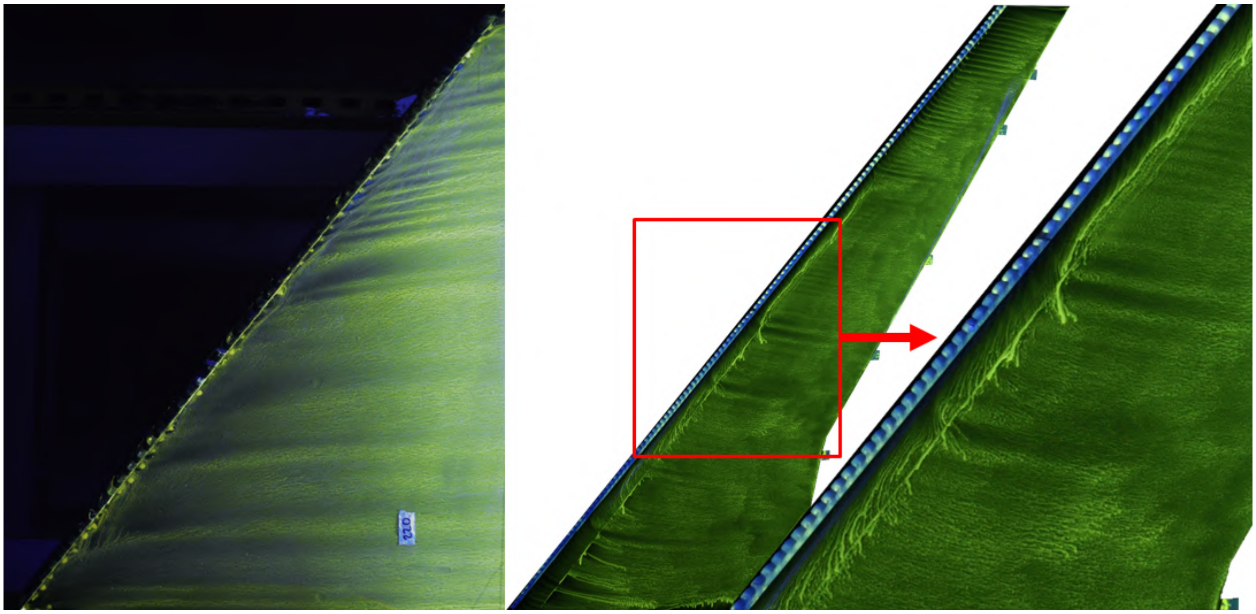

Figure 4.13: Comparison of swept flat plate and CRM65 oil flow visualization; (left) discontinuous step, flap angle of $-5°$, $Re_h = 5.03 \times 10^4$, (right) Medium Gap 3-D Discontinuous, $\alpha = 6°$, $Re = 1.6 \times 10^6$

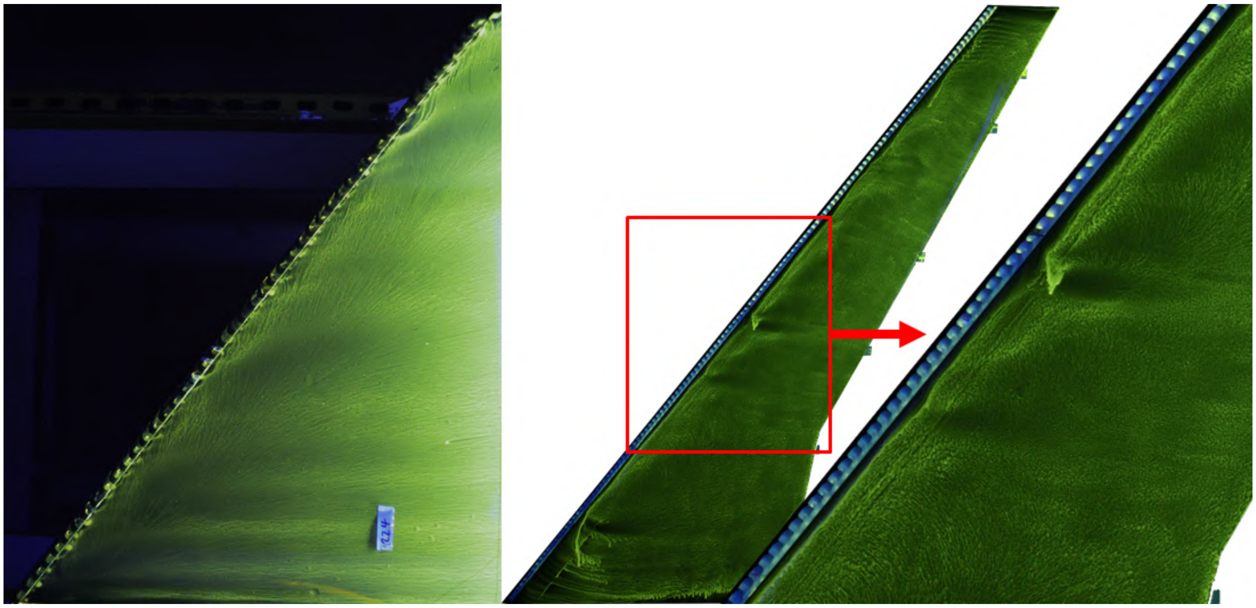

Figure 4.14: Comparison of swept flat plate and CRM65 oil flow visualization; (left) discontinuous step, flap angle of $+4°$, $Re_h = 5.03 \times 10^4$, (right) Medium Gap 3-D Discontinuous, $\alpha = 8°$, $Re = 1.6 \times 10^6$

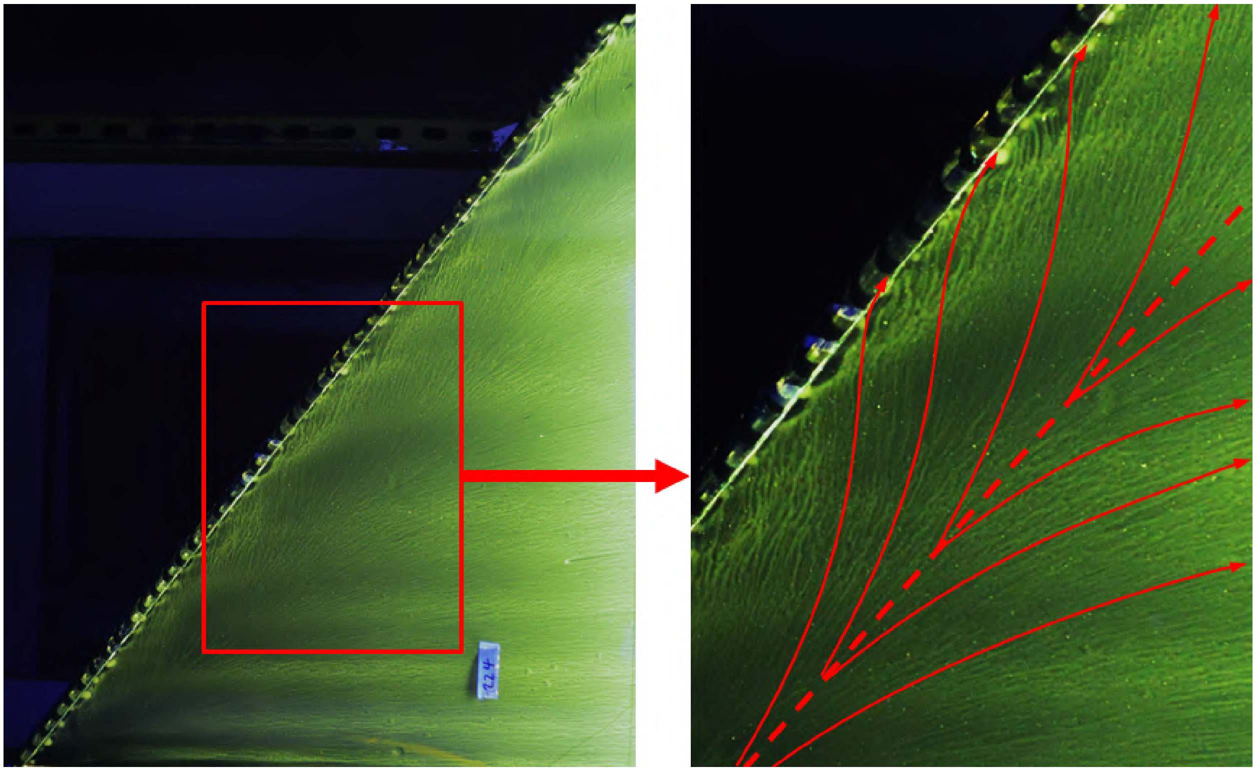

Figure 4.15: Close-up view of swept flat plate oil flow visualization of discontinuous step, flap angle of $+4^\circ$

4.2 Effect of Spanwise Discontinuities in Step

Previously, Section 4.1 examined the effect of flap angle on the flowfields associated with each step. This section will provide a detailed analysis of the structures contributing to Type II streamwise streaks behind the discontinuous step. The streaks in question are most clearly visible at the baseline configuration of -10° flap deflection and a wind speed of 60 m/s. The following subsections will discuss the discontinuous step and its two variants: the discontinuous step with alternating gaps blocked, and the solid step with the discontinuous center section installed. Along with special detailed oil flow visualization techniques, further discussion will be made in regard to changes in the Type II streamwise features as flap deflection is increased.

4.2.1 Standard Discontinuous Step

Uncertainty remains as to the exact flow physics contributing to the Type II streaks. During the course of the SWIP research project, multiple analyses have been conducted for scallop artificial ice shapes of varying fidelity that exhibit this type of flowfield. Sandhu [60] suggested that the features were ”jets,” or simply regions of higher velocity accelerated by confinement of the flow between the larger three-dimensional features of the ice shape. Camello [59], and later Bragg et al. [45], Broeren et al. [44], and Woodard et al. [19], hypothesized that the Type II features were the result of counter-rotating streamwise-running vorticity. The following discussion of results begins with detailed flow visualization downstream of the discontinuous step to identify the nature of the streaks. This effort is unique, as this type of flow visualization would have proved much too time consuming to conduct during previous SWIP wind tunnel test campaigns. Next, the dramatic changes in the flowfield associated with the discontinuous step at various flap settings are discussed in further detail. Specifically, the introduction of two distinct types of streamwise features.

Stippled Oil Droplet Flow Visualization

During the SWIP wind tunnel test campaigns and testing for the present work, the primary flow visualization technique employed was fluorescent-oil-film surface flow visualization. The strength of this technique lies in the balance between imaging the flow across the entire surface of the model with considerable detail, and allowing images for multiple runs to be collected efficiently. This balance is due to the uniform film of oil and dye that is rolled across the entire model. A complete image is obtained, and resetting for the next case is as simple a redistributing the oil from the previous run with a roller. While other methods of flow visualization may be much more time consuming or messy, thanks to the hard work and time spent in development by researchers like Diebold [68], the current oil flow method is simple and effective. However, the method is a trade-off between greater levels of detail and time-efficiency, the latter of which is especially

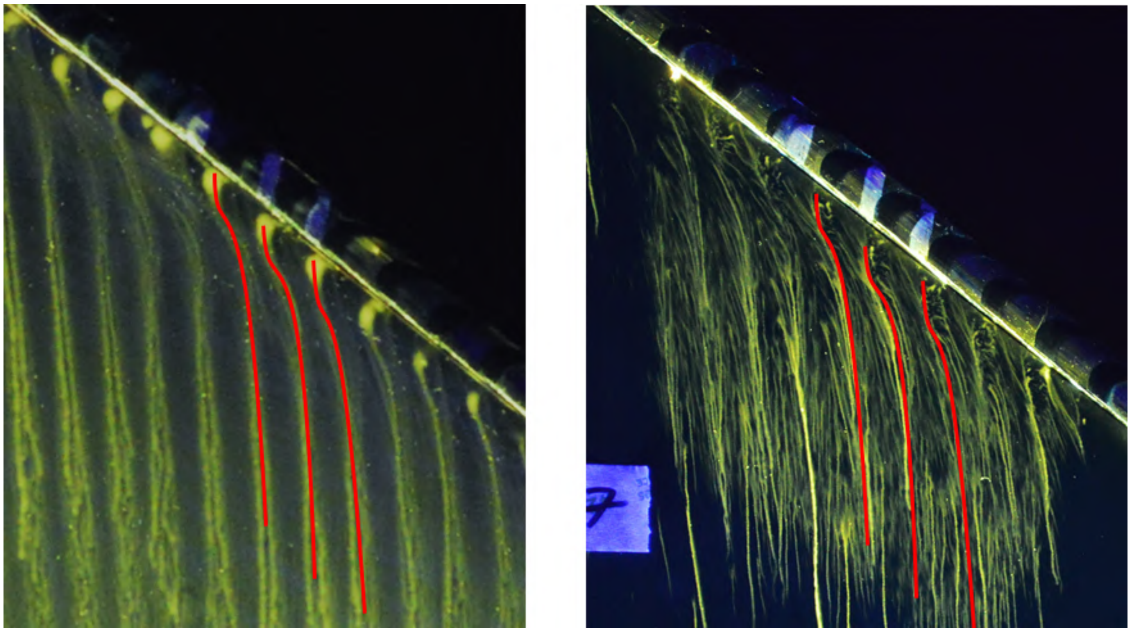

Figure 4.16: Comparison of the oil film and stippled droplet oil flow visualization techniques at the same region downstream of the discontinuous step at -10° flap angle and 60 m/s; (left) oil film, (right) stippled oil droplets

critical during costly wind tunnel testing. During experimentation at the University of Washington 3'x3' low-speed wind tunnel for the present work, the time frame was not as restrictive as a larger-scale test campaign. The freedom that this fact allowed for a special variation of the existing surface flow visualization technique to be developed with the specific aim of investigating Type II streamwise streaks. The method in question was the stippled oil droplet technique, the steps of which are described in Section 3.5.

The stippled oil droplet flow visualization technique relied on the fact that a droplet of oil-dye mixture leaves a visible trace on the vinyl sheeting as shear forces from the surrounding flow push it. When a precise density of droplets is applied to the model surface, suggestions of the surface streamlines for even small features of the flow are revealed. In contrast, a film of oil may be uniformly affected by shear in a certain region. In this case, rather than identifying small-scale flow structures, only a region devoid of oil is left behind. This is the case with Type II features observed behind the discontinuous step and the Medium Gap 3-D Discontinuous artificial ice shape for the CRM65. A comparison between the two flow visualization methods is shown in Fig. 4.16

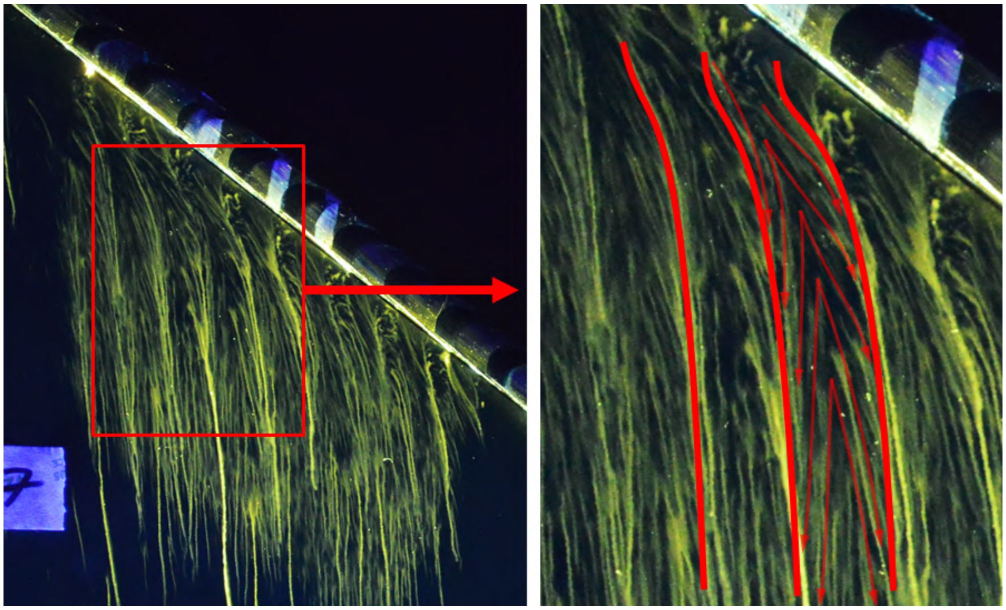

Figure 4.17: Close-up view of the stippled droplet oil flow visualization image downstream of the discontinuous step at -10° flap angle and 60 m/s

for the discontinuous step near the centerline of the plate at the baseline flap angle and airspeed. Due to the time-consuming nature of the oil stippling method, the discontinuous step at baseline conditions was the sole configuration tested. As described, each droplet deposited on the model surface in the oil stippling method left a visible trace as it flowed along the plate. The oil film method instead resulted in nondescript dark streaks, which do not provide information as to their constitutive flow structures.

Fig. 4.17 provides a closer examination of the surface streamlines suggested by the droplet traces of the stippled-oil flow visualization. The foremost features are the Type II streamwise features that are a primary motivating factor for the present study. The red arrows in the image follow the traces left by the oil within a region that would have appeared as a dark streak in the oil film method. The traces suggest that oil flows in both the inboard and outboard directions from the center of the streak. The bi-directionality indicates that, in the region in which the oil-stippling flow visualization was conducted, the Type II features are each composed of a pair of counter-rotating vortices. Carefully examining the oil film surface flow visualization compared in Fig. 4.16, each light streak located between pairs of dark streaks appears to have oil pooling on both the inboard and outboard sides. The result is seen as two streamwise-running lines of pooled oil. The most likely reason for oil pooling in this manner is lateral shear from either side of the streak. This observation represents additional evidence that each streak is composed of a vortex pair. The two-sided oil pooling only persists a short downstream distance before becoming less distinct and eventually disappearing altogether. The limited length of the pairs of oil lines may be a sign that the vortex pairs only exist for a short length before decaying, perhaps due to growing turbulent length scales reducing their coherence.

Near the step face, the composition of the flowfield cannot be definitively identified with the oil flow image alone, Fig. 4.17. Behind each feature in the discontinuous step is a wake region with low shear. These regions are seen as periodic groupings of oil droplets just downstream of the step which have experienced little movement. Further, the red surface streamlines overlaid on the oil flow image suggest that the counter-rotating vortex pairs begin directly downstream of these regions of low shear. In an effort to further probe the causes of the streamwise streaks and the vortex pairs, Fig. 4.18 plots the 3-D pressure distribution behind the discontinuous step at the same conditions as the oil flow: -10° flap angle and 60 m/s. The streamwise row of taps is located downstream of a gap, and on either side of the row are two solid components of the discontinuous step. It is behind these solid features in the first spanwise pressure row that small variations in the pressures are seen. Specifically, in the wake of each solid feature, there is a region of slightly higher pressure, or more positive C_p. The variations are so slight, however, that it is difficult to form a compelling hypothesis using these pressure data. It is also interesting to mention that the pressure coefficient is positive at every tap in the distribution, which is in some ways similar to the flow over the lower surface of an airfoil.

Drawing attention now to the regions downstream of the gaps in the step, the oil traces are seen to have a noticeable outboard and downstream directionality. This may be seen within the region of the plate just outboard from the red overlay. The oil traces then appear to converge into what would be a light streak had this image used the oil-film method. The direction of the oil traces is in contrast to the streaks just a short distance downstream, which flow both inboard and outboard. This evidence suggests that within a short distance the flow between the gaps, which has a strong outboard velocity component, either contributes to the formation of the vortex pair, or is otherwise redirected as it encounters the wake-regions. In this case, the incomplete image that surface flow visualization provides becomes apparent. It is clear that in order to gain a complete understanding of this type of flow phenomena, off-body flow measurements will be required.

To summarize the previous analyses, stippled oil droplet flow visualization has shown evidence as to the composition of Type II streamwise streaks behind the discontinuous step. Each solid feature of the spanwise-varying step produces a low-shear wake region. Downstream of these regions, pairs of counter-rotating vortices are formed and soon lose coherence a short distance downstream. Flow passing through the gaps in the step results on flow behavior that is difficult to definitively identify. It is possible that this flow interacts with the wake regions, perhaps even playing a role in the formation of the streamwise-running vortex pairs. In the next section, a detailed analysis will be given to how the Type II streaks at the baseline flap setting change at higher flap angles.

Flap Angle Effects

Section 4.1.2 described the shift from streamwise streak-dominated flowfield to modified separation bubble in general terms. The following section is intended to provide a more detailed analysis of the evolution of the Type II streaks behind the discontinuous step, which was analyzed in the preceding subsection. Similar discussions of flap angle effects will follow for the two discontinuous step variants, ending with an overall comparison at the end of the section.

Fig. 4.19 compares oil flow visualization for the discontinuous step at each flap setting. In this set of images, the light streaks where oil has collected are highlighted with yellow vertical lines. At the baseline flap angle of -10°, which was discussed in depth in the previous subsection, there is one streamwise streak per gap in the step. The one-to-one ratio was attributed to the counter-rotating vortex pairs, which appeared to develop in the wakes of each solid feature of the step. It is interesting to note, then, that streamwise streaks are still visible at higher flap angles,

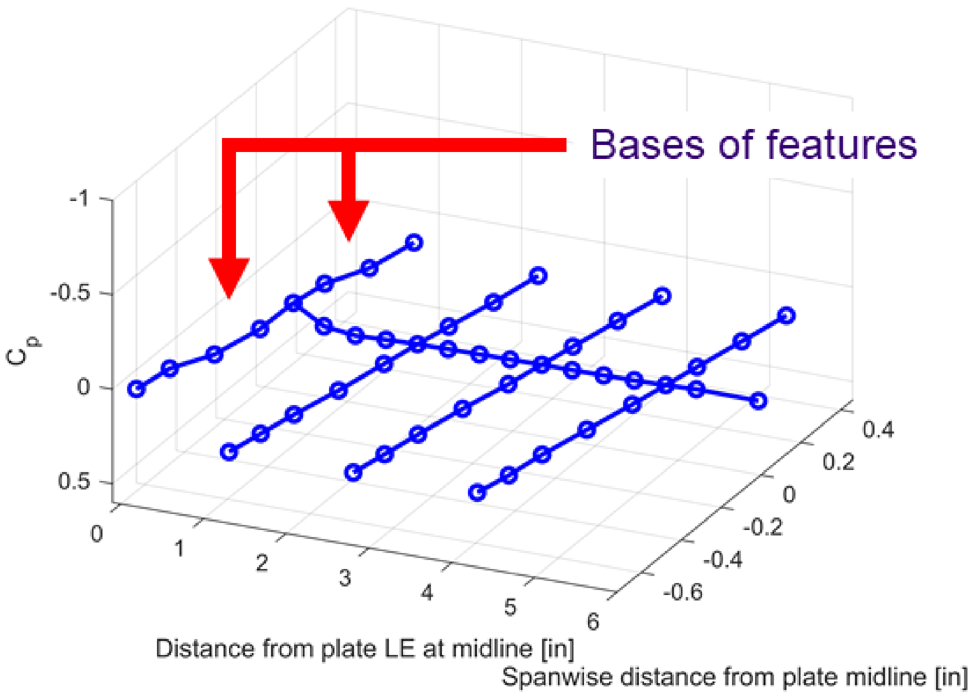

Figure 4.18: Pressure distribution downstream of the discontinuous step at $-10°$ flap angle and 60 m/s. Red arrows indicate the location of solid features of the step.

albeit with large differences. The most visible dissimilarity between the flow visualization at each flap angle is that the ratio of gaps to streaks has changed significantly. For instance, with the flap at $+4°$, there are only three clear streaks downstream of a spanwise extent of the step that features 11 gaps. With a flap angle of $-5°$, this ratio changes depending on the spanwise station. Inboard, three large streamwise flow features are present behind 15 gaps in the step. Further outboard, the flow resembles that of the baseline flap angle, though a handful of gaps do not have streaks in their wakes. These spanwise variations are likely a result of the flow angularity distributions plotted in Fig. 4.3. As a note, the discussion of the ratio of gaps in the step to observed streamwise streaks is not a definitive quantity. Rather, it is an approximation that is meant to illustrate general differences in the type of flowfield.

A closer view of the streamwise features downstream of the discontinuous step at a flap angle of $+4°$ is shown in Fig. 4.20. In this image, the oil flow appears to be a superposition of two distinct flowfields. First, near the step faces are the spiral traces of oil indicative of separation

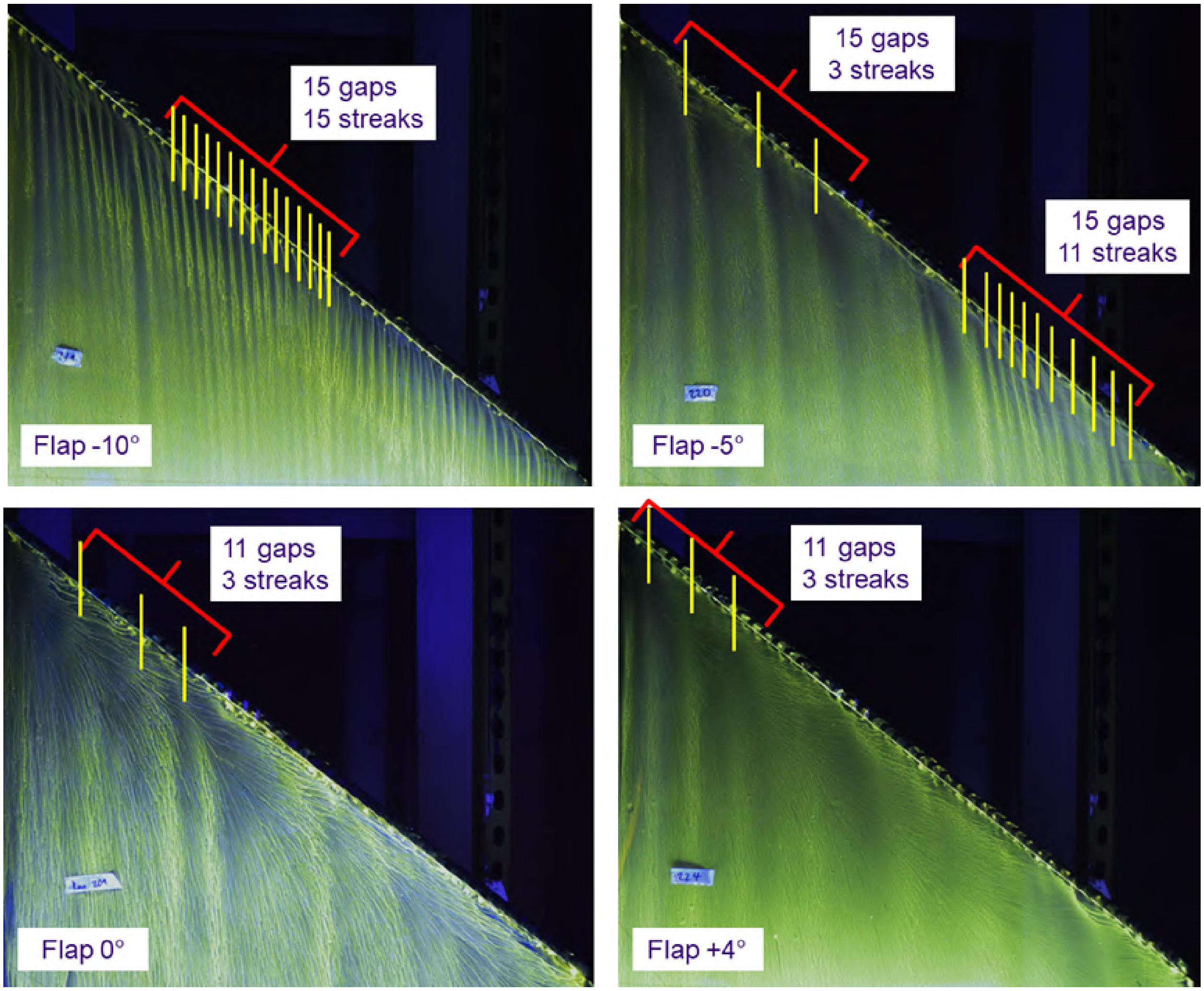

Figure 4.19: Fluorescent-oil surface flow visualization behind the discontinuous step at 60 m/s with yellow lines indicating a streamwise feature; (upper left) -10° flap deflection, (upper right) -5° flap deflection, (lower left) 0° flap deflection, (lower right) $+4^{\circ}$ flap deflection

and a leading-edge vortex. Oil flow lines of the same type are seen across the entire span of the solid step. However, in the case of the discontinuous step, there is no secondary separation, which would be visible as a straight region of pooled oil against the step face. The similarities between the streamwise pressure distributions of discontinuous and solid step at this flap angle are evident in Fig. 4.21. Both steps exhibit a large region of negative pressure that is characteristic of separated flows. At this flap deflection, the stagnation point has likely shifted low enough on the leading edge to cause separation that may even partially bypass the discontinuities in the step. The second flowfield is composed of the periodic streamwise features that are visible even within the

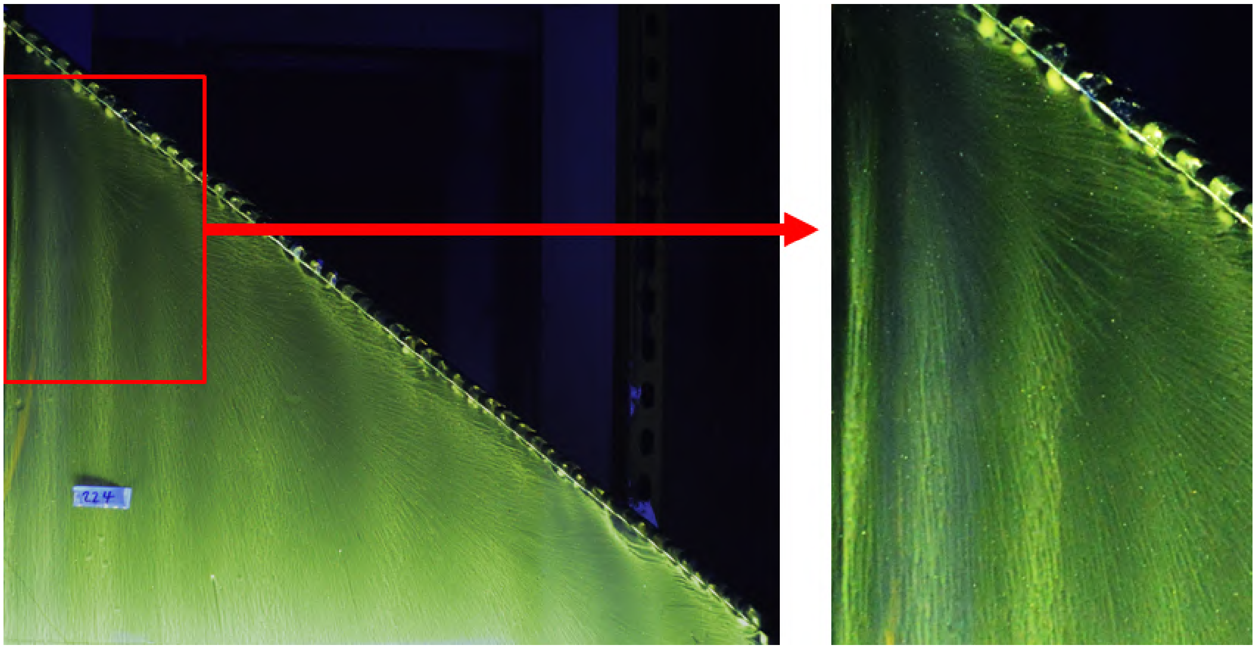

Figure 4.20: Fluorescent-oil surface flow visualization behind the discontinuous step at 60 m/s and $+4^{\circ}$ flap deflection

purported separation bubble and leading-edge vortex region. The streaks, unlike those behind the discontinuous step at the baseline flap setting, do not have the same indications of counter-rotating vortices. Rather, the streaks emerge more subtly in the form of slight deviations in the flow lines of the reattaching shear layer. Specifically, within the light regions of the streaks, the flow appears to have only a streamwise component of velocity. The oil traces within dark regions of the flow, on the other hand, suggest that the local flow has a significant outboard component for a considerable distance downstream from the step.

One possible explanation for the features observed in the oil flow in Fig. 4.20 is as follows: first, from the general curvature of the oil traces within the dark streaks, it may be assumed for the sake of argument that a coherent streamwise-running vortex is present. In a frame looking upstream, this vortex rotates counter-clockwise, based on the oil in the dark streak being swept outboard and downstream. In addition to the counter-clockwise vortex, there may a clockwise streamwise-running vortex of lesser strength located over the light streamwise streaks. This vortex is only of sufficient strength to cancel out a portion of the outboard flow at the surface, leaving only slower, streamwise flow within the light streaks. As for the underlying cause of the con-

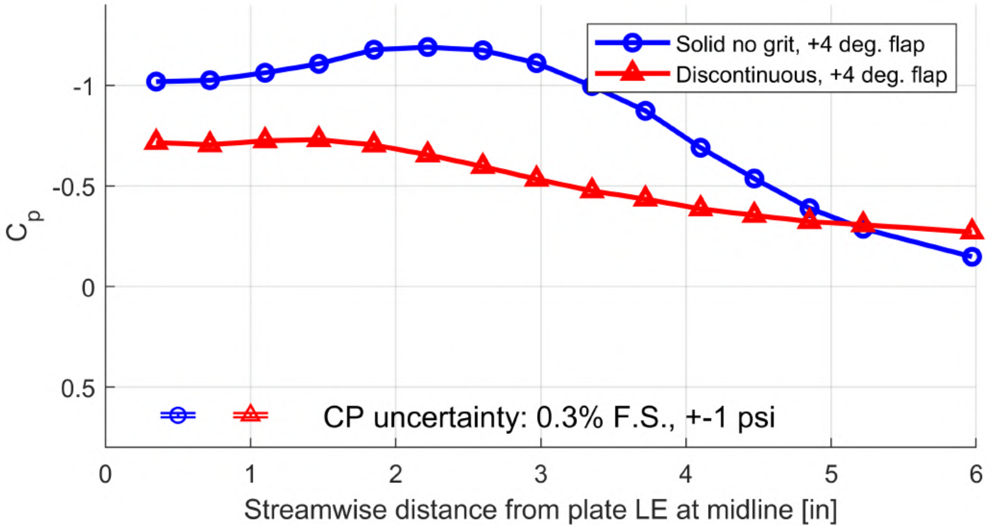

Figure 4.21: Comparison of streamwise pressure distributions behind the discontinuous and solid steps at 60 m/s and $+4^{\circ}$ flap deflection

jectural vortex pairs, Jacobs [4] hypothesized that a streamwise vortex instability excited by ice shape geometries might result in streamwise vorticity. The rough and irregular features of three-dimensional ice shapes provide upstream perturbations, which induce Λ-shaped deformation of the spanwise vortices present in the separated shear layer. The discussion of the streamwise shear layer instability continues in Section 4.3.

At this point, the underlying cause and the exact flow physics of the second type of streamwise streak remain unclear and would require further testing to determine. Regardless, it is certain that the Type II streaks present behind the discontinuous step at -10° are distinct from those that appear at $+4^{\circ}$. The following subsections detail configuration flowfields of the two remaining discontinuous step variations: alternating blocked gaps, and the solid step with the discontinuous center section installed. These geometries result in streamwise features similar to the two types discussed in the present section. For easier reference moving forward, the streaks comprised of counter-rotating vortices seen at a flap setting of -10° will be referred to as ”vortex generator-type” streaks. Each solid section of the discontinuous step acts to create a highly vortical flow downstream, which in some ways is comparable to the function of a vane-type vortex generator. The vortex generator-type is most visibly identified by the one-to-one ratio of gaps to streaks. The second type of streamwise feature, which was of uncertain origin, will be referred to as ”shear layer instability-type” streaks, after the most plausible explanation available at the time of writing. This Type II streak may be distinguished in oil flow visualization by the greater number of gaps than streaks in a given region, as well as the increased streak width and apparent CCW spiral oil traces. In the proceeding subsection, an analysis of the flow behind the discontinuous backward-facing step with alternating gaps blocked will be presented and compared to the standard discontinuous step.

4.2.2 Discontinuous Step with Alternating Blocked Gaps

Due to constraints on time and manufacturing capability, only a single full-span discontinuous step was constructed for the present study. Ideally, additional step heights or gap widths would be included in testing; however, a low-cost modification to the step was covering every second gap with a layer of tape. This discontinuous step variation was described in Section 3.3 and pictured in Fig. 3.10. While this modification does not change the gap width, it does change the ratio of gap to solid feature across the span and the periodicity of the gaps.

Fig. 4.22 compares the fluorescent-oil flow visualization images for the alternating discontinuous step at the four flap settings. As with the standard discontinuous step, the baseline flap angle of -10° produces distinct Type II streamwise flow features. The differences with this configuration are that the streaks do not cover the entire span, and have a greater width. Most importantly, is that the number of streaks in the outboard region highlighted is now less than the number of gaps. This also holds for the highest flap angle of $+4^\circ$, shown on the right. To the first point of the partial-span streaks, the flowfield resembles that of the standard discontinuous step at a -5° flap setting, pictured in Fig. 4.13 in Section 4.1.2. In that configuration, distinct spanwise streaks were also only present on the outboard region of the plate. Previously, this was attributed to spanwise variations in the local flow angle that was quantified using five-hole probe measurements, Fig. 4.3. At negative flap angles, the local angle was seen to decrease across the span.

One notable observation is that there are suggestions of shear layer instability-type streaks in the oil flow of the configurations of this geometry variation, regardless of the flap deflection. Between the flap angles visualized in Fig. 4.22, the ratio of gaps to streaks increases as well. To show these changes, all flap deflections for this configuration are placed side-by-side to show the evolution of the streamwise streaks. In some cases, such as with a flap setting of 0°, the number of streaks was uncertain. There was no decisive rule as to what qualified as a streamwise feature. Overall, the flow features varied significantly in size, spacing, and visibility, suggesting complex flow interactions. To reiterate, the ratio of streamwise streak to gap is not an exact measure of any single property. Rather, the ratio is intended to illustrate that for reasons that are not clearly understood, streaks still appear despite that flow separation may at least encompass the discontinuities.

Fig. 4.23 presents a closer look at the Type II features downstream of the step at the baseline flap setting. The previous section, which introduced the shear layer instability-type streaks, described the regions as having a noticeable outboard flow component. In the present case, as diagrammed, the flow is seen to have similar traces in the oil flow visualization. Interestingly, in the region close to the step face, one or two bright lines of pooled oil are seen to converge into the periodic Type II features that are clearly visible. This may be an artifact of pooled oil droplets being pushed by the strong outboard flow component in this neighborhood. On the other hand, it may instead be suggestive of the process by which the downstream number of streaks becomes less than the number of gaps in the step. In other words, perhaps the total light streaks which converge correspond to the number of gaps. In the region close to the step face, each gap may locally produce streamwise vorticity. However, the configuration is such that it causes vortices to coalesce before reaching a stable structure downstream.

Unfortunately, the pressure tap array was too far inboard to record the pressures in the region of the plate which showed streamwise streaks. Despite this limitation, the mean pressure distribution reveals significant spanwise variation, Figs. 4.24 and 4.25. In Section 3.3, Fig. 3.10 showed that the streamwise row fell behind a gap in the step, and the spanwise rows cover half of each of the neighboring solid features. At the baseline flap setting of -10°, the streamwise row shows the presence of a small low-pressure region that may suggest a leading-edge separation bub-

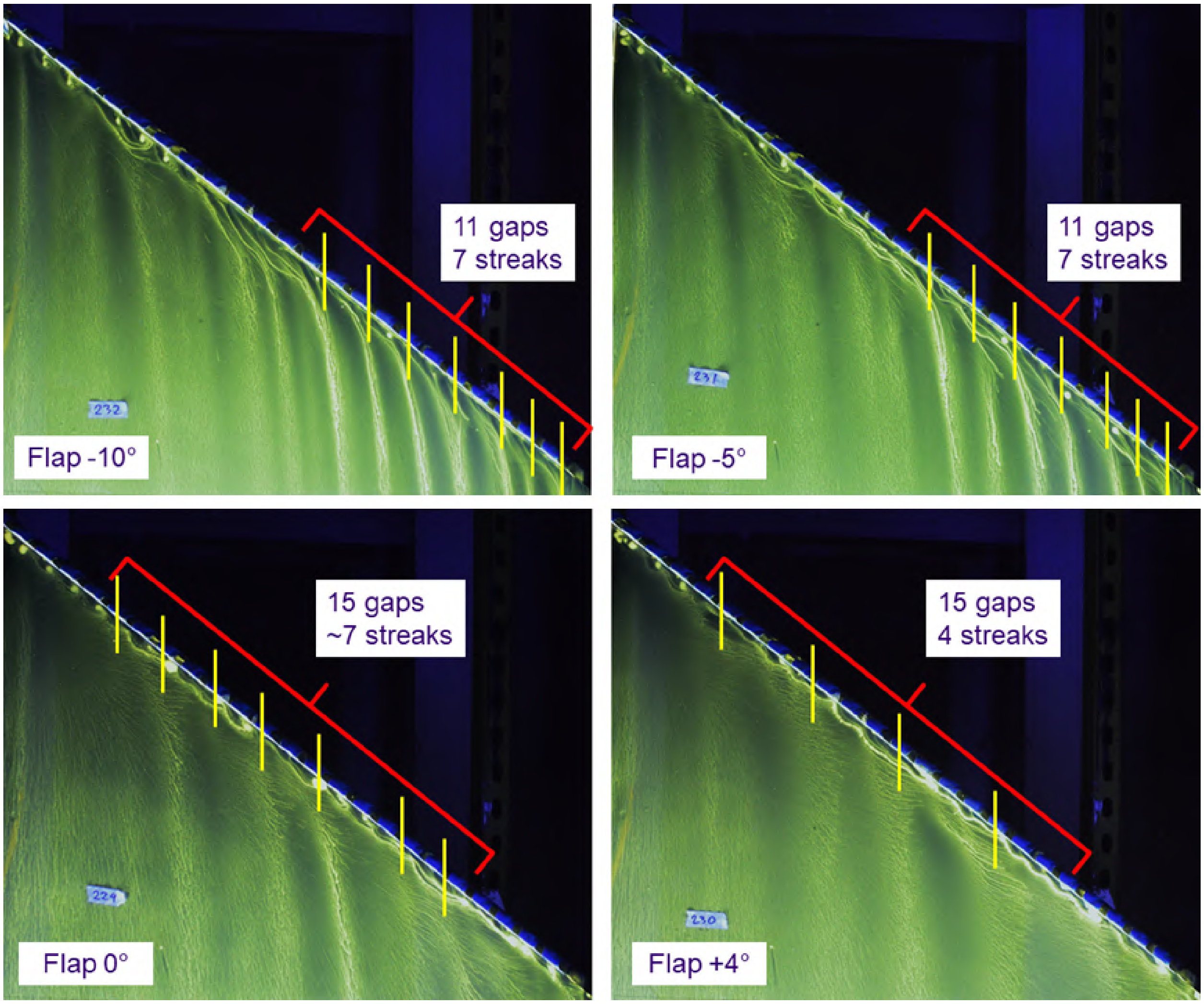

Figure 4.22: Fluorescent-oil surface flow visualization behind the discontinuous step with alternating gaps blocked at 60 m/s with yellow lines indicating a streamwise feature; (upper left) -10° flap deflection, (upper right) -5° flap deflection, (lower left) 0° flap deflection, (lower right) $+4^\circ$ flap deflection

ble, Fig. 4.24. To either side of the streamwise row, the first spanwise tap row shows a significantly lower pressure region outboard and a higher pressure region inboard, both behind solid features of the step. Oil flow visualization of the area in which pressures were taken has many complicated features. As a result, it is difficult to conclude as to why this spanwise pressure variation occurs. The pressure distribution at a flap angle of $+4^\circ$, shows the presence of the separation region that developed downstream of the standard discontinuous shape at high flap angle configurations as well.

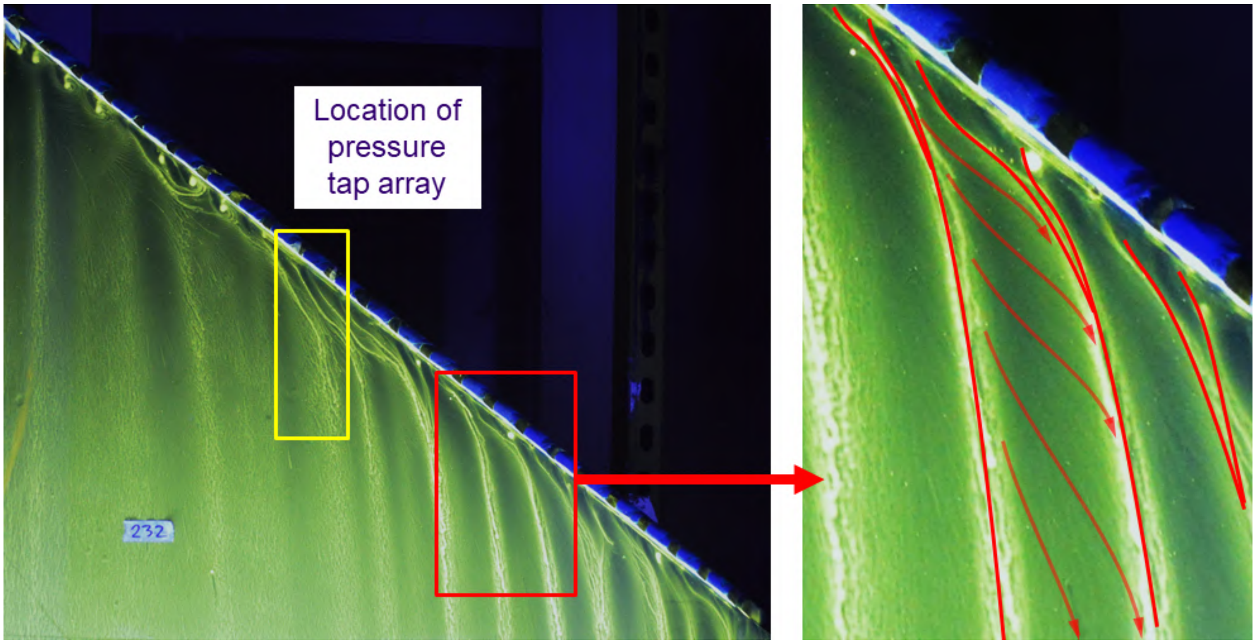

Figure 4.23: Close-up view of the fluorescent-oil surface flow visualization behind the discontinuous step with alternating gaps blocked at -10° flap deflection and 60 m/s

A final observation is that with all flap deflections tested, the flow directly downstream of the step faces exhibits clear spanwise-running oil flow. The outboard flow component is also seen in the curvature of the streamwise streaks, regardless of the ratio of gap to streak. Fig. 4.26 presents a conjectural drawing of a flowfield that may explain the evidence that has been presented in this subsection through pressures and oil flow visualization. At certain flap angles, the freestream flow impinges on the leading edge at an angle that creates a small separation bubble. The swept leading edge results in a spanwise-running spiral vortex within this recirculation region. Above, whether by the vortex generator effect or a streamwise shear layer instability, a large counter-clockwise streamwise-running vortex develops. The superposition of these two results in streamwise streaks that are inclined in the outboard direction near the step face, along with additional outboard-flowing oil within the hypothesized separation bubble. As shown in Fig. 4.23, the streamwise flow features sweep oil away close to the step face, even within the bubble region. If the separation bubble was highly unsteady as it interacted with the strong vortical flow overhead, perhaps it would result in the observed superposition. With increasing flap deflection, the separation bubble grows until either the streamwise vortices no longer occur or they are too far from the plate surface to be visible in the surface oil flow. Again, for an accurate understanding of these complicated flow phenomena, off-body measurements such as PIV would be required. Unsteady surface pressure measurements would also provide valuable insights into phenomena like reattachment length fluctuations.

In review, the discontinuous step with alternating gaps blocked resulted in a flowfield that was equally, if not more, complicated than that of configurations of the standard discontinuous step. This geometry showed that shear layer instability-type streamwise streaks vary with flap deflection, and range from strongly periodic to irregular and indistinct with varied spacing. A speculative explanation for the general flowfield structure was proposed, involving a small separation bubble and a spanwise leading-edge vortex interacting with streamwise-running instability vortices above. During experimentation on a high-fidelity horn ice shape, Gurbacki [2] and Jacobs [4] noted that periodic ”cell-structures” could not be attributed to a single geometric feature. In this same way, the Type II flow features in the present geometry do not have a clear dependency on the locations of gaps in the step. Based on observations from oil flow visualization of the CRM65 fitted with the High Fidelity Maximum Scallop artificial ice shape, realistic ice shapes are most likely to exhibit something like the instability-type streaks. Thus, the latter type of streamwise flow features are of greater importance to the understanding of swept, iced-wing flowfields. Perhaps certain scallop accretions could produce something like the vortex-generator effect, however, the shear layer instability was observed to be prevalent during CRM65 wind tunnel testing, and is the less-understood phenomenon. In the next subsection, the flow behind the third and final discontinuous step variation is discussed.

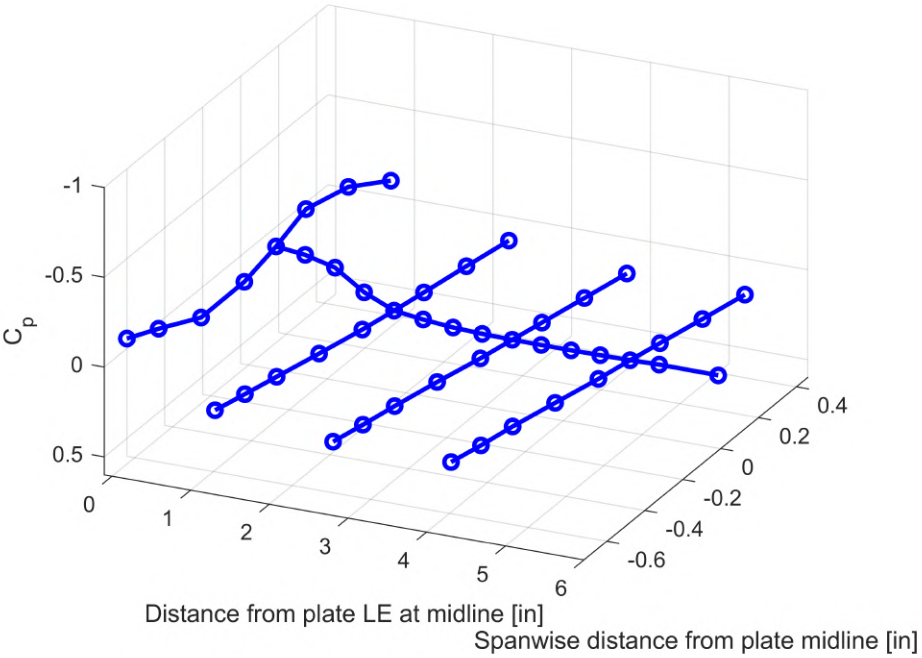

Figure 4.24: Pressure distribution downstream of the discontinuous step with alternating gaps blocked at -10° flap angle and 60 m/s

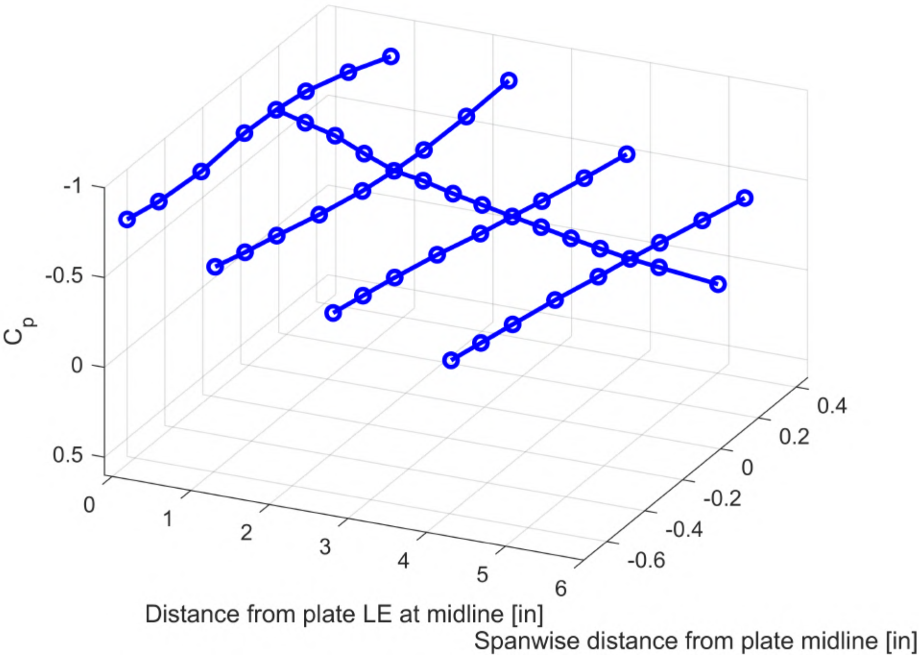

Figure 4.25: Pressure distribution downstream of the discontinuous step with alternating gaps blocked at $+4^\circ$ flap angle and 60 m/s

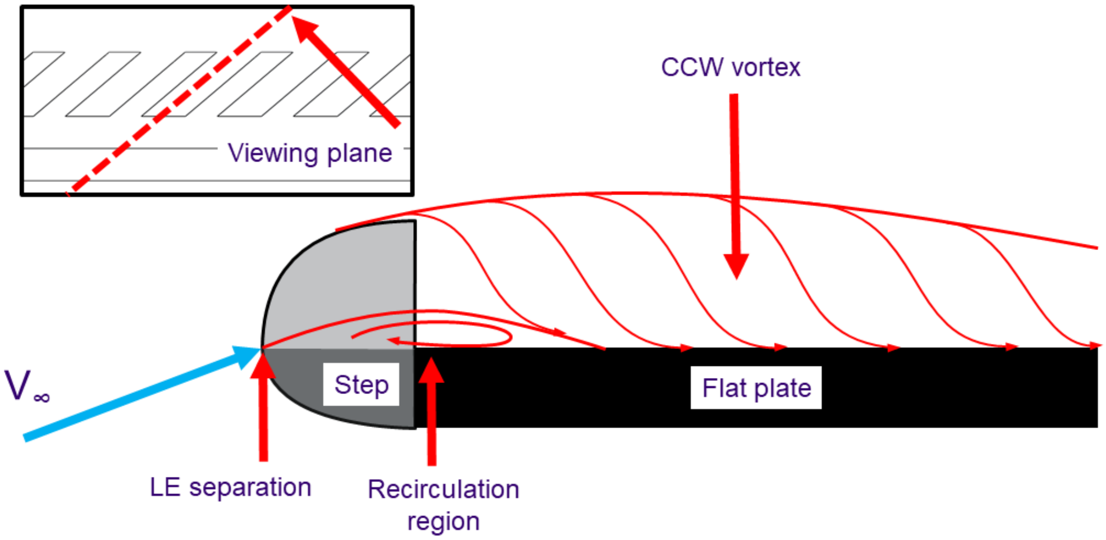

Figure 4.26: Diagram illustrating a proposed flowfield about the discontinuous step to explain the observed surface flow visualization patterns

4.2.3 Solid Step with Discontinuous Center Section

As mentioned in Section 3.3, each leading-edge step consists of five removable sections that are mounted on the underside of the flat plate. This arrangement allows for any combination of solid and discontinuous step sections. For the following tests, the middle section of the full-span solid step was replaced with that of the discontinuous step. The result was a solid backward-facing step with a single, central region of spanwise discontinuities. This type of geometry as not tested as a part of the SWIP research program. However, the set-up for this configuration required no special effort and yielded some interesting, if complicated, results.

As was shown for the alternating discontinuous step, Fig. 4.27 compares the oil flow visualization images for each of the four flap settings. At the baseline flap deflection, the flow behind the discontinuous center section locally resembles that of the standard discontinuous step. Specifically, the ratio of gaps to streaks is again one-to-one. At the inboard side of the plate, the beginnings of the spanwise-running leading-edge vortex that is characteristic of the solid step are visible. Notably, the meeting point of the streamwise streaks and the leading-edge vortex suggests that the Type II flowfield overpowers that of the solid step configuration. Outboard just beyond the center

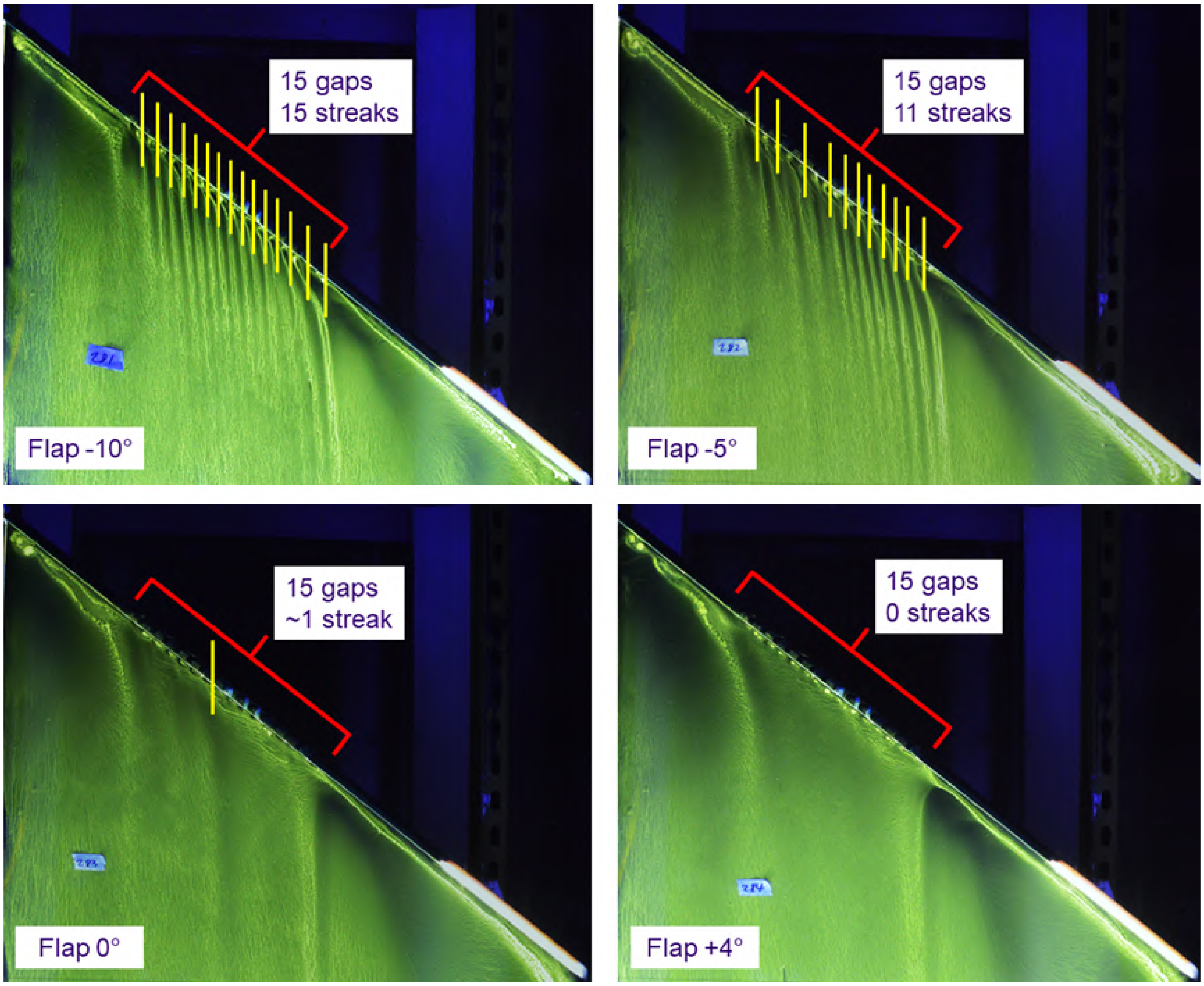

Figure 4.27: Fluorescent-oil surface flow visualization behind the solid step with the discontinuous center section installed at 60 m/s with yellow lines indicating a streamwise feature; (upper left) -10° flap deflection, (upper right) -5° flap deflection, (lower left) 0° flap deflection, (lower right) $+4^\circ$ flap deflection

section, a leading-edge vortex again forms, though it soon encounters the test section wall and is turned downstream.

With the flap at the next setting of -5°, a remarkable change begins to take place. From the close-up view of the oil flow visualization in Fig. 4.28, it may be seen that the Type II flow features that emanated from each gap are converging. What remains are several visible streaks downstream that appear fewer than the number of gaps. Whether this is a result of interactions with the leading-edge vortex from the solid step, the spanwise variations in local flow angle, or a combination of multiple factors is uncertain. Another explanation may be that this phenomenon is a critical component of the transition from the vortex generator-type streaks to instability-type streaks. As the flap angle increases further, the number of Type II streaks continues to decline until there are no visible streaks at all. Finally, at a flap angle of $+4°$, it is also interesting to note that the discontinuous center section still disrupts the solid step configuration flowfield despite the flow separation that is suggested by the pressure distribution. This oil flow image may show that there is still significant streamwise component flow through the discontinuities in the step. The leading-edge vortex from the solid portion of the step is still eliminated despite the outboard-flowing oil close to the discontinuous section step faces.

While this particular geometry did not have a real-life comparison, it still provided a fascinating new perspective. For instance, parts of the flowfield seen in the oil flow suggest that as the flap angle was changed, the streamwise streaks from some of the gaps fade away. At the same time, the remaining Type II features appear wider and slightly less distinct. Furthermore, despite evidence indicating that a leading-edge separation and spiral vortex are present behind the step, it is not sufficient to disrupt the strong streamwise component of velocity passing through the gaps. Though the results presented in this section are a wealth of new information, there is still a tantalizing amount that is still not known. What has been shown previously is that there are at least two types of streamwise vortical flow features. Stippled oil droplet flow visualization helped determine the composition of the vortex generator-type streaks. However, the other type was not nearly as clear. Likely, many of the most important flow phenomena over these spanwise discontinuities occur too far off-body to be analyzed using the present methods.

4.2.4 Summary of Streamwise Streak Variation

Thus far, each of the three discontinuous backward-facing step variations has been discussed. This final subsection will compare and summarize the results. In light of the new topics introduced previously, the results of the CRM65 and the Maximum Scallop 3-D Discontinuous shapes will be revisited as well.

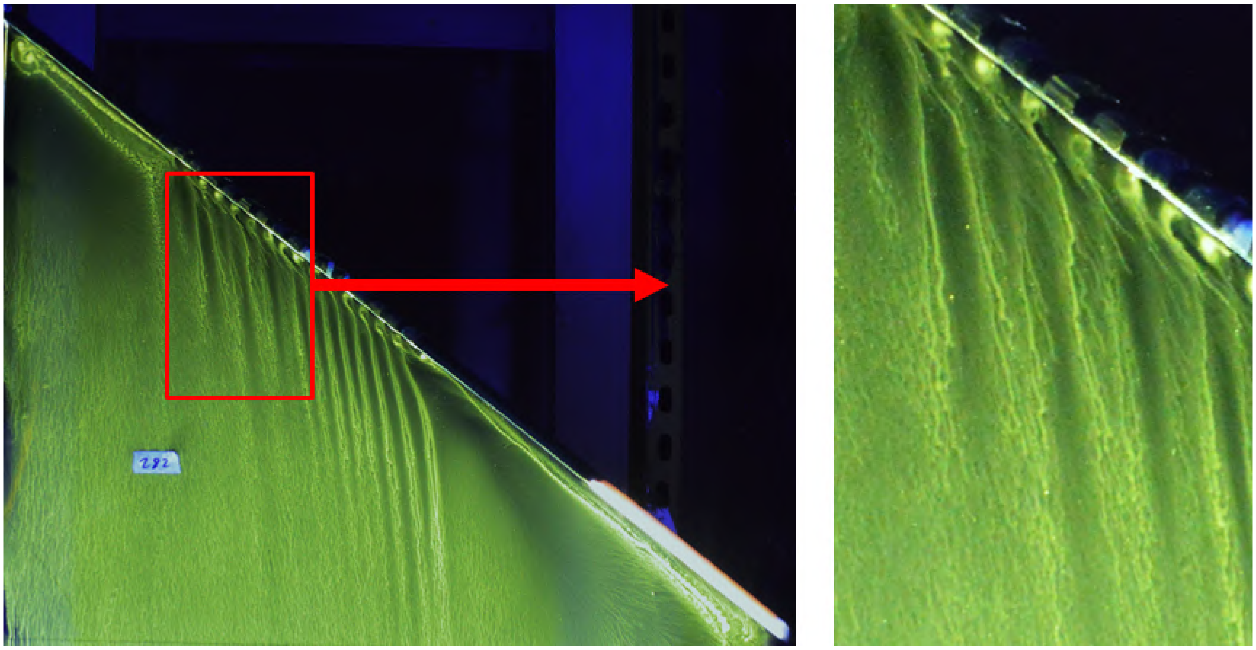

Figure 4.28: Close-up view of the fluorescent-oil surface flow visualization for the solid step with the discontinuous center section installed at a flap angle of $-5°$ and 60 m/s

In Chapter 3, the design of the discontinuous backward-facing step shape was described. For this geometry, the widths of gaps and solid features, along with the cutting plane inclination, was based on the Medium Gap 3-D Discontinuous artificial ice shape. Woodard et al. [22] describes the design of other variants of the 3-D Discontinuous shape, which had a range of gap widths and cutting planes. One such variant, the Small Gap 3-D Discontinuous had narrower gap and feature widths, which also changed according to a spanwise width distribution based on measurements of the High Fidelity shape. During testing of the Small Gap ice shape on the 8.9% scale CRM65 wing model, fluorescent-oil surface flow visualization revealed a trend in the evolution of the Type II flowfield that is comparable in some ways to the results of the present study, Fig. 4.29. The comparison of oil flow visualization images with yellow lines marking visible Type II features shows that as the angle of attack increased, the streak spacing behind the Small Gap ice shape configuration increased as well. However, even at lower angles, the number of Type II features in the flowfield behind configurations of this ice shape did not correspond to the number of gaps. Similar behavior was observed in the flow behind the discontinuous step variations, in particular the alternating blocked gap step. From the baseline flap angle to the highest, what have been

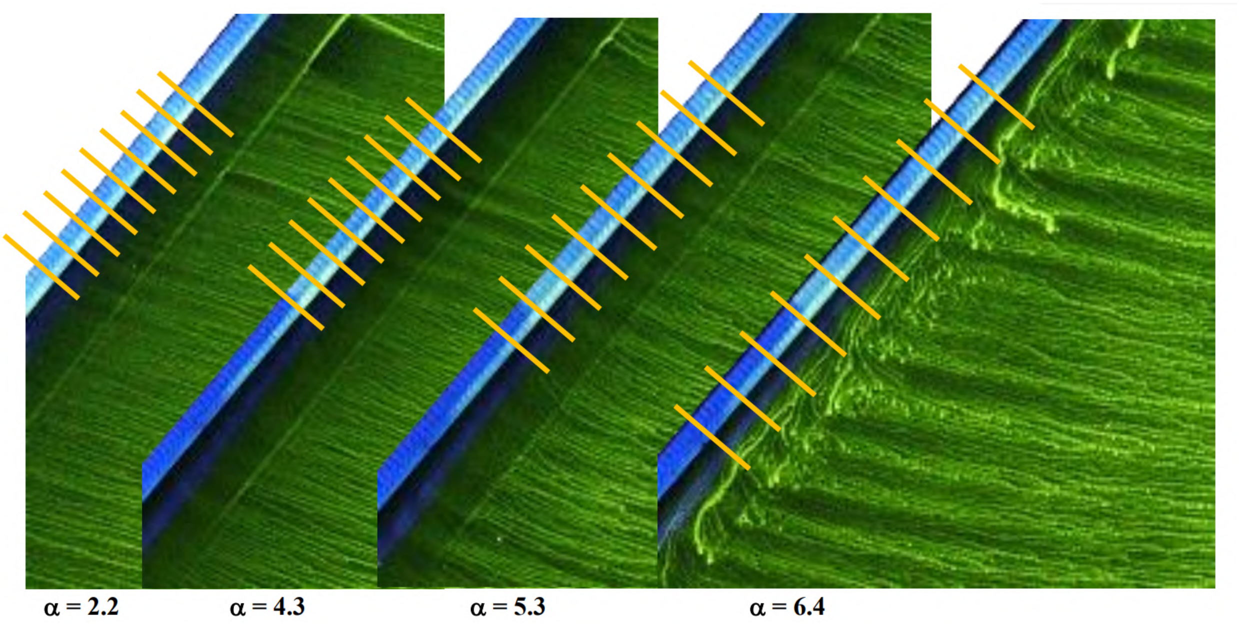

Figure 4.29: Close-up view of CRM65 model from y/b = 0.30 to 0.44 for the Small Gap 3D Discontinuous ice shape at $\alpha = 2.2, 4.3, 5.3$ and 6.4 deg. with markers illustrating the period of the type II flowfield streamwise features, after Woodard et al. [19]

referred to as shear layer instability-type streaks grew in width and became fewer behind a given extent of the step, Fig. 4.22. Thus, in the same manner as the Small Gap 3-D Discontinuous, the ratio of gaps to features increased. With these similarities, it may be reasonable to hypothesize that the same mechanism or flow physics phenomenon is at play in forming the streamwise streaks in the flowfields of the configurations of both geometries. What this mechanism is, however, cannot be determined from the results of the present study.

A final comparison is made at each flap configuration between the pressure distributions downstream of each discontinuous step modification, Figs. 4.30-4.33. The changed gap period in the alternating gap discontinuous step results in the strong spanwise pressure variations seen in Fig. 4.31. Further, the streamwise pressure distribution shown in Fig. 4.30 indicates the alternating gap step possessed a small leading-edge separation. The presence of this separation region was also shown in the surface oil flow visualization in the form of outboard oil flow and the curvature of the streaks. Interestingly, placing the discontinuous center section alongside solid step sections does not appear to have greatly affected the pressure distribution at either flap configuration. This, too, is in agreement with the analysis of the oil flow images. Lastly, at a flap setting of $+4^{\circ}$, all three discontinuous step variations show signs of flow separation, Fig. 4.32-4.33. Though the alternating gap step variation still shows the large region of negative pressure that is reminiscent of the separation bubble behind the solid step configurations, spanwise pressure variations are still present. The periodicity of the discontinuities produces strong changes in the resulting flowfield behind the step configuration.

In summary, the approach of the present work was to investigate the Type II flowfield using a swept flat plate. To this end, a leading-edge backward-facing step with spanwise discontinuities was designed and tested, along with two additional modifications. The configurations of each variation on this step exhibited two distinct flowfields. Periodic streamwise flow features dominated the first, the number of which exactly matched the number of gaps across the span. Further investigation using stippled oil droplet flow visualization showed that this variety of streamwise streak is likely the result of a pair of counter-rotating vortices that form in the wake of each solid feature in the discontinuous step. The second is the more complex and irregular of the two, appearing to be a superposition of a leading-edge separation and large streamwise flow features. In this case, the streamwise streaks do not correspond to a particular geometric feature. This is hypothesized to be the result of a instability in the separated shear layer that may form behind the backward-facing step. Additionally, certain configurations possessed a mixture of qualities from both flowfield types. The spanwise variations in local flow angularity are attributed as the cause for these combinations. High-fidelity artificial ice shapes are known to produce Type II flowfields that cannot be attributed to a particular geometry feature. Using this fact, the second type of flowfield should be deemed most relevant to iced-wing aerodynamics. Unfortunately, the supposed shear layer instability was unable to be confirmed in the present study, and further work is required.

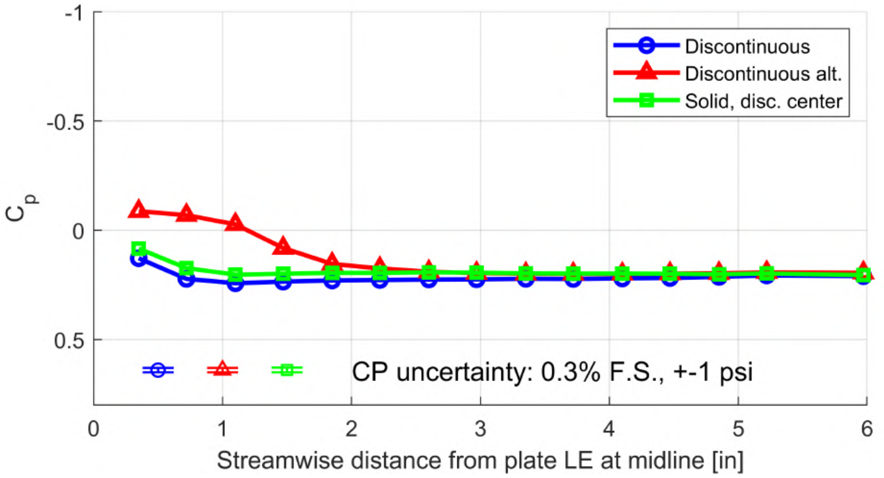

Figure 4.30: Comparison of the streamwise pressure distributions for each of the variations on the discontinuous step at a flap angle of $-10°$ and 60 m/s

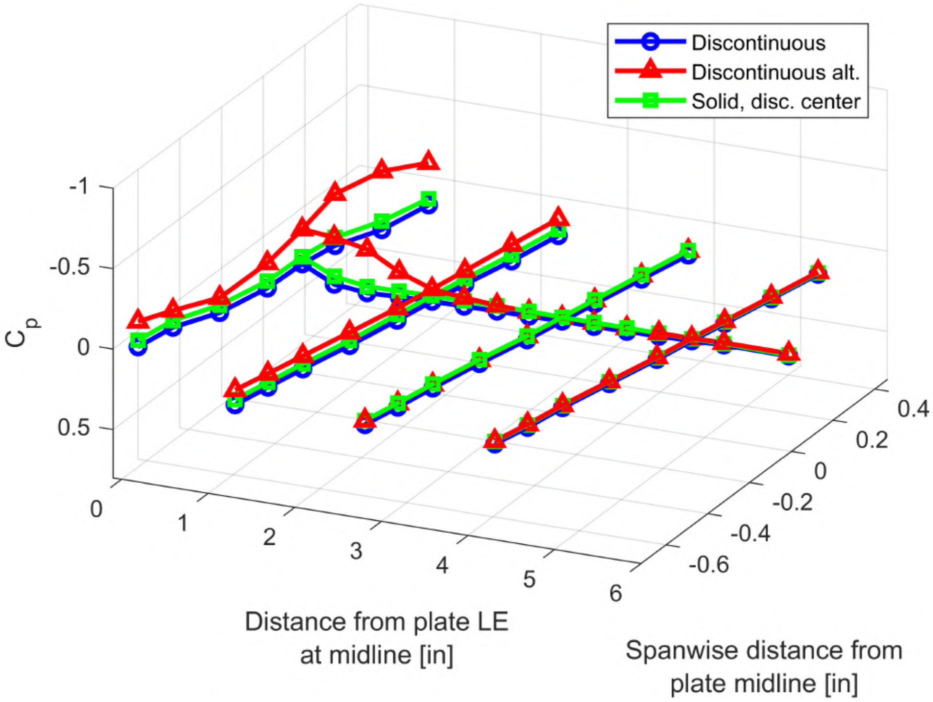

Figure 4.31: Comparison of the pressure distributions for each of the variations on the discontinuous step at a flap angle of $-10°$ and 60 m/s

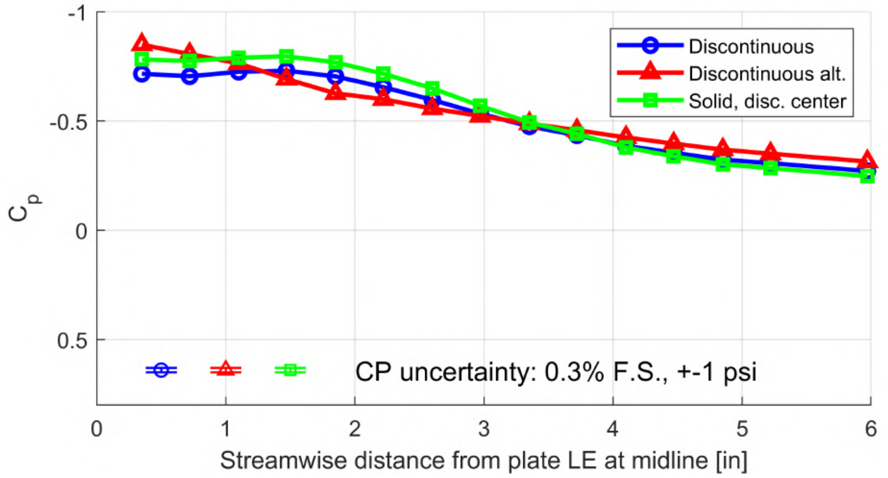

Figure 4.32: Comparison of the pressure distributions for each of the variations on the discontinuous step at a flap angle of $+4^\circ$

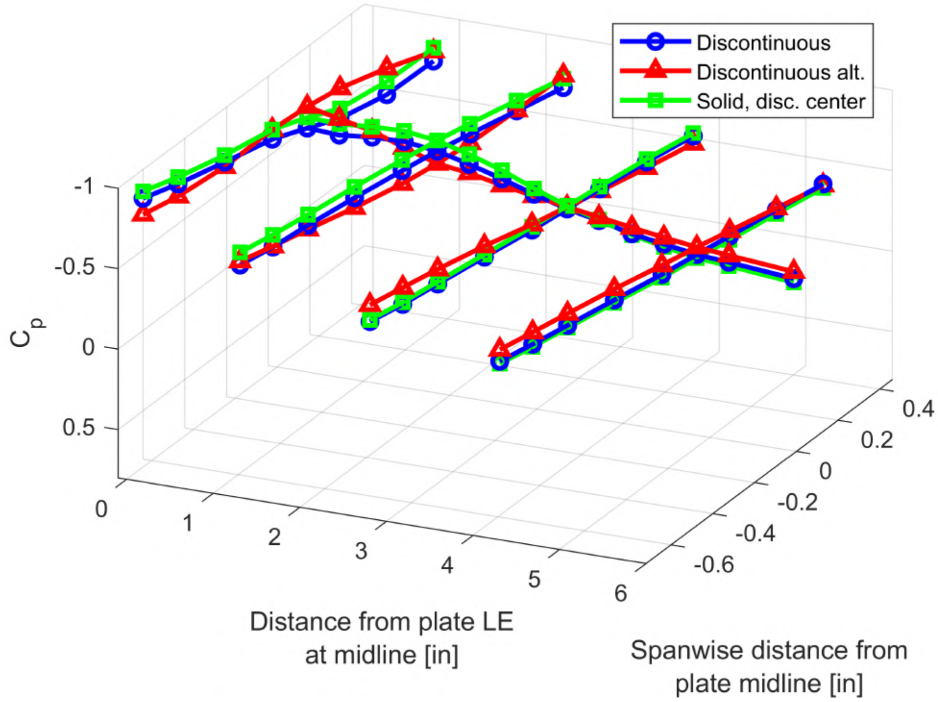

Figure 4.33: Comparison of the streamwise pressure distributions for each of the variations on the discontinuous step at a flap angle of $+4^\circ$ and 60 m/s

4.3 Effect of 24 Grit on Solid Step

During wind tunnel testing of a high-fidelity simulated horn ice shape on a NACA 0012 airfoil, Gurbacki [2] observed a periodic lengthening and shortening of the reattachment length with an ovular curvature to the oil-flow lines. This phenomenon, referred to as cell-structures, was described previously in Section 2.1.2. After a close examination of the ice shape, the cell structure pattern could not be attributed to any single repetitive large feature or protrusion in the ice shape. Additionally, a two-dimensional, smooth horn ice simulation with grit applied also resulted in cell structures, though not always with the clarity as from the high-fidelity ice shape.

Jacobs [4] tested the same NACA 0012 airfoil and horn ice geometries, and observed spanwise-periodic cell structures using surface oil flow visualization on only the high-fidelity shape. Interestingly, PIV measurements showed multiple clockwise and counter-clockwise streamwise vortices within the separation bubbles of both the two- and three-dimensional horn ice shapes. Upon examination of the distribution of these streamwise vortices, it was found that the two-dimensional ice shape resulted in a uniform distribution, while the three-dimensional resulted in concentrations. This suggested that the appearance of cell structures in the flow visualization was a product of not just streamwise vortices, but a particular distribution of them. That is, random distributions of streamwise vortices would leave no trace in the time-averaged surface oil flow visualization. Making connections to studies of the plane mixing layer and blunt flat plate separation bubble, Jacobs [4] hypothesized that a streamwise vortex instability might be a contributor to the cell structures. The rough and irregular features of the three-dimensional ice shape provided upstream perturbations, which induced Λ-shaped deformation of the spanwise vortices that are characteristic of a separated shear layer. The deformations then evolve into hairpin vortices, and thus the cell structures observed. This explanation of a shear layer instability devolving into streamwise-running vortices proves to be an attractive theory, as the following discussions show.

The fidelity study of the Maximum Scallop ice shape during the SWIP testing campaigns further showed the possible effects of grit on the flow around an artificial ice shape. Namely, these effects were illustrated using the Maximum Scallop 3-D Smooth, with and without an application of grit across the surface of the leading edge. The grit was intended to simulate some of the naturally occurring ice roughness. In the case of the 8.9% scale CRM65 model, the grit was chosen according to FAA Advisory Circular 25-25A [69], which calls for a roughness height of 3 mm for ice roughness simulations. Scaled to the 8.9% scale wing, this corresponded to 60 grit roughness, which has a mean size of 0.010”, or 254 microns. The performance effects are described in depth by Camello [59], Sandhu [60], and Woodard et al. [18]. In summary, both fidelities of the Maximum Scallop 3-D Smooth shape are non-conservative when compared to the High Fidelity Maximum Scallop, resulting in wholly different flowfields and undershooting the high fidelity performance penalties. The addition of grit degrades the aerodynamic performance slightly closer to the levels of the High Fidelity.

While the coating of 60 grit may not have had sufficient impact to recreate the aerodynamic penalities of the High Fidelity accurately, it did, however, have interesting effects upon the flowfield of the configuration. Fig. 4.34 compares fluorescent-oil surface flow visualization images for the Maximum Scallop 3-D Smooth ice shape with and without 60 grit at an angle of attack of 4°. Both shapes show signs of a spanwise-running leading-edge vortex, which is characteristic of Type II flowfields. However, the oil flow visualization for the ice shape with grit shows additional streamwise-running features that are very much reminiscent of a Type II flowfield, which for reference are discussed in Section 2.3.2 and shown in Figs. 2.30 and 2.33. It may be possible that, in this configuration, the grit is sufficient to excite the shear layer instability suggested by Jacobs [4], which would result in streamwise vorticity. It should also be noted that at high angles of attack as the separation regions grow further downstream, the visibility of streamwise features is greatly reduced across the span of the Maximum Scallop 3-D Smooth with grit. Whether this is a result of disruption of the flow features as the wing approaches stall, or whether the streamwise-running flow no longer imprints upon the oil flow is not known.

The present work sought to recreate cell structures or other streamwise features on the swept flat plate using 24 grit applied to the solid leading-edge step surface. The mean size of 24

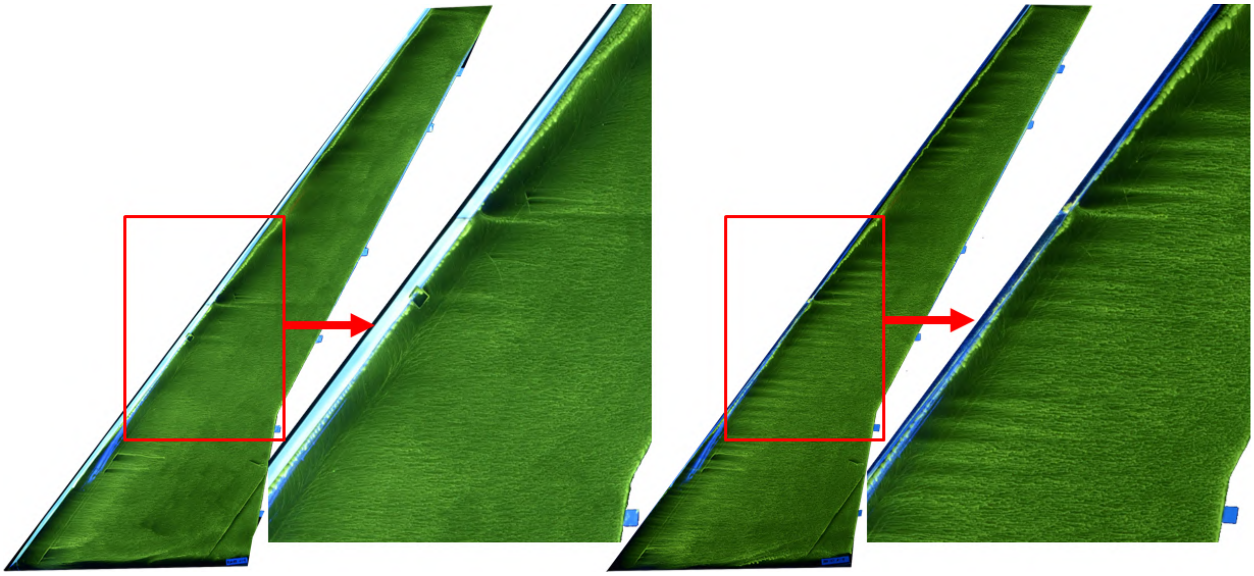

Figure 4.34: Fluorescent-oil surface flow visualization on the 8.9% scale CRM65 model with Maximum Scallop 3-D Smooth ice shape, $\alpha = 4^\circ$, $Re = 1.6 \times 10^6$; (left) no grit applied, (right) 60 grit applied

grit, 0.0270”, resulted in a roughness height to step height ratio of $k/h = 5.4\%$. Figs. 4.35 and 4.36 show surface oil flow visualization images for the overall configuration flowfields, as well as a detailed inset near the centerline. Each configuration was run at the baseline condition of -10° flap deflection and a wind speed of 60 m/s. Contrary to the expected result, the oil flow images suggest the 24 grit did not induce streamwise features, nor the cell structures described by Gurbacki [2]. The appearance of the Type II-like flow features in the case of the Maximum Scallop 3-D Smooth may have been influenced by the spanwise variation of the ice shape cross-section. In contrast, the solid leading-edge step had a constant cross-section across the entire span. Additionally, the reattachment and secondary separation lengths for both configurations are nearly identical and roughly constant across the center of the plate.

Though the flow visualization at the baseline conditions was not indicative of significant differences in the flowfields behind each step configuration, the pressure distributions do show differences. Figs. 4.37 to 4.40 compare the streamwise pressure distributions along the plate centerline for the solid step with and without grit at each flap setting and at 60 m/s. At the baseline condition of -10° flap deflection, only a slight difference in the pressure recovery is seen, with the addition of grit slowing this process, Fig. 4.37. At high flap angles, the differences between the two step configurations grow more significant. Without grit, the low-pressure region below the primary leading-edge vortex reaches a greater magnitude. With grit, the Type I pressure plateau is flatter and takes longer to recover, indicating longer reattachment lengths and enhanced energy extraction from the flow. This evolution is confirmed by the plot comparing the mean streamwise reattachment lengths for both solid steps, Fig. 4.5. The plot of reattachment lengths confirms that at higher flap angles, configurations with 24 grit applied show longer reattachment lengths than configurations without.

In review, the addition of grit to the backward-facing step geometry does not elicit the streamwise vortical features that were observed by Gurbacki [2] or during the testing of the Maximum Scallop 3-D Smooth artificial ice shape. The grit does, however, have a significant effect upon the growth of the separation region emanating from the leading-edge step. In future fidelity studies, which should aim to capture both the proper aerodynamic effect and flowfield features, the addition of grit roughness may remain an important component. In other words, the present results should show that grit has significant effects upon the flowfield that should not be discounted due to the fact that clear streamwise-running features were not produced in this case.

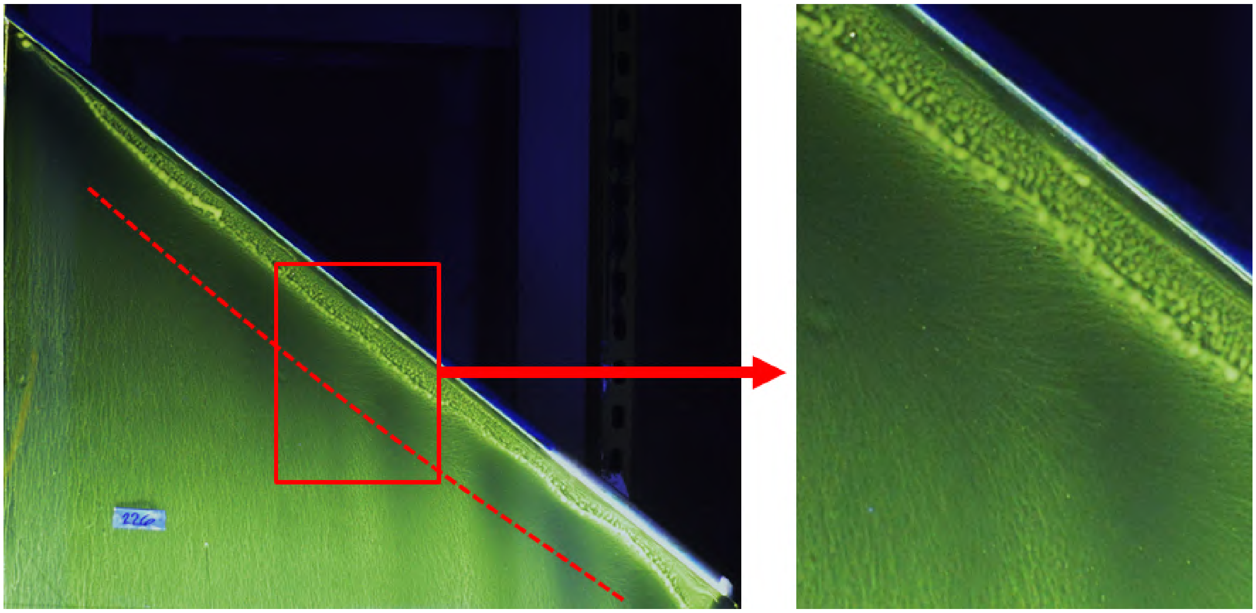

Figure 4.35: Close-up view of the fluorescent-oil surface flow visualization for the solid step without grit at a flap angle of $-10°$ and 60 m/s

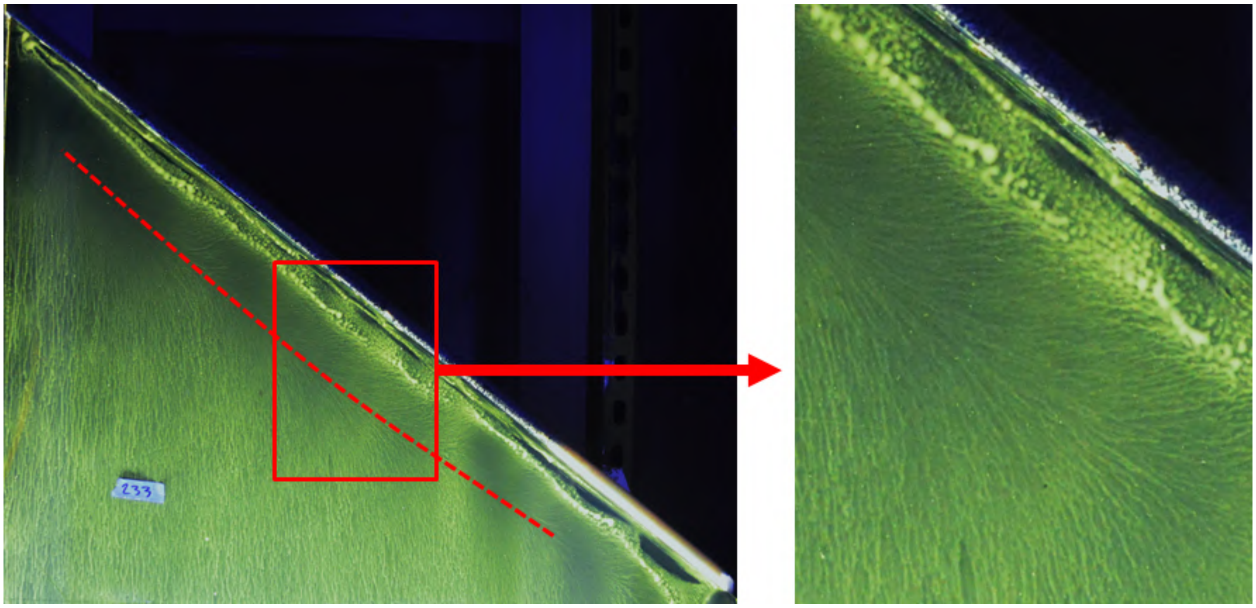

Figure 4.36: Close-up view of the fluorescent-oil surface flow visualization for the solid step with 24 grit at a flap angle of $-10°$ and 60 m/s

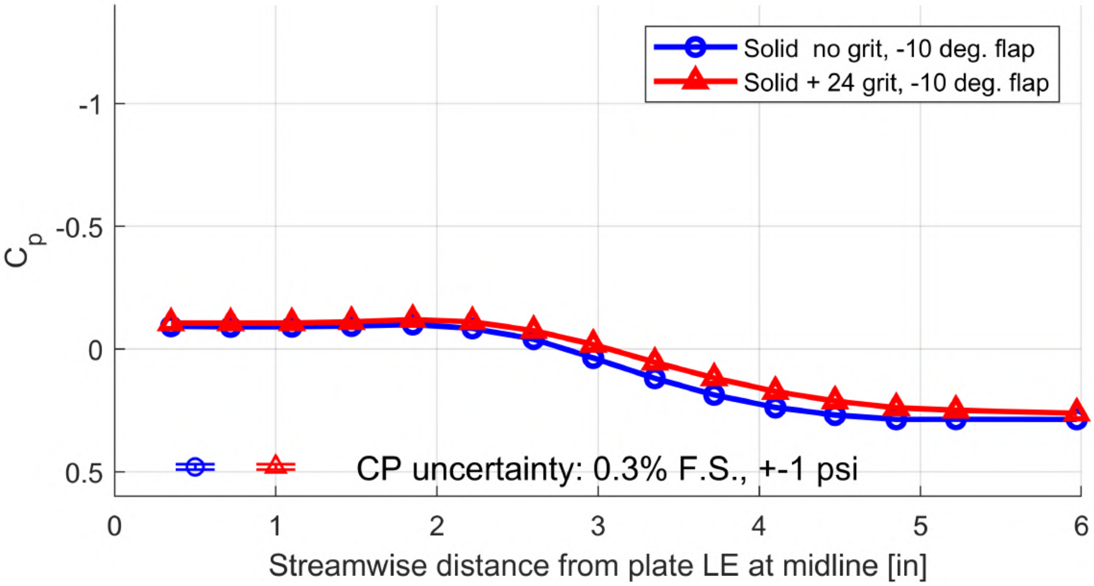

Figure 4.37: Pressure distribution along the streamwise tap row for the solid step with and without 24 grit; flap angle of $-10°$, 60 m/s

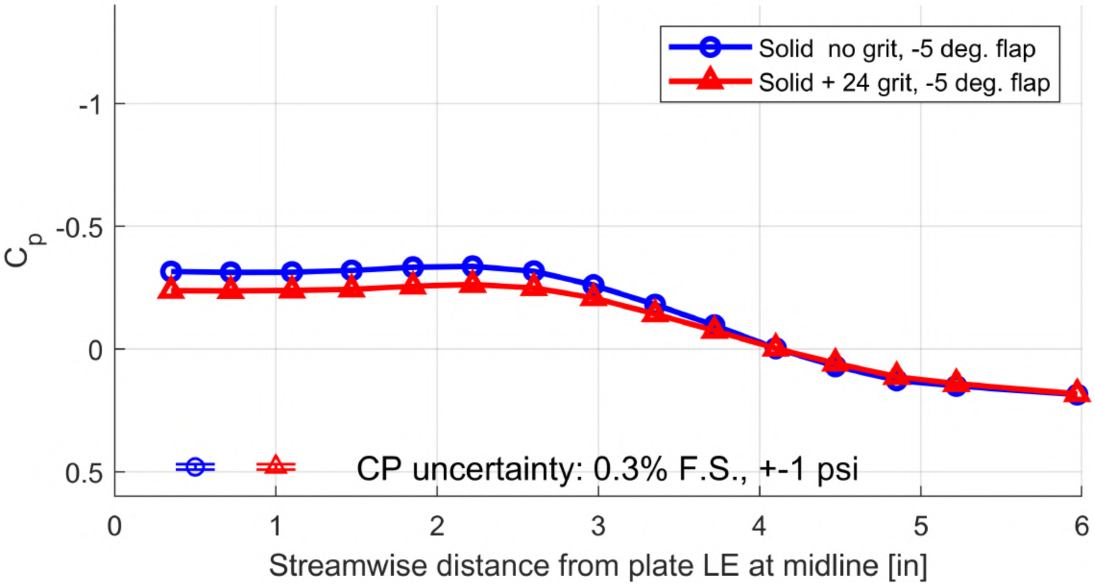

Figure 4.38: Pressure distribution along the streamwise tap row for the solid step with and without 24 grit; flap angle of $-5°$, 60 m/s

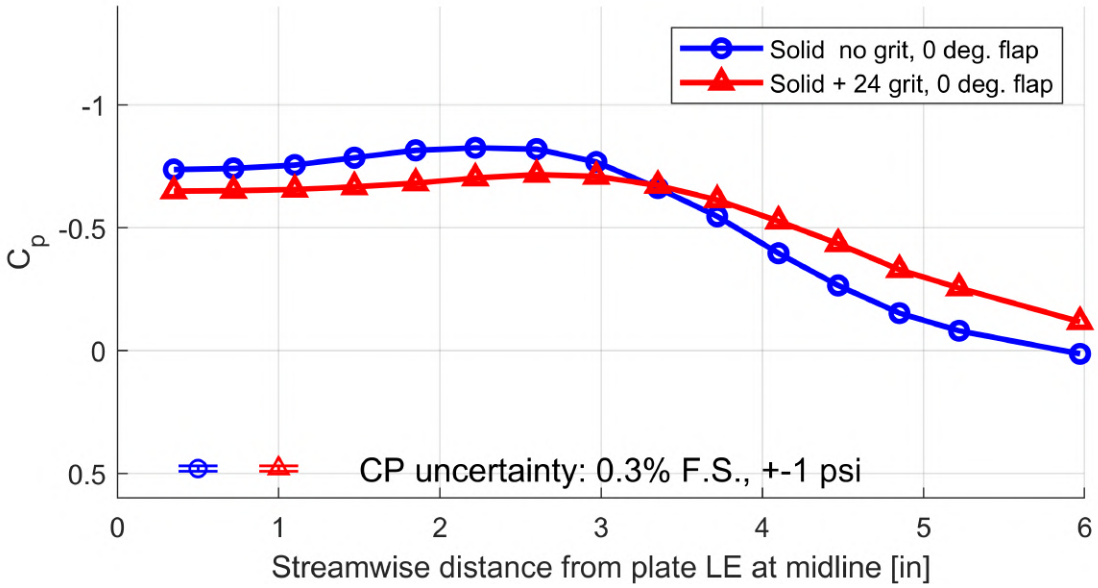

Figure 4.39: Pressure distribution along the streamwise tap row for the solid step with and without 24 grit; flap angle of 0°, 60 m/s

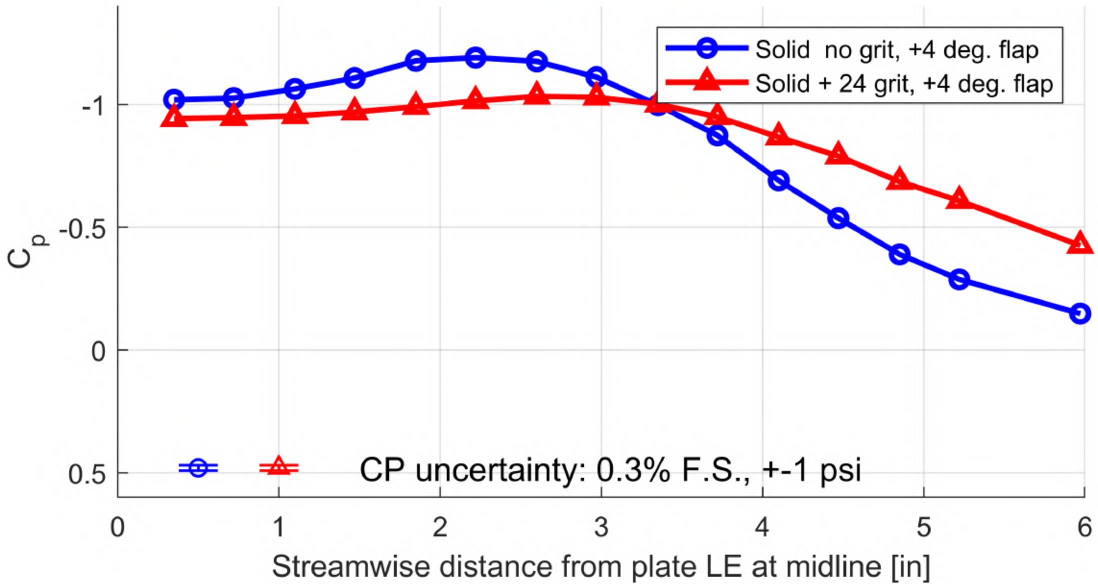

Figure 4.40: Pressure distribution along the streamwise tap row for the solid step with and without 24 grit; flap angle of +4°, 60 m/s

4.4 Reynolds Number and Mach Effects

The review in Chapter 2 mentions that the aerodynamics of iced wings typically have small or no Reynolds and Mach number dependence. The observed lack of Reynolds and Mach number dependence in swept, iced-wing flowfields allowed for the extrapolation of low-Reynolds number aerodynamic testing results to in-flight conditions during the SWIP program [41]. In the present study, the Reynolds and Mach numbers were varied as a part of the experimentation on the backward-facing steps. An atmospheric wind tunnel was used, and as a result, the Reynolds and Mach number could not be controlled independently. Three wind speeds were used, which are tabulated with corresponding Reynolds numbers based on step height and Mach numbers in Table 4.1. The Reynolds number is calculated using Eqn. 4.1, which uses the step height as the characteristic length scale. This choice of length scale is commonly made in studies of backward-facing steps, as flat plate experiments typically do not have a chord that may be used. Oil flow visualization was completed at each speed at the baseline flap setting of $-10°$ for the two primary step configurations: the discontinuous step, and the solid step without grit. Surface pressure distributions were also taken at each speed at the baseline flap setting for each of the five total step geometries.

$$Re_h = \frac{\rho U_\infty h}{\mu} \tag{4.1}$$

Table 4.1: Number of nodes for different mesh resolutions

Airspeed [m/s]	**M**	$\mathbf{Re_h}$
30	0.088	2.50×10^4
45	0.132	3.78×10^4
60	0.176	5.03×10^4

One of the first indications of the effect of varied Reynolds and Mach number is the mean streamwise reattachment length across the span of the solid step at each Reynolds num-

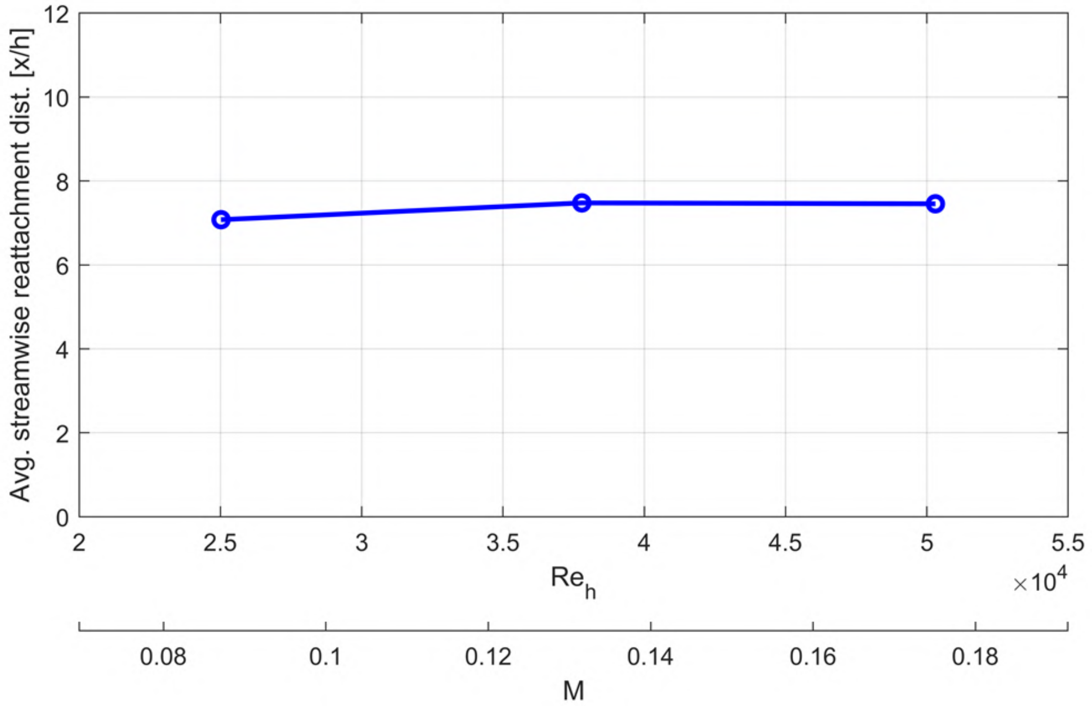

Figure 4.41: Variation in mean streamwise reattachment length with Reynolds number, as measured from oil flow visualization images

ber, Fig. 4.41. Again, the reattachment length is measured using the digital processing method in Matlab described in Section 4.1.2. The plot of reattachment length for the solid step suggests that, at least in terms of the general structure of the separation bubble, the flowfields of the configurations are largely unchanged across the Reynolds and Mach number range. The discontinuous step, which was dominated by Type II streamwise streaks across the entire span at the baseline flap setting, had no measurable reattachment length to compare. However, Fig. 4.42 compares the fluorescent-oil surface flow visualization images taken at each Reynolds and Mach number, with a close-up view to better analyze the general flow structure. It must be noted that oil flow at each airspeed was completed using varied run times. Due to the viscosity of the oil-dye mixture used, low speeds required longer times in order for the flow features to become visible on the plate surface. An inspection of the three sets of images shown in Fig. 4.42 suggests that the flow structures behind the discontinuous step remain mostly unchanged throughout the range. Aside from slight differences in the streak length owing to the differences in shear and run time, the orientation and width of the streamwise streaks to not appear to from speed to speed. Additionally, the ratio of gap to streak remains one-to-one.

As the second point of comparison, Figs. 4.43 and 4.44 show the streamwise pressure distributions for the two primary steps. The primary difference between the data for each velocity at the baseline flap setting is a slight negative trend with increasing velocity. This negative shift occurs uniformly across the distribution, and decreases in magnitude at higher airspeeds. The trend of slightly lower pressures across the Reynolds and Mach number range held true for each of the five configurations tested. Overall, the results presented in this section indicate that Reynolds and Mach number variation are not a strong influence over the flowfield structure or pressure distribution. This is in agreement with previous studies which concluded that the iced-wing flowfield, along with associated aerodynamic effects, are largely independent of Reynolds and Mach number. It should be noted that the Reynolds and Mach number effects were not investigated in conjunction with flap angle variation. Instead, this investigation of Reynolds number effects was limited to the baseline flap setting of -10°. It may be possible that Reynolds or Mach number may have an impact at higher flap angles. Ultimately, the trend is that ice shapes, which are overwhelming perturbations much like the backward-facing steps, are largely independent of Reynolds number regardless of angle of attack. While these data were collected at a single flap setting, it may be safely assumed that higher flap angles would likely not have had increased Reynolds or Mach number effects relative to the baseline angle tested.

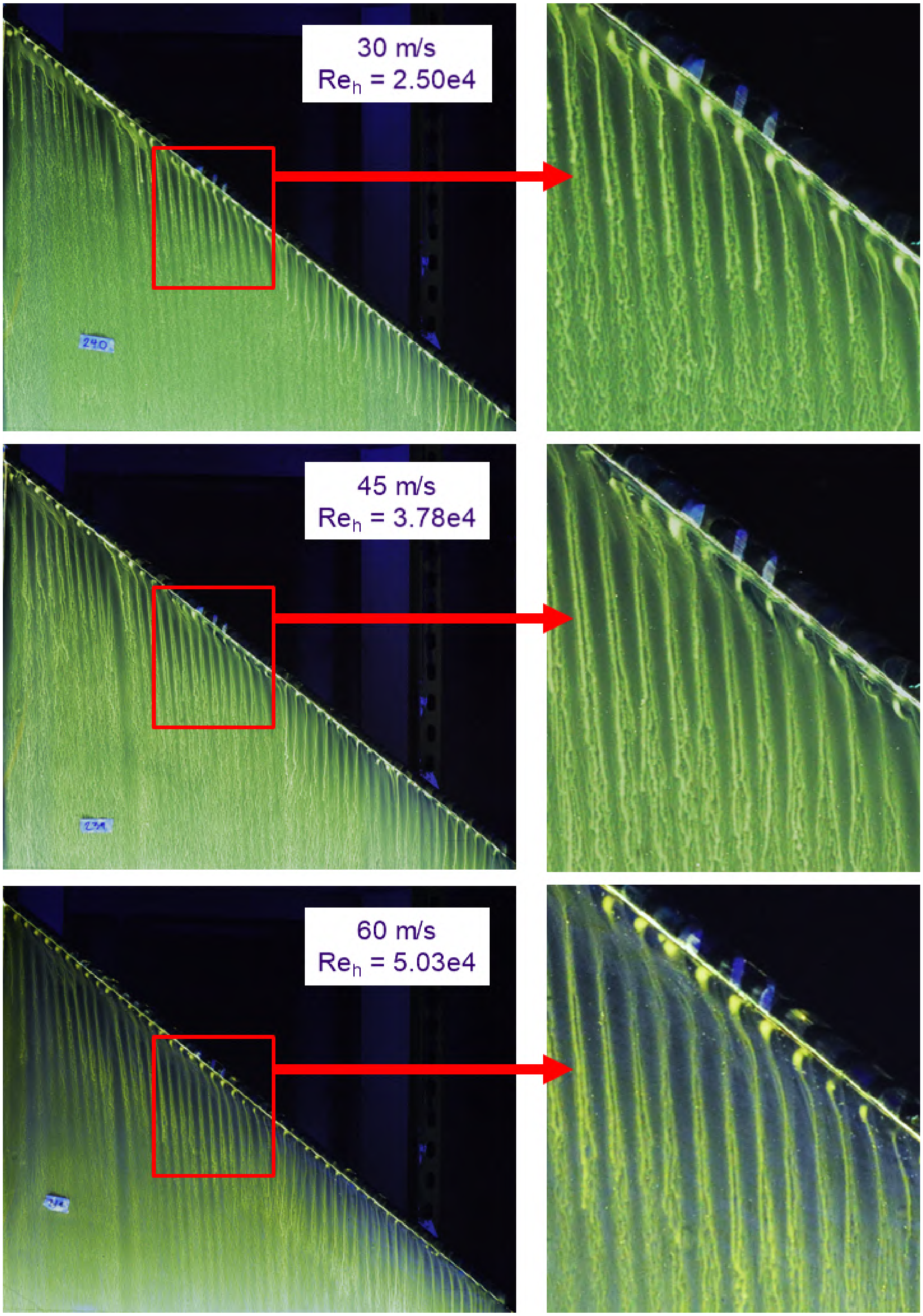

Figure 4.42: Oil flow visualization images of discontinuous step with -10° flap deflection at each airspeed tested; (top) 30 m/s, 3 minute run time (center) 45 m/s, 4 minute run time (bottom) 60 m/s, 5 minute run time

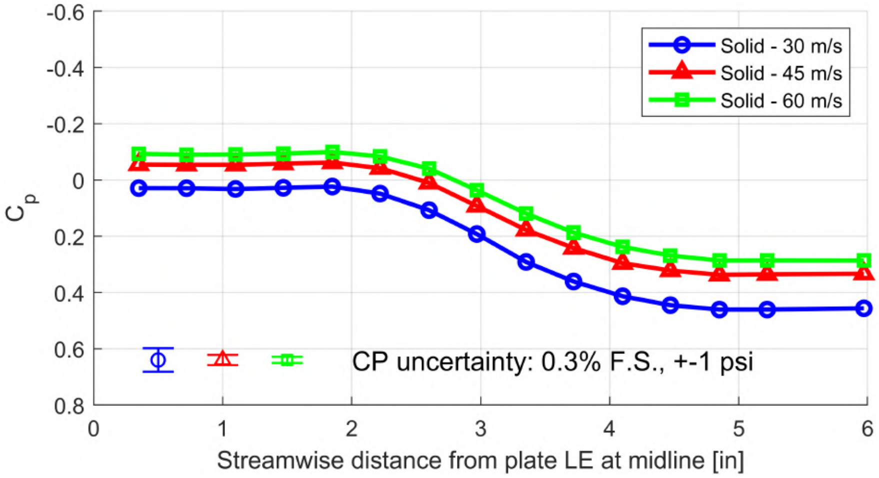

Figure 4.43: Variation in the pressure distribution along the streamwise tap row; solid step with flap angle of -10°

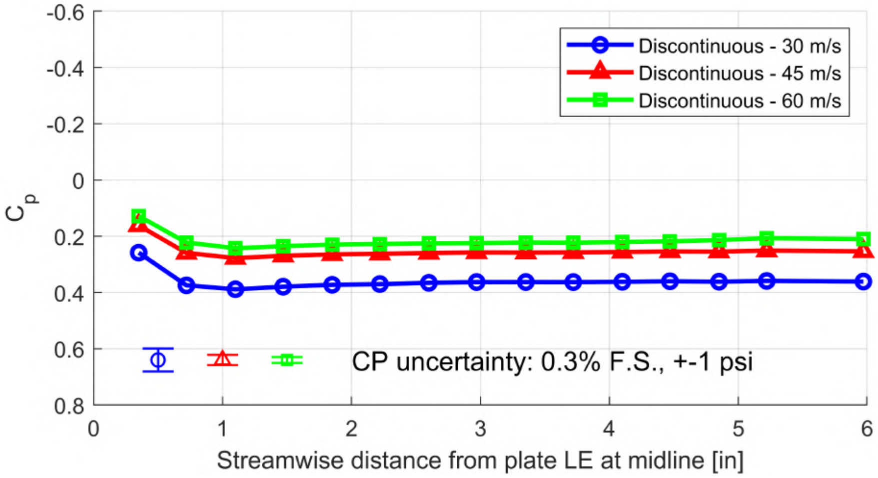

Figure 4.44: Variation in the pressure distribution along the streamwise tap row; discontinuous step with flap angle of -10°

Chapter 5

Summary, Conclusions, and Recommendations

5.1 Summary

This thesis describes the design and wind tunnel testing of a swept flat plate with removable leading-edge backward-facing steps to investigate the flowfields associated with swept-wing artificial ice shapes. The backward-facing step geometries were designed to reproduce two types of flowfield observed during aerodynamic testing of the CRM65 semispan wing model. First, the Type I flowfield was dominated by a spanwise-running leading-edge separation vortex. This type of flowfield was recreated with a continuously solid leading-edge backward-facing step with step height 0.5”. Second, the Type II flowfield lacked a leading-edge vortex, and streamwise-running streaks of oil dominated oil flow visualization of this flowfield. The Type II flowfield was produced in this study using a modification of the solid backward-facing step geometry, which removed material in a manner similar to the Medium Gap 3-D Discontinuous artificial ice shape developed by Woodard et al. [22].

The steps were constructed in five sections using the 3-D printing method of fused-deposition modeling, and were composed of ABS filament. Superficial modifications were also made to the two backward-facing steps to test additional configurations. A coating of 24 grit was added to the solid step, and the gap periodicity of the spanwise discontinuous step was changed by taping over every second gap. The last step geometry was simply the discontinuous step center section installed in place of the solid step center section.

Testing was conducted at the University of Washington 3'x3' subsonic wind tunnel. Fluorescent-oil surface flow visualization techniques were applied for a qualitative image of the flowfield over the flat plate. Surface pressures were measured behind the step with an array of 48 taps. Local flow angularity ahead of the leading edge of the swept flat plate was also computed using measurements from a five-hole pressure probe.

5.2 Conclusions

The objective of this work was to investigate the flow physics of the streamwise streak-dominated Type II flowfield and the effect of spanwise discontinuities in a swept, backward-facing step. The following is a list of the key conclusions and observations made from this research:

1. Varying the trailing-edge flap deflection had strong, spanwise-dependent effects on the flat plate flowfields.
    a. The local flow angularity varied widely with the flap setting, as well as across the span of the flat plate, as computed from five-hole pressure probe measurements.
    b. For the solid step, increased flap angle led to growth of the separation region behind the step, shown by oil flow visualization and reattachment lengths.
    c. For the discontinuous step, increasing flap angle caused the flowfield to shift from a vortex generator-type streamwise streak-dominated flowfield to one with separated flow and intermittent shear layer instability-type streaks
2. Two distinct streamwise flow features were observed to be responsible for the Type II streamwise streaks behind the configurations of the discontinuous step geometries.
    a. Vortex generator-type flows left traces in the oil flow visualization that suggested they were composed of pairs of counter-rotating vortices that formed in the wake of each solid feature in the step.

   b. Shear layer instability-type flows did not originate from any single geometric feature and were hypothesized to be a result of streamwise vortices from a shear layer instability. This instability may be excited by the discontinuous backward-facing step in some configurations.

   c. Of the two streamwise flow features identified in the flowfields associated with spanwise discontinuous steps, the shear layer instability-type is most similar to the observed flowfields of the 3-D Discontinuous artificial ice shapes for scallop ice.

3. The addition of 24 grit on the solid backward-facing step geometry had only small effects on the flowfield of each configuration.

   a. Cell structures, as defined by periodic variations in the reattachment length and ovular curvature in the surface oil flow, were not identified in the present work.

   b. The pressure distribution behind configurations of the solid step with 24 grit applied showed slower pressure recovery and flow reattachment when compared to configurations of the solid step without grit.

   c. The addition of 24 grit was seen to increase the reattachment length of the separation behind configurations of the solid step at higher flap deflections.

4. Reynolds and Mach number did not have significant effect on the flow behind the backward-facing step geometries at the configurations tested.

   a. Reattachment length behind configurations of the solid backward-facing step geometry did not vary with Reynolds and Mach number, as measured using oil flow visualization.

   b. Only small differences were observed in the pressure distributions of the configurations of each step geometry tested.

   c. The trend of small Reynolds and Mach number effects agrees with past iced-wing aerodynamics research, as well as research on swept backward-facing steps.

5.3 Recommendations

The experimental results presented in this thesis have provided new insight into artificial iced-wing flow physics. This includes the identification of previously undetermined flowfield structures, such as the composition of vortex generator-type streamwise streaks. However, these data have also served to identify areas in which the flowfield is still largely undetermined. For instance, the transition from one type of streamwise streak to another. Flow visualization images and surface pressures have given hints, though much work remains for the future. What follows is a list of recommendations for the next steps that would deepen the understanding of swept-wing icing flow physics.

1. The flow physics of swept flat plates should be studied more to better control conditions and accurately interpret results.
    a. Significant variations in the local flow angularity were measured across the span of the flat plate using the five-hole probe.
    b. The causes of the spanwise dependency were not determined, but had an influence on the flowfield behind the leading-edge step, as observed in the oil flow visualization.
    c. No data were collected to quantify the effect of flap deflection on the stagnation point location. Further testing should include pressure taps along the surface of the leading edge.
    d. Only one plate height was used. Additional plate heights could be studied to determine if the test section confinement affects the resulting flowfield.
    e. More work should be done to investigate the flowfield around a swept flat plate, perhaps with a rounded leading edge, rather than a backward-facing step.
2. The understanding of the flow about all backward-facing step geometries tested in this thesis would benefit from off-body measurements or flow visualization, as well as unsteady measurements.

    a. Particle image velocimetry (PIV) could provide instantaneous and mean flow across multiple planes above and along the plate.
    b. Unsteady surface pressure measurements could help identify the behavior of certain flowfields, such as separated and reattaching flow. Additional care should also be taken to capture the entire length of the pressure recovery.
    c. PIV, hot wire anemometry, or laser-doppler velocimetry could provide turbulence statistics. This type of detailed data is not commonly collected for iced-wing flowfields.
    d. Smoke flow could provide instantaneous qualitative images of the off-body flowfield that were not captured by surface oil flow.

3. The shear layer instability-type streamwise features should be studied specifically.
    a. As previous tests have shown, certain types of flowfield cannot be accurately characterized with surface flow visualization techniques or surface pressures.
    b. Off-body velocity measurements or direct numerical simulation would be most helpful to characterize this flow phenomenon.

4. Rather than low-fidelity step geometries, use high-fidelity leading-edge ice shapes on the flat plate.
    a. Though it would be difficult to adapt such an irregular geometry to a swept flat plate study, it would provide results that are most relevant to furthering the understanding of realistic swept wing icing.
    b. A realistic swept-wing ice shape could also shed new light on the formation of the streamwise-running features observed during CRM65 testing.
    c. Data from a high-fidelity shape could be compared to the different types of flowfield that are observed behind a geometry similar to the Maximum Scallop 3-D Discontinuous.

5. Study more artificial scallop-type step geometries, similar to the variations on the Maximum Scallop ice shapes designed by Woodard et al. [22].
    a. Additional study of these geometries could help interpret the aerodynamic testing results in the context of the fundamental flow physics.
    b. Having more discontinuous step geometries may lead to an improved picture of the most important factors that influence each the flowfields of each configuration.

Chapter 6

References

[1] Bragg, M. B., Broeren, A. P., and Blumenthal, L. A., "Iced-Airfoil Aerodynamics," *Progress in Aerospace Sciences*, Vol. 41, No. 5, 2005, pp. 323–362.

[2] Gurbacki, H., *Ice-induced unsteady flowfield effects on airfoil performance*, Master's thesis, University of Illinois at Urbana-Champaign, 2003.

[3] Busch, G., Broeren, A., and Bragg, M., "Aerodynamic simulation of a horn-ice accretion on a subscale model," *Journal Of Aircraft*, Vol. 45, No. 2, 2008, pp. 604–613.

[4] Jacobs, J., *Iced airfoil separation bubble measurements by particle image velocimetry*, Ph.D. thesis, University of Illinois at Urbana-Champaign, 2007.

[5] Ansell, P. J. and Bragg, M. B., "Unsteady Modes in Flowfield About Airfoil with Horn-Ice Shape," *Journal of Aircraft*, Vol. 53, No. 2, 2016, pp. 475–486.

[6] Vargas, M. and Reshotko, E., "LWC and Temperature Effects on Ice Accretion Formation on Swept Wings at Glaze Ice Conditions," Tech. Rep. NASA/TM—2000-209777, 2000.

[7] Khodadoust, A. and Bragg, M. B., "Aerodynamics of a Finite Wing with Simulated Ice," *Journal Of Aircraft*, Vol. 32, No. 1, 1995, pp. 137–144.

[8] Kwon, O. J. and Sankar, L. N., "Numerical simulation of the flow about a swept wing with leading-edge ice accretions," *Computers and Fluids*, Vol. 26, No. 2, 1997, pp. 183–192.

[9] Reehorst, A., Potapczuk, M., Ratvasky, T., and Gile Laflin, B., "Wind Tunnel Measured Effects on a Twin-Engine Short-Haul Transport Caused by Simulated Ice Accretions," Tech. Rep. NASA/TM—1997-107419, 1997.

[10] Broeren, A. P., Lee, S., Shah, G. H., and Murphy, P. C., "Aerodynamic Effects of Simulated Ice Accretion on a Generic Transport Model," Tech. Rep. NASA/TM—2012-217246, 2012.

[11] Papadakis, M., Yeong, H.-W., Wong, S.-C., Vargas, M., and Potapczuk, M., "Experimental investigation of ice accretion effects on a swept wing," Tech. Rep. DOT/FAA/AR-05/39, 2005.

[12] Kim, H. and Bragg, M., "Effects of leading-edge ice accretion geometry on airfoil performance," *17th Applied Aerodynamics Conference*, 1999, p. 3150.

[13] Manshadi, M. and Esfeh, M., "Experimental investigation of flowfield over an iced aerofoil," *The Aeronautical Journal*, Vol. 120, No. 1227, 2016, pp. 735–756.

[14] Papadakis, M., Alansatan, S., and Seltmannt, M., "Experimental study of simulated ice shapes on a NACA 0011 airfoil," *37th Aerospace Sciences Meeting and Exhibit*, American Institute of Aeronautics and Astronautics Inc, AIAA, 1999.

[15] Broeren, A. P., Bragg, M. B., Addy, Harold E., J., Guffond, D., Lee, S., and Moens, F., "Effect of High-Fidelity Ice Accretion Simulations on the Performance of a Full-Scale Airfoil Model - NASA/TM-2010-216344," *46th AIAA Aerospace Sciences Meeting and Exhibit*, 2008.

[16] Calay, R. K., Holdo, A. E., and Mayman, P., "Experimental simulation of runback ice," *Journal of Aircraft*, Vol. 34, No. 2, 1997, pp. 206.

[17] Lee, S. and Bragg, M. B., "Experimental investigation of simulated large-droplet ice shapes on airfoil aerodynamics," *Journal of Aircraft*, Vol. 36, No. 5, 1999, pp. 844.

[18] Woodard, B. S., Broeren, A. P., Lee, S., Lum, C. W., and Bragg, M. B., "Summary of Ice Shape Geometric Fidelity Studies on an Iced Swept Wing," *Proceedings of the 2018 Atmospheric and Space Environments Conference*, Atlanta, GA, June 2018.

[19] Woodard, B. S. and Bragg, M. B., "Effect of Spanwise Discontinuities on the Aerodynamics of a Swept Wing with Scalloped Ice Accretion," *Proceedings of the 12th Atmospheric and Space Environments Conference*, Reno, NV, June 2020.

[20] Selby, G., *Phenomenological Study of Subsonic Turbulent Flow Over a Swept Rearward-Facing Step*, Ph.D. thesis, University of Delaware, 1982.

[21] Selby, G., "Passive control of three-dimensional separated vortical flow associated with swept rearward-facing steps," *Journal of Fluids Engineering, Transactions of the ASME*, Vol. 111, No. 1, 1989, pp. 99–101.

[22] Woodard, B., Broeren, A., Potapczuk, M., Lee, S., Lum, C., Bragg, M., and Smith, T., "Experimental Aerodynamic Simulation of a Scallop Ice Accretion on a Swept Wing," Tech. Rep. SAE Technical Paper 2019-01-1984, 2019.

[23] Tanner, M., "The Pressure at the Reattachment Point in Subsonic Two-Dimensional Steady Base Flow," *Aeronautical Quarterly*, Vol. 27, No. 1, 1976, pp. 55–65.

[24] "Ice Accretion Simulation," Tech. Rep. AGARD-AR-344, 1997.

[25] Lynch, F. T. and Khodadoust, A., "Effects of Ice Accretion on Aircraft Aerodynamics," *Progress in Aerospace Sciences*, Vol. 37, No. 8, 2001, pp. 669–767.

[26] Furlong, G. C. and McHugh, J. C., "A Summary and Analysis of the Low-Speed Longitudinal Characteristics of Swept Wings at High Reynolds Number," Tech. Rep. NACA-TR-1339, 1957.

[27] Poll, D., "Spiral Vortex Flow Over a Swept-Back Wing," *Aeronautical Journal*, Vol. 90, No. 895, 1986, pp. 185–199.

[28] Khodadoust, A. and Bragg, M. B., "Aerodynamics of a Finite Wing with Simulated Ice," *Journal of Aircraft*, Vol. 32, No. 1, 1995, pp. 137–144.

[29] Vargas, M., Papadakis, M., Potapczuk, M., Addy, H., Sheldon, D., and Giriunas, J., "Ice Accretions on a Swept GLC-305 Airfoil," Tech. Rep. NASA/TM—2002-211557, 2002.

[30] Broeren, A., Potapczuk, M., Riley, J., Villiedieu, P., Moens, F., and Bragg, M., “Swept-Wing Ice Accretion Characterization and Aerodynamics,” Tech. Rep. NASA/TM—2013-216555, 2013.

[31] Vassberg, J. C., DeHaan, M. A., Rivers, S. M., and Wahls, R. A., “Development of a Common Research Model for Applied CFD Validation Studies,” *Proceedings of the 26th AIAA Applied Aerodynamics Conference*, Honolulu, HI, August 2008.

[32] Rivers, M. and Dittberner, A., “Experimental Investigation of the NASA Common Research Model,” *AIAA Paper 2010-4218*, June 2010.

[33] Broeren, A. P., Potapczuk, M. G., Lee, S., Malone, A. M., Paul Jr., B. P., and Woodard, B. S., “Ice-Accretion Test Results for Three Large-Scale Swept-Wing Models in the NASA Icing Research Tunnel,” *Proceedings of the 8th AIAA Atmospheric and Space Environments Conference*, June 2016.

[34] Fujiwara, G., Bragg, M., Triphahn, C., Wiberg, B., Woodard, B., Loth, E., Malone, A., Paul, B., Pitera, D., Wilcox, P., and Khodadoust, A., “Development of Experimental Icing Simulation Capability for Full-Scale Swept Wings - Hybrid Design Process, Years 1 and 2,” Tech. Rep. NASA/CR—2017-219573, 2017.

[35] Lee, S., Broeren, A. P., Addy Jr., H. E., Sills, R., and Pifer, E., “Development of 3-D Ice Accretion Measurement Method,” Tech. Rep. NASA/TM—2012-217702, 2012.

[36] Broeren, A., Addy Jr., H., Lee, S., and Monastero, M., “Validation of 3-D Ice Accretion Measurement Methodology for Experimental Aerodynamic Simulation,” Tech. Rep. NASA/TM—2015-218724, 2015.

[37] Camello, S. C., Lee, S., Lum, C. W., and Bragg, M. B., “Generation of Fullspan Leading-Edge 3D Ice Shapes for Swept-Wing Aerodynamic Testing,” *Proceedings of the 8th AIAA Atmospheric and Space Environments Conference*, June 2016.

[38] Broeren, A. P., Woodard, B. S., Diebold, J. M., and Moens, F., “Low-Reynolds Number Aerodynamics of an 8.9% Scale Semispan Swept Wing for Assessment of Icing Effects,” *Proceedings of the 9th AIAA Atmospheric and Space Environments Conference*, Denver, CO, June 2017.

[39] Woodard, B., Broeren, A., Diebold, J., and Bragg, M., “Preliminary Testing of Low Reynolds Number Aerodynamics for a Swept Wing With Artificial Ice Roughness,” Tech. Rep. DOT/FAA/TC-17/48, Federal Aviation Administration, 2017.

[40] Lum, C. W., Diebold, J. M., Woodard, B. S., Sandhu, N., and Bragg, M. B., “The Application of a Five-Hole Probe Wake-Survey Technique to the Study of Swept Wing Icing Aerodynamics,” *Proceedings of the 9th Atmospheric and Space Environments Conference*, Denver, CO, June 2017.

[41] Broeren, A. P., Lee, S., Woodard, B., Lum, C. W., and Smith, T. G., “Independent Effects of Reynolds and Mach Numbers on the Aerodynamics of an Iced Swept Wing,” *Proceedings of the2018 Atmospheric and Space Environments Conference*, Atlanta, GA, June 2018.

[42] Sandhu, N., Soltani, M. R., Bragg, M. B., Lum, C. W., Woodard, B., Broeren, A. P., and Lee, S., “Effect of Simulated Scalloped Ice on the Aerodynamics of a Swept-Wing at Low-Reynolds Number,” *Proceedings of the 2018 Atmospheric and Space Environments Conference*, Atlanta, GA, June 2018.

[43] Broeren, A., Potapczuk, M., Lee, S., Woodard, B., Bragg, M., and Smith, T., “Experimental Aerodynamic Simulation of Glaze Ice Accretion on a Swept Wing,” No. 2019-01-1987, SAE International, 2019.

[44] Broeren, A. P., Lee, S., Woodard, B. S., and Bragg, M. B., “Effect of Geometric Fidelity on the Aerodynamics of a Swept Wing with Glaze Ice Accretion,” *Proceedings of the 12th Atmospheric and Space Environments Conference*, Reno, NV, June 2020.

[45] Bragg, M. B., Yoshida, W. T., Broeren, A. P., Lee, S., and Woodard, B. S., “Ice Shape Classification for Swept Wings,” *Proceedings of the 12th Atmospheric and Space Environments Conference*, Reno, NV, June 2020.

[46] Olsen, W., Shaw, R., and Newton, J., “Ice Shapes and the Resulting Drag Increase for a NACA 0012 Airfoil,” Tech. Rep. NASA/TM—1984-83556, 1984.

[47] Busch, G. and Bragg, M., “Experimental Study of Full-Scale Iced-Airfoil Aerodynamic Performance using Sub-scale Simulations,” *1st AIAA Atmospheric and Space Environments Conference*, 2009.

[48] Vargas, M., “Current experimental basis for modeling ice accretions on swept wings,” *Journal of Aircraft*, Vol. 44, No. 1, 2007, pp. 274–290.

[49] Vargas, M., “Swept Wing Icing Physics Studies at NASA Glenn Research Center 1990-2006,” *SAE Aircraft and Engine Icing International Conference*, Vol. 116, 2007.

[50] Vargas, M. and Reshotko, E., “Parametric Experimental Study of the Formation of Glaze Ice Shapes on Swept Wings,” Tech. Rep. NASA/TM—1999-208900, 1999.

[51] Presteau, X., Montreuil, E., Leroy, A., Guffond, D., Henry, R., and Personne, P., “Experimental study of the scallop formation on swept cylinder,” *SAE Aircraft and Engine Icing International Conference*, 2007.

[52] Bragg, M. B., Khodadoust, A., and Kerho, M. F., “LDV Flowfield Measurements on a Straight and Swept Wing with a Simulated Ice Accretion,” *AIAA Aerospace Sciences Meeting and Exhibit*, Reno, NV, January 1993.

[53] Broeren, A. P., Addy, Harold E., J., Busch, G. T., Bragg, M. B., Guffond, D., and Montreuil, E., “Aerodynamic Simulation of Ice Accretion on Airfoils,” Tech. Rep. NASA/TP-2011-216929, 2011.

[54] Bragg, M., Khodadoust, A., and Spring, S., “Measurements in a leading-edge separation bubble due to a simulated airfoil ice accretion,” *AIAA Journal*, Vol. 30, No. 6, 1992, pp. 1462.

[55] Lee, S. and Bragg, M., "Effects of simulated-spanwise-ice shapes on Airfoils: Experimental investigation," *37th Aerospace Sciences Meeting and Exhibit*, American Institute of Aeronautics and Astronautics Inc, AIAA, 1999.

[56] Broeren, A. P., Diebold, J. M., and Bragg, M. B., "Aerodynamic Classification of Swept-Wing Ice Accretion," Tech. Rep. NASA/TM—2013-216381, 2013.

[57] Fujiwara, G. E. C., Bragg, M. B., Camello, S., and Lum, C. W., "Computational and Experimental Ice Accretions of Large Swept Wings in the Icing Research Tunnel," *Proceedings of the 8th AIAA Atmospheric and Space Environments Conference*, June 2016.

[58] Radenac, E., "Validation of a 3D Ice Accretion Tool on Swept Wings of the SUNSET2 Program," *Proceedings of the 8th AIAA Atmospheric and Space Environments Conference*, June 2016.

[59] Camello, S. C., *Effect of ice accretion simulation fidelity on low-reynolds number swept-wing aerodynamic performance*, Master's thesis, University of Washington, Seattle, WA, 2017.

[60] Sandhu, N., *Aerodynamics of a Swept Wing With Simulated Scalloped Ice at Low Reynolds Number*, Master's thesis, University of Washington, 2018.

[61] Weber, D. J., "Hot film velocity measurements downstream of a swept backward-facing step," Tech. Rep. CRDEC-TR-221, 1990.

[62] Weber, D. J. and Danberg, J. E., "Correlation of mean velocity measurements downstream of a swept backward-facing step," *AIAA Journal*, Vol. 30, No. 11, 1992, pp. 2701–2706.

[63] Hartman, R., *Computational study of incompressible turbulent flow over a swept rearward-facing step*, Ph.D. thesis, University of Delaware, 1988.

[64] Kaltenbach, H.-J. and Janke, G., "Direct numerical simulation of flow separation behind a swept, rearward-facing step at Re H =3000," *Physics of Fluids*, Vol. 12, No. 9, 2000, pp. 2320–2337.

[65] Kaltenbach, H.-J., "Turbulent flow over a swept backward-facing step," *European Journal of Mechanics B/Fluids*, Vol. 23, No. 3, 2004, pp. 501–518.

[66] Engineering Laboratory Design, Inc., *Operating and Maintenence Instructions, 36" Open-Circuit Wind Tunnel*.

[67] Williams, O., Samuell, M., Sarwas, E., Robbins, M., and Ferrante, A., "Experimental Study of a CFD Validation Test Case for Turbulent Separated Flows," *AIAA Scitech Forum*, Orlando, FL, January 2020.

[68] Diebold, J. M., *Aerodynamics of a Swept Wing with Leading-Edge Ice at Low Reynolds Number*, Master's thesis, University of Illinois at Urbana-Champaign, Urbana, Illinois, 2012.

[69] "Federal Aviation Administration, Advisory Circular AC 25-25A," Tech. rep., 2014.